11-17-2016

Frequency Tunable Antennas and Surface Microwave Imaging System Using Microfluidic Reconfiguration Techniques

Abhishek Dey
University of South Florida, abhishek@mail.usf.edu

Frequency Tunable Antennas and Surface Microwave Imaging System Using Microfluidic Reconfiguration Techniques

by

Abhishek Dey

A dissertation submitted in partial fulfilment
of the requirements for the degree of
Doctor of Philosophy
Department of Electrical Engineering
College of Engineering
University of South Florida

Major Professor: Gokhan Mumcu, Ph.D.
Tom Weller, Ph.D.
Jing Wang, Ph.D.
Rasim Guldiken, Ph.D.
Al-Aakhir Rogers, Ph.D.

Date of Approval:
October 19, 2016

Keywords: Liquid Metal, Metallized Plate, Reconfigurable Antenna, High Power, Textile Antenna

DEDICATION

To my parents, Amrapali and Ashish.

ACKNOWLEDGMENTS

I would like to thank my advisor Dr. Gokhan Mumcu, I am immensely indebted to you. I am forever grateful for your guidance, patience and never-ending support, but most importantly, for always challenging me. I cannot imagine my PhD experience without you. You are truly my mentor.

I am sincerely grateful to Dr. Thomas Weller for providing his valuable guidance during my initial years as a graduate student. I will always remember the meeting I had in your office when I expressed my desire to switch my research focus towards RF and how you went out of your way to recommend me to Dr. Mumcu.

I want to express my deepest and thankful feelings to Dr. Jing Wang for all the knowledge I gained from his courses regarding microfabrication processes. Your courses coupled theory with practical classes that helped me understand and gain hands on experience with different fabrication techniques. These skills were of immense help towards my research.

I want to thank Dr. Rasim Guldiken for his invaluable inputs on understanding and fabricating microfluidic channels. I am thankful for the initial meetings with you where you guided me to address challenges I was facing with bonding the channels as well as determining the optimum channel geometry for implementing my antennas.

I will always be grateful to Dr. Al-Aakhir Rogers for making me feel so welcomed when I joined the BioMEMS group back in 2010. As a fresh graduate student and so far away from home, it was very comforting to feel part of the group. Your PhD defense was the first one I attended and it could not have created a higher bar for what a dissertation defense should be.

I am thankful to my NREC family namely Rich, Rob and Sclafani for being my family away from home. I cherished each day that I worked at NREC gaining all the technical knowledge I needed to succeed in my graduate journey. I will also be grateful for all the holiday events that I got to celebrate with you all that went a long way in making me feel less homesick.

I want to thank all my WAMI group members for the joyous and intellectual experiences I have shared with them.

I would like to thank my parents and my wife Mabel for being patient and supportive throughout my graduate journey. Without their unconditional support and love I would not have been able to complete this journey.

TABLE OF CONTENTS

LIST OF TABLES

LIST OF FIGURES

ABSTRACT

Reconfigurable radio frequency (RF) devices are attractive for miniaturization of wireless components and systems by handling functionality of multiple distinct devices. Existing reconfiguration techniques rely on device loadings with semiconductor diodes, ferrite/ferroelectric materials, and microelectromechanical system (MEMS) switches and capacitors. However, it is well-recognized that these techniques cannot fully address important system metrics such as high efficiency, wide frequency tuning range, high power handling capability and cost. Therefore, novel alternative techniques are highly desirable to advance the state of the art in reconfigurable RF devices. The aim of this dissertation is to investigate the novel concept of microfluidically loaded reconfigurability within the context of RF antennas and imaging systems. The proposed devices operate based on continuously movable microfluidic loads consisting of metal (liquid/solid) and dielectric solutions. Microfluidics and microfabrication techniques are utilized with flexible/rigid multilayered substrates to maximize the reconfigurable loading effect on the devices and enable highly reconfigurable antennas and imaging array realizations. Specifically, a wideband frequency tunable monopole antenna is introduced by utilizing continuously movable liquid metal within the microfluidic channel as a length varying conductor. By resorting to ultra-thin channel walls, the liquid metal volume overlapping with the microstrip line feed is utilized as a non-radiating capacitive excitation point to achieve the realized 4:1 (1.29GHz – 5.17GHz) frequency tuning range. Subsequently, an alternative design that replaces liquid metal volume with a microfluidically movable metallized plate is introduced. This novel liquid-metal-free

implementation alleviates the liquid metal associated drawbacks of reliability, long-term device operation, and efficiency. The antenna is shown to provide 2:1 (1.6GHz – 3.3GHz) frequency tuning range with > 87 % radiation efficiency. Due to the high radiation efficiency, the antenna is also capable of handling 15 W of RF power which is 10 W more than its liquid metal counterpart. This metallized plate approach is also suitable for reconfiguration of miniature antennas, and this is demonstrated with the design/implementation of a microfluidically reconfigurable top loaded monopole antenna. It is also suitable for reconfiguration of other structures such as textile antennas – and this is demonstrated with a 0.8GHz to 1.4GHz frequency reconfigurable textile antenna realization. The last section of the dissertation introduces a novel surface imaging array realization by utilizing the microfluidically reconfigurable metallized plate as an RF read-out circuit component. Specifically, a 24 element imaging array is designed and validated to operate within 6 – 12 GHz band with subwavelength resonators to demonstrate the possibility of constructing low-cost high-resolution microwave surface imaging arrays by utilizing the microfluidics based reconfiguration techniques. The presented work emphasizes system level implementation of the proposed devices by integrating them with micropump units, controller boards, and investigating their reliability performances under higher power RF excitations.

CHAPTER 1: INTRODUCTION

1.1 Motivation

Reconfigurable radio frequency (RF) antennas and filters have drawn growing interest to enable compact and light weight multifunctional systems for wireless communications, sensor networks and biomedical imaging systems. Some of the key performance metrics of these RF devices include 1) compact size; 2) cost; 3) power handling; 4) frequency tunability bandwidth; 5) scanning range; 6) reconfiguration speed; 7) radiation efficiency; and 8) frequency agile capability. Recent literature has extensively investigated the reconfiguration capabilities offered by material loadings [1-3], varactors [4-6], PIN diodes [7-9], ferroelectric varactors [10-12], microelectromechanical systems (MEMS) switches and MEMS capacitors [13-19]. These techniques are well recognized to offer compact and cost effective high reconfiguration speed. However, they continue to exhibit drawbacks in terms of several RF performance metrics such as the range of frequency tunability, power handling capability, and radiation efficiency. Semiconductor and ferroelectric varactors result in low efficient RF device implementation with small frequency tuning ranges [9, 10]. Their power handling capabilities are also limited with the device size and third order intermodulation products. MEMS capacitors and switches enable low loss device implementations, however they do not provide continuous frequency tunability [11] and high power handling capability [12, 13]. Implementing imaging systems using MEMS and PIN diodes is costly due to substantial hardware requirements in terms of RF switch components, control circuits and bias networks. Novel alternative techniques that address the overall

performance needs of reconfigurable RF devices are highly desirable in order to advance their capabilities. This dissertation effort specifically proposes to investigate the novel concept of microfluidically loaded reconfigurability within the context of RF antennas, and imaging systems.

1.2 Brief Overview of Existing Technology

1.2.1 Frequency Reconfigurable Antennas

Frequency reconfigurability of electrically small antennas can enable development of smaller form software defined radios and spectrum aware systems. Material loadings [3], ferroelectric varactors [5, 6, 15], RF MEMS switches [8, 11] and RF MEMS capacitors [7,12] are currently the main technologies that are being extensively investigated for realizing tunable RF antennas. Literature survey reveals that frequency tunability ranges of varactor loaded antennas are below 2:1. RF MEMS can be used to extend the range by physically changing the structural shape of the RF devices but reconfiguration only happens at discrete frequency steps due to the practical challenges of incorporating a high number of switches. The performance of these state-of-art frequency reconfigurable RF devices are well recognized to be limited by the tunability and power handling capabilities of their varactors and switches. Due to their potential for addressing such needs, microfluidics based reconfigurability has recently drawn attention for implementation of reconfigurable antennas. For example, stretchability of the liquid metal filled polymer substrates have been demonstrated for frequency tunable and flexible antennas [20-22]. Loading of antenna substrates with different type of liquids exhibiting diverse permittivity values has been proposed for frequency reconfigurability [23]. A continuously movable liquid metal slug inside plastic tubing has been used as a parasitic director to generate beam steering from a circular loop antenna [24] and a frequency tunable Yagi-Uda monopole array [25]. Microfluidically repositionable liquid metal patch antennas have been utilized behind microwave lenses to generate beam-

scanning mm-wave focal plane arrays [26]. However, microfluidics based reconfigurability being an emerging technology still has many practical concerns which need to be addressed. A major goal of this dissertation is to advance the state of such reconfigurable antennas from simplistic conceptual laboratory prototype demonstrations to system level integrations by employing microfabrication, packaging and controlling techniques.

1.2.2 Microwave Imaging System

Current mm and sub-mm imaging approaches utilize a single or a small number of detectors to acquire 2D images by making use of mechanical raster scans [27-30]. The image information is collected through the use of rotating mirrors or translation stages that are controlled using slow precision motors. Consequently, the overall system becomes costly and bulky. In addition, these systems require a significant amount of time to acquire high resolution images. These provide a hindrance to their implementation in real-time monitoring systems. In order to alleviate the issues regarding real time imaging recent literature review suggests employing tightly packed arrays of direct mm-wave detectors behind extended hemispherical lenses. In these approaches an imaging pixel consists of an antenna coupled to a rectifying device such as micro-bolometer [31], hetero structure backward diode [32], or metal-insulator-metal junction [33]. Although direct detection allows for a compact pixel size by removing the need for filters, local oscillators and mixers, the DC pads incorporated within the pixels to extract the rectified THz signal become as large as the antenna itself beyond 200GHz due to size limitations imposed by the flip chip technology [34]. In this dissertation a novel approach of microfluidically loaded microstrip lines for convenient realization of RF read-out circuitries for large format sub-wavelength imaging arrays is investigated for the first time. The proposed microfluidically controlled parasitic RF loads will essentially act as RF shorting circuits when the microchannels

are separated from the microstrip lines with a thin insulator layer. As part of this dissertation further investigation will be made to develop a system level implementation of this proposed imaging array. RF measurements circuitries, microprocessor controller, micropump unit, software interface with computers for back-end data processing and other necessary components will be built on a single board along with the imaging array.

1.3 Contributions

Microfluidic based reconfigurability has been demonstrated to offer many potential advantages but there are several challenges related to their fabrication, packaging, power handling capability, actuation, reliability and repeatability that need to be addressed. This dissertation addresses these challenges through;

(a) the development of unique fabrication procedures that help in packaging and integration of microfluidic channels onto conventional printed circuit boards,

(b) implementing frequency tunable antennas using metallized plates as the radiating/switching element which improve their power handling capability and reliability,

(c) integrating electronically switched micropumps for accurate control over movement of metallized plate inside a microchannel,

(d) demonstrating system level implementation of the reconfigurable devices by integrating them with controller boards, micropump units, and software interfaces.

1.4 Dissertation Organization

The outline of the dissertation is as follows:

(a) Chapter 2 gives background on conventional methods for implementing frequency tunable antennas.

(b) Chapter 3 presents a wideband frequency tunable liquid metal monopole. Specifically, the antenna is demonstrated to have a 4:1 (1.29GHz- 5.17GHz) tuning range with a tuning speed of 252MHz/sec.

(c) Chapter 4 describes a monopole antenna in which a metallized plate is used as the radiating element instead of liquid metal. The higher conductivity of metalized plate increases the power handling capability of this monopole antenna over the previous implementation. To show this, the power handling capability of these monopole antennas are studied for the first time through multiphysics simulations and experiments. Specifically, the presented monopole operates over a wide frequency tuning range from 1.7GHz to 3.5GHz (~2:1) with a measured realized gain >2.4dB. It exhibits 200% more power handling capability as compared to the prior implementation.

(d) Chapter 5 describes a microfluidically switched dipole antenna. The switching element is implemented using a selectively metallized plate. By moving the plate over the antenna trace it modifies the electrical length of the current on the dipole thereby tuning its frequency. The chapter further describes this switching technique being applied to a textile version of the dipole.

(e) Chapter 6 describes a microfluidically switched surface imaging system at microwave frequencies. The imaging system consists of a 1D array of complementary open loop resonators being interrogated individually using a metallized plate. 2D imaging capability is achieved by using a stepper motor controlled stage. The system is interfaced to a computer using LabVIEW for back-end data processing. A patterned printed circuit board is imaged using the imaging system to demonstrate its operation and resolution.

(f) Chapter 7 concludes this dissertation.

CHAPTER 2: BACKGROUND

2.1 Introduction

This chapter presents a review of the different technologies that have been traditionally used for implementing frequency tunable antennas. The advantages and disadvantages of the respective technologies have been summarized. A review of the recent interest in using microfluidics for implementing frequency tunable antennas has also been presented. This chapter highlights the advantages of microfluidic based tunability with reference to relevant examples. The chapter concludes summarizing the challenges that have not yet been addressed by it which paves the way for the works presented in the following chapters.

2.2 Frequency Tunable Antennas

The demand for multifunctional systems are continually growing with the rapid progress in the field of communications. Traditional systems that were meant for single frequency of operation are being replaced with systems capable of utilizing access over a wide spectrum of frequencies. These modern portable wireless systems require antennas that can cover multiple frequencies. Frequency tunable antennas that can alter its radiating frequency without affecting its other parameters such as radiation efficiency, field pattern have been viewed as a blessing for such systems. Such antennas can replace a number of single-function antennas thereby reducing the overall size, cost, and complexity of a system while improving performance. Implementing such frequency tunability has been achieved using various techniques which have been described in the following sections.

2.2.1 Frequency Tunability Using RF-MEMS Switch and Capacitors

Frequency tunable antennas implemented using RF-MEMS (Radio Frequency Micro-Electro Mechanical Systems) switches and capacitors have garnered a lot of interest [35-41]. This tuning technique offers the advantages of low insertion loss, low power consumption by the bias network, fast switching speeds, high Q-factor and ease of integration on low dielectric substrates. In [35] a frequency reconfigurable antenna is presented which can operate in two different frequency bands (700MHz and 4900MHz). The planar inverted F-antenna is reconfigured between the two frequency states using a single RF MEMS switch placed strategically along the antenna geometry. The switch is used to alter the path length of the current on the antenna which in turn enables the antenna to reconfigure its operating frequency. A 2-bit Ka band frequency tunable slot antenna has been demonstrated in [36]. The coplanar waveguide fed slot antenna can be tuned to different frequency states over 28GHz-35GHz using the RF MEMS switches placed along the radiating slot. The RF MEMS switch when actuated shorten the length of the radiating slot thereby increasing the resonant frequency of the antenna. Apart from changing the electrical path or antenna aperture RF MEMS capacitors have been used to tune the operating frequency of the antenna [37]. The presented slot antenna is loaded with a stub on which MEMS variable capacitors are placed periodically. The capacitors are used to change the electrical properties of the stub i.e., characteristic impedance and electrical length which in turn affect the resonant frequency. Different from the previously mentioned approaches, in [38] a five band reconfigurable PIFA antenna for mobile phone applications has been introduced which uses the technique of loading or re-matching the antenna externally using RF MEMS switches. This technique provides the attractive option of reconfiguration implemented entirely in the circuit domain since all switching and biasing circuitry is kept off the antenna structure. Another popular method of implementing

frequency reconfiguration using RF MEMS switches is the pixel antenna concept [39-41]. The main radiating antenna geometry is discretized into small sections, called pixels, and interconnected by means of RF-switches. By activating different switch configurations, the antenna surface is reshaped, thus reconfiguring its frequency and radiation characteristics. It has also been proposed that instead of discretizing the antenna, a parasitic pixel layer capable of reconfiguring the resonance frequency can also be used leading to significant advantages in switch biasing, power handling and integration possibilities.

2.2.2 Frequency Tunability Using PIN Diodes

Frequency tunable antennas implemented using the switching technique mentioned in the previous section have also been developed using PIN diodes as the switching element. PIN diodes offer the advantages of higher breakdown voltage, low RF on resistance, fast switching which make them very lucrative as RF switches [42-46]. A compact planar reconfigurable slot antenna has been shown to operate over a wide tuning range of 1.7:1 using PIN diodes [42]. A single-fed resonant slot loaded with a series of PIN diode switches forms the antenna whose tuning is realized by changing its effective electrical length. This is done by controlling the bias voltages of the PIN diodes along the slot antenna. Planar inverted F-antennas (PIFA) which have gain widespread attention on account of their suitability for mobile applications stand to benefit a lot from frequency tunability. This has been demonstrated in [43] through a PIFA loaded with a PIN diode wherein no separate dc control unit for the switch is needed. The dc voltage is carried to the switch simultaneously with the RF signal. The antenna covers the frequency ranges appropriate to the GSM850, GSM900, GSM1800, PCS1900, and UMTS telecommunication standards.

The incorporation of PIN diodes as part of the radiating element requires placing biasing lines in the antenna radiating plane. This can lead to undesirable resonances in the antenna

operating band as well as changes in the antenna radiation pattern if the bias lines are not designed properly. Several techniques addressing this challenge have been proposed [44-47]. In [44] a novel design technique of placing the PIN diodes on the ground plane has been discussed. In this technique the ground plane of the microstrip monopole antenna is modified by strategically placing the PIN diodes to obtain triple band coverage. The feed line and the main radiating square stub are left untouched which mitigate degradation of input matching and radiation as the antenna is switched. Furthermore, reconfigurable filtering antennas (filtennas) have also been introduced as a solution to avoid placing the switching components on the radiating antenna part [45,46]. This is done by incorporating a tunable bandpass filter in the antenna feed line. The filter is reconfigured using PIN diodes. In [45] a filtering slot antenna covering 2.1GHz long term evolution (LTE) and 2.4GHz wireless fidelity (Wi-Fi) bands is shown while [46] shows a similar antenna being tuned over 5.2GHz to 5.5GHz. In such filtennas the integration of the antenna and the bandpass filter reduces the effect of the bias lines and leads to more compact devices and improves the performance of the RF front ends.

2.2.3 Frequency Tunability Using Varactor Diodes

Electrically tunable antennas have been implemented using PIN diodes and RF MEMS switches as shown in the previous sections. Varactor diodes have become a popular choice for implementing such electrically tunable antennas on account of several reasons. They consume less dc power because of their low current consumption, they can be easily integrated with antennas due to their small package sizes and are available commercially in wide variety. These advantages are highlighted by implementing a varactor loaded H-shaped microstrip antenna (HMSA) [47]. In this design the multi-band functionality of the antenna is achieved by careful selection of the position of the varactors so that for a specific range of the varactors' bias voltages, a specific mode

of the multi-mode HMSA is matched, whereas the other modes are mismatched. To show the further advantages of using varactors in developing frequency tunable antennas, a slot loop antenna is discussed in [48]. Slot loop antennas have the inherent advantage of being uniplanar which makes it easier to fabricate but at the same time it is difficult to obtain wideband matching over the entire tuning range. Using varactor tuned matching network a single coplanar waveguide feed to the antenna is implemented and demonstrated to have a wide tuning range of 6.71GHz to 9.14GHz. To obtain even wider tuning range of 1.5:1 a stub loaded varactor tuned microstrip antenna is demonstrated in [49]. The square microstrip patch is loaded with 12 identical stubs distributed evenly along the 4 edges. The stubs are connected to the square patch using varactors. This approach allows to simultaneously vary the resonance frequency in vertical and horizontal directions with two independent reverse bias voltages. Novel antenna design methodologies have also been investigated to further extract the utility of using varactors. In [50] a dual band slot loop antenna is proposed. By loading the slot edge with varactors, the phase of edge current is affected, and so are the resonant frequencies of the slot. In [51] a miniaturized printed planar antenna using split-ring resonator to form a dual-band frequency-tunable antenna is shown. By carefully choosing the position of loaded varactors high isolation between the high band and the low band are achieved with independent tunability of each bands.

2.2.4 Frequency Tunability Using Tunable Materials

The use of tunable materials in developing frequency reconfigurable antennas is a relatively new field. Though the proliferation of these type of antennas has been hindered by challenges such as reliability and efficiency of the antennas, several promising prospects have been reviewed in this section. In [52] a ferroelectric dielectric based antenna is shown which can be tuned by varying the applied DC voltage. The dielectric constant of the ferroelectric material is

modulated by varying the applied electric field in a direction perpendicular to the propagation of the signal. At microwave frequencies similar technique of voltage modulated antenna is shown which uses liquid crystal as the substrate [53]. The antenna can be tuned from 34.1GHz to 37.7GHz by varying the applied DC voltage from 0V to 90V. The use of liquid crystal at microwave frequencies is facilitated by their low power consumption and lower loss [54]. Another approach which demonstrates frequency tunability while miniaturizing the antenna at the same time is by using magneto-dielectric materials as the antenna substrate [55]. The 3D inverted F-antenna can be tuned to cover the DVB-H frequency band.

2.2.5 Frequency Tunability Using Mechanical Reconfiguration

The frequency tunable antenna topologies discussed above utilize lumped tunable components. In these approaches the non-linearity of the tuning element, added loss as well as difficulty in maintaining the radiation properties limit the operation of the antennas over a wide tuning range (>2:1). Recently in applications where RF switches are not desired due to the additional power losses and complexity of the bias lines, mechanically tunable antennas have been being investigated [56-58]. The mechanically tunable antennas are promising devices as they can provide reduced RF loss, higher isolation, and better linearity with respect to antenna structures integrated with electronic switches. In [56] a dual-band tunable slot antenna is presented with a tuning ratio of 2.6:1 is obtained. The tunability is accomplished by employing a rack and pinion mechanism to slide parasitic patches over the antenna to vary the slot lengths and thus the frequency of operation of each band. A new method of employing planar Hoberman linkages on top of a circular microstrip antenna is shown in [57]. The linkages are used to move parasitic patches on top of the circular microstrip antenna to vary its operating frequency from 2.25GHz to 3.02GHz. Multilayer stretchable conductors which retain their conductivity under strain have been

used to build low-cost and robust frequency tunable antennas [58]. The conductors which are formed by combining a thin layer of rubber and metal exhibit high conductivity with large elasticity. Antennas build on such substrates can be made to operate at different operating frequency by applying strain that physically stretches the antenna geometry.

The tunability of antennas implemented using the above mentioned techniques satisfy most of the requirements of a frequency tunable antenna. However, there are some aspects such as the range of frequency tunability, power handling capability, and radiation efficiency that are still not addressed by them. On account of their ability to potentially address these shortcomings microfluidics based reconfiguration has been pursued with great interest by many researchers in recent years. Microfluidics based reconfigurable antennas have been demonstrated to have wider tuning range and higher power handling capability than those obtained using the conventional techniques discussed above. In the following section the concept of microfluidics and its varied applications in the field of biomedical research has been presented. This is followed by a review on current state-of-the-art of microfluidically tunable antennas.

2.3 Microfluidics

Microfluidics found its origin in microbiology where it was used as a tool to manipulate very small volumes of samples and reagents. This was a very compelling feature for microanalysis as it opened up the possibilities to implement several functions in a small and yet cheap device. With further progress in microfluidics research these devices were used for fast and in-situ detections of bacteriological threats. The growth of these devices was further stimulated by incorporation of well-developed microfabrication techniques for their production. Though the initial devices were based on silicon and glass on account of their compatibility with

microfabrication techniques soon they were replaced with soft polymers due to their lower cost, higher biocompatibility and other physical properties such as flexibility and optical transparency.

2.3.1 Materials

Microfluidic devices have been built using many different materials over the years. The different materials, their advantages and disadvantages have been summarized as follows:

- Silicon was one of the first materials to be used for building microfluidic devices on account of its compatibility with standard microfabrication processes. Silicon possesses many advantageous qualities such as thermal conductivity, surface stability and solvent compatibility. However, the opacity of silicon to the visible electromagnetic spectrum made its adoption into microfluidics difficult. The etching of the microfluidic channels in silicon requires complex manufacturing processes such as wet anisotropic etching or deep reactive ion etching (DRIE) which hinder low cost rapid prototyping.
- Possessing similar qualities as of silicon, glass came into being the popular material of choice for fabricating microfluidic devices as it was optically transparent. Properties such as high pressure resistance, hydrophilic surface, electrical insulation, biocompatibility made it a lucrative option. The higher cost of the raw material coupled with the long isotropic wet-etching time to define the channels though marked its limitations.
- The difficulty in integrating silicon and glass into microfluidics paved the way for a new class of materials called polymers. Polymers helped bridge the gap between the ideal material for microfluidic devices and glass/silicon. They can be mass produced using soft lithography, hot embossing, and injection-molding techniques which make rapid prototyping much easier. In addition, polymers have lower cost, transparency in the visible/UV spectrum, and surface modification possibilities. The different types of

polymers that have been used for microfluidic devices are polydimethylsiloxane (PDMS), polystyrene (PS), polycarbonate (PC), polymethymethacrylate (PMMA). In this dissertation PDMS has been used for fabricating all the microfluidic channels due to its surface modification properties when exposed to oxygen plasma. This was a key enabler in developing the reconfigurable RF devices and will be discussed in detail in the following chapters.

2.3.2 Applications

Microfluidic devices due to their ability to precisely control very small volumes of liquids have found many applications in the biomedical field. One of its main applications has been to develop lab-on-chip devices. These devices can integrate all the functionalities of a laboratory on a single chip. The usefulness of such devices is evident by following their adoption in different biomedical applications such as pH control, cell analysis, and drug administering. For example, in cell culture experiments having a controlled environment is of utmost importance and one of the prime factors that needs to be monitored is the pH of the medium. Researchers have been able to control precisely the pH of such environment using microfluidic devices. These devices use ion-sensitive field-effect transistor (ISFET) coupled with pulse modulated lab-on-chip valves. The transistor sense the change in pH which is used as a feedback to the control valves. The valves regulate the flow of different solutions into the microfluidic device to control the pH of the cell environment. Probably the application that best summarizes the advantages of lab-on-chip devices is point of care testing (POC). POC means medical analysis that can be carried out at the patient site. The intrinsic features of microfluidic devices such as low consumption of reagents and sample, miniaturization of device, disposable and low-cost make them ideally suited for POC applications. More recent application of microfluidics is towards developing reconfigurable RF

devices with functionality that are more advanced than classical reconfigurable ones. The linear nature of the reconfiguration technique makes them ideally suited for high power applications. The next section presents a review of such devices.

2.3.3 Frequency Tunability Using Microfluidics

Frequency tunable antennas reconfigured using microfluidics have recently drawn attention on account of their significant advantages as compared to ones implemented using diodes, varactors and MEMS. A review of relevant work shows various types of antennas demonstrating frequency tunability using microfluidic tuning [59-77]. In these antennas the microfluidically controlled loads acting as either shorting, loading, or main radiating element are moved using different actuation mechanisms. The following section presents examples of such antennas to help readers develop better understanding about their working principle.

In the shorting based approach liquid metal is used as the microfluidically controlled shorting switch. This technique has been used to implement frequency tunable patch [59] and slot antennas [60]. The frequency tunable patch antenna uses eutectic-indium gallium (EGaIn) filled channels as the switching element. The channels filled with liquid metal are bonded to the top of the microstrip patch antenna. When pressure is applied to the liquid metal it flows inside the channels to alter the electrical continuity across three gaps on the antenna geometry. This elongates the antenna and tunes it from 2.4GHz to 1.6GHz. For the frequency tunable slot antenna, a microfluidic channel is placed perpendicular to its length. The pressure driven channel is filled with liquid metal (EGaIn) to shorten the length of the radiating slot and thereby tune its resonating frequency. In such shorting based approaches oxidization of the EGaIn (liquid metal) has been seen to be the most pressing concern. To minimize the residue left behind by EGaIn inside the

microchannels, researchers have investigated use of different carrier liquids and microchannel surface coatings as potential solutions [61].

In the loading based approach, microfluidically controlled loads are placed on top of the radiating antenna to alter the electromagnetic fields, thereby changing its resonating properties. These reactive loads can either be liquid metals [62, 63] or liquid dielectrics [64, 65]. Slot antennas have been seen as the preferred type for implementing such reactive loading based frequency tunable antennas [62-67]. In [66] a reconfigurable CPW fed folded slot antenna was realized by loading liquid metal bridges across the radiating slot. The position of the liquid metal bridges is determined based on the desired resonating frequencies. By filling or emptying of the respective bridges, the antenna is shown to resonate at 2.4GHz, 3.5GHz and 5.8GHz. Similar technique of reactive loading of a dual band slot antenna is seen in [67]. The antenna consists of two slots for its dual band operation. Each of the two slots can be loaded with reactive liquid metal loads, one for providing lower band tuning of 1.8GHz to 3.1GHz and the other for upper band tuning from 3.2GHz to 5.4GHz. The antenna can provide a frequency coverage ratio of 3:1. Apart from liquid metal, liquid dielectrics have also been shown as effective loads for tuning the resonant frequency of slot antennas. In [65] the surface of an annular slot antenna is integrated with microfluidic channels. The first and the second resonant frequencies can then be independently tuned by flowing liquid dielectrics such as acetone and de-ionized water through the channels. The antenna shows tunability from 3.3GHz to 4.2GHz for first resonance and 5.2GHz to 8GHz for the second resonance.

In more examples of liquid metal based loading technique patch antennas have also been investigated by researchers [68, 69]. The frequency tunable patch antenna demonstrated in [68] consists of a U-shaped slot etched into the ground plane. Microfluidic channels are placed directly

aligned with the slot. By filling the channels with liquid metal using pressure driven syringes the reactive loading of the slot is diminished. This increases the resonant frequency of the antenna from 1.85GHz to 2.07GHz. Similar pressure driven technique of moving liquid metal cylindrical loads to tune a dual band patch antenna is shown in [69]. In this approach channels filled with liquid metal are placed along the non-radiating edge of the antenna. As the liquid metal cylinder inside the channel moves under the patch antenna, the antenna demonstrates dual band behavior. The separation between the lower and upper band increases with increase in the overlap distance. The antenna can achieve frequency coverage ratios in the range of 1.08 to 1.3.

The microfluidic loads can also be used as the main radiating component of the antenna. In such applications liquid metals are an attractive choice as their inherent property of taking the shape of the channel they are pumped into helps to define the antenna geometry [70-74] (shape, dimensions). To demonstrate the concept, the simplistic example of a monopole antenna is discussed in [70]. The radiating frequency of the monopole antenna is defined by its length. The volume of liquid metal being pumped into the capillary is controlled by using electrochemical actuation. This changes the length of the monopole thereby tuning its resonating frequency over a 0.66GHz to 3.4GHz bandwidth. Similar actuation technique is applied to implement a frequency tunable crossed dipole antenna [73]. In this work DC voltage is applied to each arm of the dipole to shorten or lengthen the liquid metal slugs in the respective arms. The linearly-polarized resonances of the antenna can be tuned over 0.8GHz to 3GHz. It can be switched to circular polarization and tuned over 0.89GHz to 1.63GHz. In addition to using liquid metal as the movable element, frequency tunable antennas defined using static liquid metal can also be found in relevant works [75-77]. In these cases, the liquid metal is filled into elastomeric channels to define the shape of the antenna (patch [75], dipole [77]). The frequency tunability is then achieved by

physically stretching the liquid metal filled elastomer. The self-healing property of liquid metal ensures that the antenna stretches without any discontinuities being formed.

2.3.4 Challenges with Microfluidic Based Tunability

The review of current state-of-the-art microfluidic based tunable antennas has demonstrated their several advantages however, there are still many challenges that need to be addressed. These include fabrication of the device, actuation and accurate control over the movement of the microfluidic load inside the channels, power handling capability of the antennas, their reliability and repeatability.

2.3.4.1 Fabrication

The microfluidic channels are generally fabricated in the elastomer polydimethylsiloxane (PDMS) using standard soft-lithographic technique. The issue arises when these channels need to be integrated on top of the printed circuit board (PCB). The PCB has the antenna or the feed line etched on it. To obtain tunability the microfluidic load needs to electromagnetically couple to the antenna/feed line. In each of these cases the distance between the microfluidic load (inside the channel) and the copper (etched on top of the PCB) needs to be very small to ensure good coupling between them. In most of the relevant works mentioned in the review on frequency tunability using microfluidics, a thin layer of spin-coated PDMS is used as the bonding layer between the channel and the PCB. The PDMS coated PCB is exposed to oxygen plasma which modifies its surface properties making it conducive to covalently bond to the channel surface (also made using PDMS and exposed to oxygen plasma). Although this technique ensures close separation between the channel and the PCB, the increased loss of intermediate PDMS layer makes the antenna more lossy (especially at higher frequencies) and thereby lowers its efficiency. New bonding materials need to be investigated which have a lower loss than PDMS and also higher thermal conductivity. The

increased thermal conductivity is needed to ensure that the antennas can operate at high input power conditions as it is one of the significant advantages of using linear microfluidic devices.

2.3.4.2 Actuation

The antennas implemented using movable microfluidic loads require an actuation method to achieve the desired tuning capability. The method implemented should be repeatable and enable accurate positioning of the movable loads. The positioning is extremely important as it affects the response of the antenna. Pressure driven systems discussed in the literature review mostly employ manual syringes as the actuation mechanism. While this simplistic approach is suitable for experimental purposes, they need to be replaced with low power and electronically controlled systems that can apply the hydraulic pressure. The electronic control will help in automatic tuning of the antenna based on the desired resonant frequency while low power is essential requirement for any stand-alone portable system.

2.3.4.3 Power Handling Capability

Antennas generally have two power specifications, operating under high peak power for short duration and, high average power for long duration. Microfluidic based antennas are expected to withstand such power handling requirements due to their linear tuning scheme. Further experiments need to be performed to support this as well evaluate the failures that can occur due to the high power levels. It would also help to develop and verify thermal simulation models similar to their electromagnetic counterparts that can predict the maximum power levels a particular antenna can handle.

2.3.4.4 Reliability and Repeatability

The liquid metal based microfluidic antennas offer significant enhancement in terms of tuning range compared to other methods. There is however still some concern over the reliability

and repeatability of these antennas. The liquid metals (EGaIn, Galinstan) used in these applications tend to get oxidized very easily and leave residue inside the channels making continuous movement challenging. Alternative techniques need to be investigated that can alleviate such issues.

2.4 Conclusion

In this chapter a brief review of frequency tunable antennas and the techniques used for implementing them has been presented. The concept of microfluidics and its varied applications in the field of biomedical research has been discussed to help readers develop a better understanding regarding this technology. Then the advantages of using microfluidics in the context of reconfigurable antennas has been highlighted. A detailed review of frequency tunable antennas implemented using microfluidic reconfiguration is performed. The chapter concludes with the challenges still faced by microfluidic based tunability. The solutions to such challenges will be presented through the implementation of reconfigurable antennas in the following chapters.

CHAPTER 3: WIDEBAND FREQUENCY TUNABLE LIQUID METAL MONOPOLE ANTENNA

3.1 Note to Reader

Portions of this chapter have been previously published in [78,79], and have been reproduced with permission from IEEE. Permission is included in Appendix A.

3.2 Introduction

The demanding size reduction needs of multifunctional communication systems have generated interest in reconfigurable antenna technologies. A reconfigurable antenna can potentially alleviate the need for multiple antennas by providing versatility in terms of frequency, bandwidth, polarization, and radiation pattern. As reported in the literature review in the previous chapter the reconfiguration capabilities offered by material loadings [1-3], varactors [4-6], PIN diodes [7-9], ferroelectric varactors [10-12], microelectromechanical systems (MEMS) switches and MEMS capacitors [13-19] have been extensively investigated. Due to their drawbacks in terms of range of frequency tunability, power handling capability, and radiation efficiency alternative reconfiguration techniques are being investigated. In this regard microfluidics based reconfigurability has recently drawn attention for implementation of such reconfigurable antennas. In this chapter a liquid metal monopole antenna that can dynamically change its length to provide significant frequency tunability has been introduced [78]. Since liquid metals are known to react with conventional metals used in printed circuit boards, a key enabler of this monopole antenna was the realization of its feeding mechanism with capacitive coupling that ensures the isolation of

the liquid metal volume. The high level of RF coupling between the microstrip line and the antenna was accomplished by manufacturing the microfluidic channels by bonding a 1 mil (=25.4μm) thick low loss liquid crystal polymer (LCP) substrate with a relatively thick (~2mm) Polydimethylsiloxane (PDMS) substrate. A detailed investigation of the antenna concept introduced in [30] is presented. Furthermore, an enhanced 4:1 (1.29GHz to 5.17GHz) frequency tuning range is achieved by resorting to a different feed coupling scheme [79]. A system level implementation of the 4:1 tunable antenna with external micropumps is presented. Microfluidic channel dimensions used for the antenna implementation are selected through detailed flow characterizations to achieve a high frequency tuning speed with reliable liquid metal volume movement. The antenna is shown to operate with a tuning speed of 242.5 MHz/s and exhibit >1.3 dB measured realized gain across its frequency tuning range.

The presented frequency tunable monopole antenna also allows for high gain antenna arrays that could be reconfigured to operate over a wide frequency tuning range. Most importantly, when resorted to meandered or interconnected microfluidic channels, the implementation of such arrays can again be accomplished by using a single bi-directional micropump unit. To demonstrate this capability, in this chapter, a 4×1 linear broadside array operating from 2.5GHz to 5GHz is designed and experimentally verified. The array is shown to operate with measured >6 dB broadside gain and a tuning speed of 125 MHz/s. The chapter is organized as follows. Section 1.2 introduces the liquid metal monopole implemented using a meandered coupled line approach. The design and fabrication details are discussed along with the experimental verification of the monopole. Section 1.3 introduces the 4:1 frequency tunable liquid metal monopole antenna concept and carries out an example design based on computational simulations and experimental microfluidic channel flow characterization studies. Section 1.4 presents a 4×1 linear broadside

array to demonstrate the potential of the presented technique in realizing wideband frequency tunable high gain antenna arrays. A micropump unit comprising of microcontroller controlled piezoelectric micropumps was developed to facilitate portability of the antenna array.

3.3 Liquid Metal Monopole Using Meandered Coupled Line

3.3.1 Design

Figure. 3.1(a) demonstrates the layered structure of the liquid metal tunable monopole antenna and 3.1(b) shows the top view. A 50mm long liquid metal slug embedded inside a microchannel filled with low loss Teflon® solution is fed by a 50Ω microstrip line printed over a readily available 1.57mm thick Rogers RT5880 substrate. Through simulation based studies carried out with Momentum® suite of Agilent Advanced Design System (ADS), the minimum overlap length that provides sufficient RF coupling between the feed and the liquid metal slug was determined as 5mm. Therefore, the lowest operation frequency for this antenna is achieved at about 1.5 GHz when a 45mm long monopole is realized. When the monopole length is reduced to 5mm, the expected resonance frequency is ~5GHz. The back surface of the feed layer substrate is used as the ground plane. To maintain the radiation pattern of the antenna close to be omnidirectional over this broad frequency tuning range, the width and length of the ground plane was selected to be less than a wavelength at the highest operating frequency. Through simulations, the smallest ground plane size that can provide a good impedance match for the lower end of the tuning range was determined as $25\times30mm^2$. Since tuning is achieved by partially retracting the liquid metal antenna over the feed line, the final design step is to ensure that the enlargement of this overlap area/length does not degrade the impedance matching. A straight microchannel based implementation of this overlap region was found to result in a bad impedance matching performance as shown in Figure. 3.2(a) for frequencies above 3.1 GHz. This was associated with

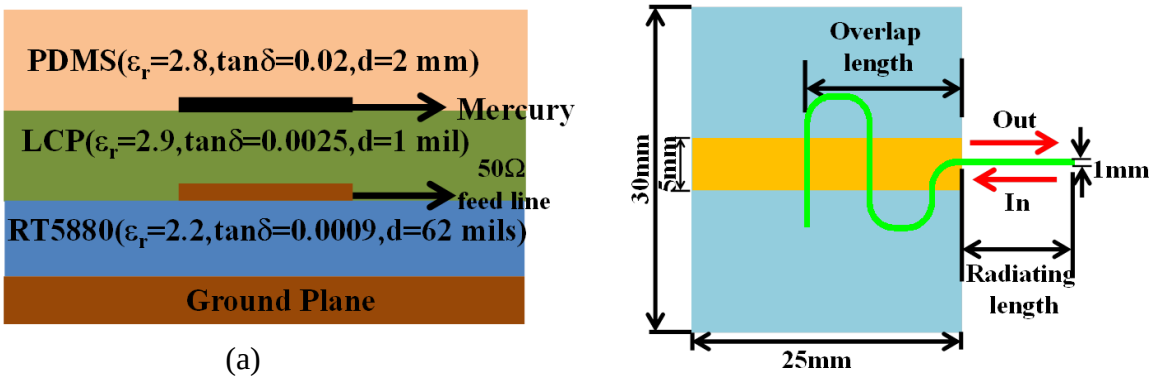

Figure 3.1: Liquid metal monopole antenna. (a) Substrate stack-up; (b) Top view.

the formation of a resonant coupled line structure within the overlap region. To overcome this issue, the shape of the channel retracted over the feed line was meandered. As shown in Figure. 3.2(b), the meandered channel based monopole was able to provide a well matched $|S_{11}|$ (i.e. <-

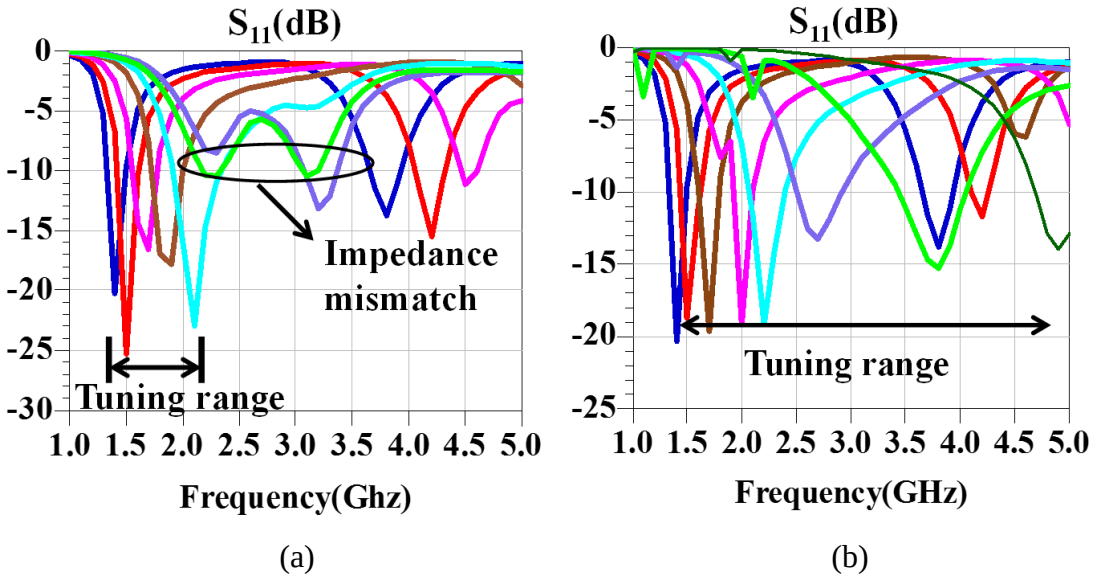

Figure 3.2: Simulated $|S_{11}|$ performance of the liquid metal monopoles exhibiting (a) Straight and; (b) Meandered coupling sections.

10dB) over the entire tuning range of 1.5GHz to 5GHz with peak gain of 2.4dB realized at 4.2GHz. The simulated efficiency was >54% throughout the tuning range.

3.3.2 Fabrication

The mold of the 100μm thick 1mm wide microchannel defining the shape of the monopole antenna was fabricated in 2mm thick PDMS using soft-lithography. To define the inlet and outlet for the liquid flow, 1mm diameter holes were punched into the PDMS mold. Thick PDMS blocks with punched holes acting as microfluidic adapters for PTFE pipes were fabricated separately and irreversibly bonded on top of the inlet/outlet of this PDMS mold using the oxygen plasma treatment. To seal the microchannel, the PDMS mold was bonded to a thin layer of LCP (25μm) using a customized 3-Aminopropyl triethoxysilane (APTES) treatment. The bonded PDMS-LCP pair carrying the microchannel was placed on top of the feed line. To prevent stiction with the microchannel walls, mercury (σ=106 S/m) was employed as the liquid metal. Syringes were utilized for reconfiguring the antenna in the experimental verifications.

3.3.3 Measured Performance

The fabricated antenna is shown in Figure. 3.3(a). The antenna layers were aligned and clamped during the measurements. The snapshots depicting the position of the liquid metal monopole at different operational frequencies are presented in Figure. 3.3(b). The measured $|S_{11}|$ performance agrees well with the simulated performance. Due to the air gaps between the feed board and the antenna substrate, the lowest operational frequency of the antenna was realized at 1.7GHz instead of the simulated 1.4 GHz. By changing the antenna length, the resonance frequency was shifted up to 4.9GHz without degrading the $|S_{11}|$<-10dB impedance matching. Representative normalized E-plane radiation patterns measured at several frequencies are demonstrated in Figure. 3(d). Specifically, the antenna demonstrated an almost stable pattern despite having a fixed size ground plane. In the E-plane, the measured peak realized gain values varied between 2.3dB and 0.5dB.

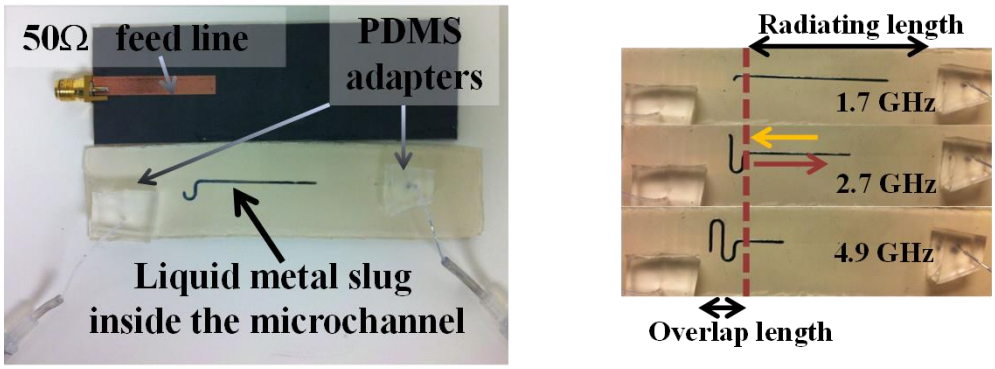

(a) (b)

Figure 3.3: (a) Fabricated antenna; (b) Snapshots of the monopole configured to operate at different frequencies.

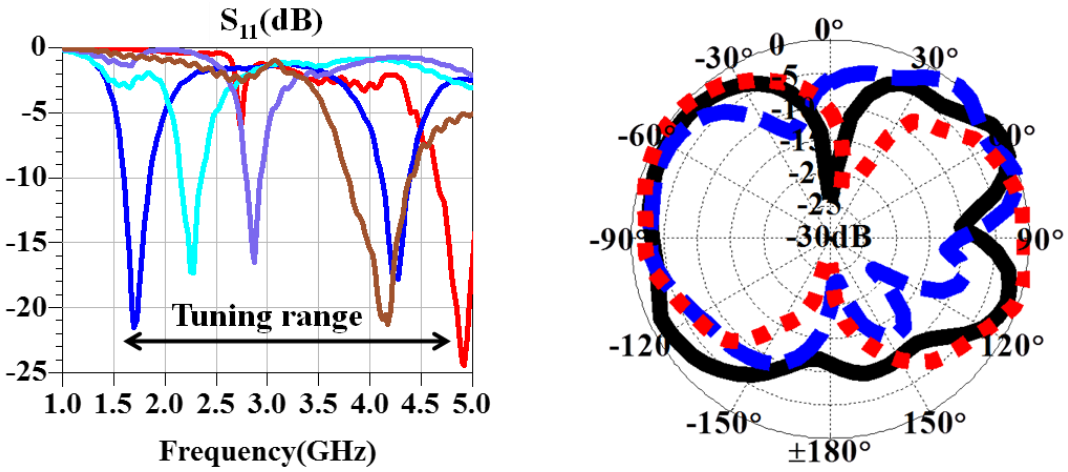

(a) (b)

Figure 3.4: (a) Measured $|S_{11}|$ performance for different radiating lengths; (b) Measured E-plane normalized radiation patterns at different frequencies.

3.4 Frequency Tunable Liquid Metal Monopole Using Tapered Feed Line

In the previous section a monopole antenna using coupled meandered line approach was presented. The antenna tuning range was limited by the appearance of the couple line resonance at higher frequencies. To address this issue in this section a tapered feed line monopole antenna is presented. Figure. 3.5 depicts the 4:1 liquid metal monopole and its substrate stack-up. The liquid metal is enclosed inside a microfluidic channel fabricated within 2 mm thick Polydimethylsiloxane

(PDMS, ε_r=2.8, tanδ=0.02) using soft lithography process. The microfluidic channel is sealed using a 1mil thick (1mil = 0.0001inches = 25.4μm) Rogers Ultralam 3908 liquid crystal polymer (LCP) based substrate layer (ε_r=2.9, tanδ= 0.0025). The LCP layer is bonded to a 62mil thick Rogers RT5880 substrate (ε_r=2.2, tanδ=0.0009) that carries a 50Ω microstrip feed line and ground

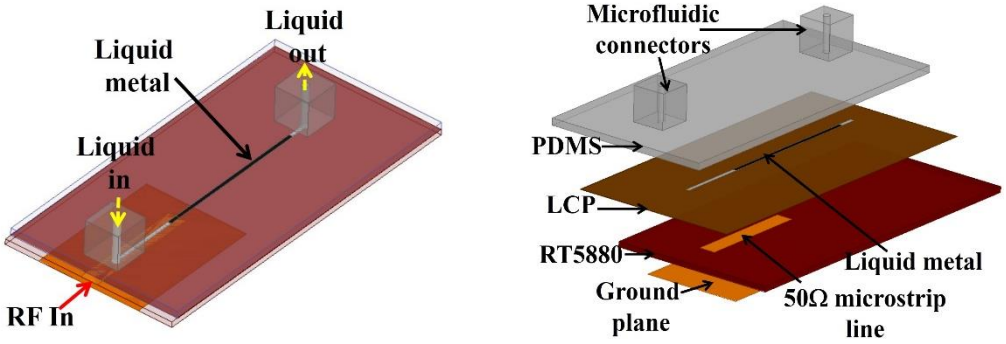

(a) (b)

Figure 3.5: (a) Liquid metal monopole with widened feed; (b) Substrate stack-up.

plane metallization. The microfluidic channel is aligned with the microstrip feed line to generate capacitive coupling through the 1mil thick LCP layer. The non-liquid metal volume of the microfluidic channel is filled with low loss Teflon solution (DuPont AF 2400, 400S2-100). A bidirectional micropump unit is used to reconfigure the physical length of the antenna by

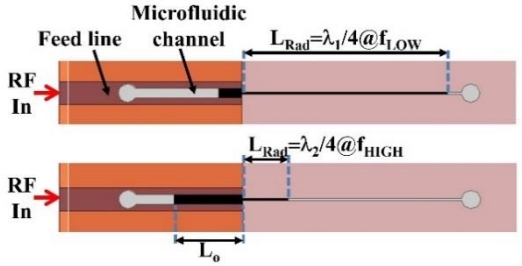

Figure 3.6: Reconfiguration principle of the monopole antenna.

retracting a portion of the liquid metal volume to reside over the microstrip feed line (see Figure. 3.6).

This reconfiguration technique relies on the ability to form a continuous liquid metal slug inside the microfluidic channel. Physically long slugs forming the radiating part of the antenna are necessary for achieving a low frequency of operation and wideband frequency tuning range. On the other hand, a wider overlap area between the microstrip line and the liquid metal slug increases the capacitive coupling necessary to realize a virtual RF short at the feed point. Consequently, the range of realizable liquid metal slug widths and lengths must be identified before proceeding with a specific antenna design. To do so, a series of experiments were performed to determine the maximum realizable physical length and width of the liquid metal slug under different microfluidic channel heights.

3.4.1 Liquid Metal Flow Characterization

To characterize the channel dimension effects on the length of the liquid metal slug, five sets of microfluidic channels were fabricated. Each set included 60mm long microfluidic channels with widths varying from 0.5mm to 5mm. Each set had a uniform channel height. The channel eights among the sets were varied from 100µm to 300µm with 50µm increments. Due to its low-rate oxidization and stiction properties, mercury was utilized as the liquid metal. Syringes were used to accurately transport liquid metal and Teflon solution inside the channels. By increasing the liquid metal volume gradually, the maximum length of the liquid metal slug that can be repositioned inside the channel without any splitting was determined. For example, for the 250µm high channels, the length of the realizable liquid metal slug reduced from 50mm to 6mm as the channel width is increased from 0.5mm to 3mm as shown in Figure. 3.7(a). For wider widths,

Table 3.1 Effect of channel dimensions on length of liquid metal slug

Channel Width (w)	*Channel Height (H)*				
	100µm	150µm	200µm	250µm	300µm
0.5mm	11mm	25mm	36mm	50mm	45mm
1mm	8mm	12mm	17mm	22mm	21mm
2mm	5mm	8mm	15mm	18mm	15mm
3mm	2mm	2mm	3mm	6mm	3mm

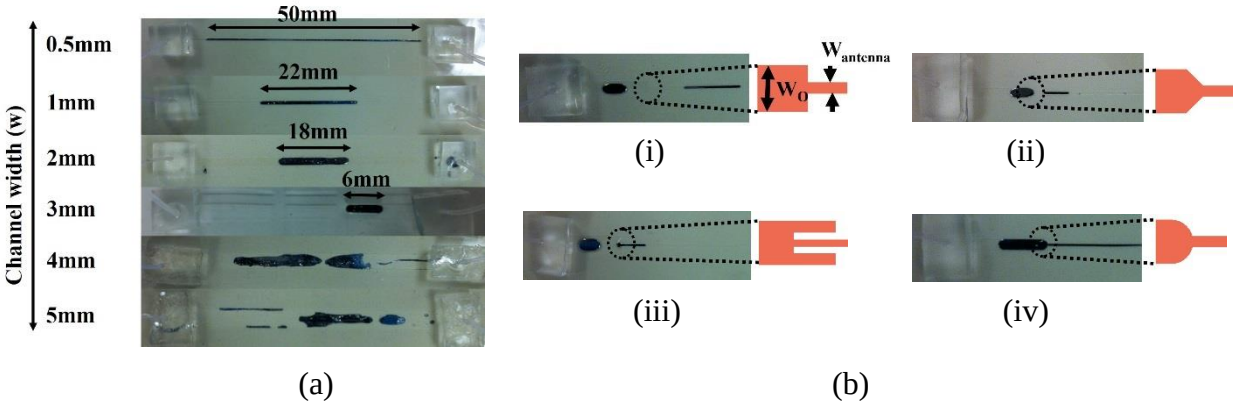

Figure 3.7: (a) Liquid metal flow in 250um high channels with varying widths; (b) Liquid metal flow characterization through different microfluidic junction layouts inter-connecting the 2mm (W_O) and 0.5mm ($W_{antenna}$) wide channels: (i) Straight transition; (ii) 30º tapered transition; (iii) Capillary action mimicking transition; (iv) Round transition.

it was not possible to form movable slugs as the liquid metal took a shape that does not cover the entire width of the channel. Table 3.1 presents the maximum slug lengths that could be realized inside the microfluidic channels. The maximum length was determined to be 50mm inside a 250µm high and 0.5mm wide microfluidic channel. Hence, 0.5mm wide and 250µm high channel shape was selected for implementing the radiating section of the monopole. This choice is attractive for realizing the minimum operational frequency and maximizing the frequency tuning range. On the other hand, a wider and shorter overlap area is advantageous for maximizing the capacitive coupling in the feed section. This approach alleviates undesired coupled line resonances

and minimizes the required liquid metal volume. From Table 3.1, it is observed that the widest channel that can accommodate the overall antenna volume (i.e. 0.5mm x 50mm x 250µm) is the 2mm wide channel (i.e. 2mm x 18mm x 250µm). Consequently, 2mm wide channel is selected for the feed section implementation. A second set of experiments was performed to identify a junction shape that will provide a reliable inter-transition of the liquid metal slug between the 0.5mm and 2mm wide channels. It is important that the liquid metal volume remains in the form of a continuous slug when it passes through the junction. However, the high surface tension of the liquid metal can prevent such a transition if the junction is not carefully designed. Figure. 3.7(b) depicts the junction shapes and corresponding behavior of the liquid metal slug. As can be seen from Figure. 3.7(b), among all the trials, the rounded junction shape was observed to provide a reliable operation without disrupting the continuous slug nature of the liquid metal. Therefore, this junction shape was selected for the antenna implementation.

3.4.2 Design

From the presented flow characterization studies, the maximum achievable length of the liquid metal slug was observed to be 50mm inside a 0.5mm wide and 250µm high microfluidic channel. Therefore, the antenna structure shown in Figure.3.5 was initially simulated with 50mm radiating length and 0.5mm width to determine the lowest resonance frequency (throughout the paper, Ansys HFSS v15 is used as the full-wave electromagnetic simulator). By using a direct electrical connection between the microstrip feed line and the monopole, the lowest resonance frequency was determined as f_{min}=1.2GHz. Hence, the minimum overlap area between the liquid metal and the microstrip feed line must be designed to exhibit an effective RF short ≥1.2GHz.

The minimum overlap area was determined based on the $|S_{21}|$ performance of two back-to-back liquid metal and microstrip line transitions as shown in Figure. 3.8(a). The microstrip feed

line had a width of W_{ms}=5mm to achieve Z_0=50Ω characteristic impedance. The width of overlap area was set to W_O=2mm based on the flow characterization studies. The overlap length L_O was gradually increased from 1mm to 10mm while the $|S_{21}|$ performances were observed over the 1GHz-5GHz band as shown in Figure 3.8(b). Specifically, for L_O=5mm, $|S_{21}|\geq$-0.62dB and implied ≤0.5dB insertion loss for single transition. Larger overlap lengths did not provide further significant reductions in insertion loss performance. Consequently, minimum overlap length was

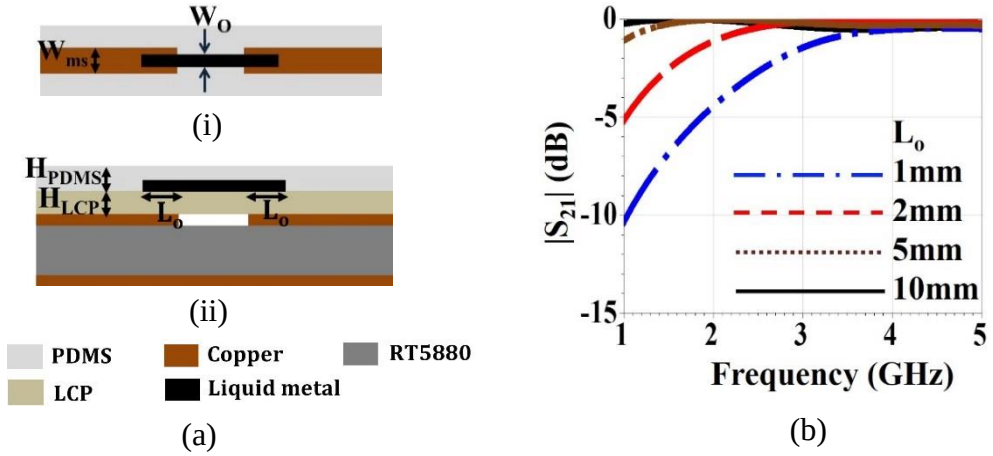

Figure 3.8: (a) Back-to-back feed model (i) Top view and (ii) Bottom view for minimum overlap length determination (W_{ms}=5mm, W_O=2mm, H_{LCP}=0.0254mm, H_{PDMS}=2mm); (b) S_{21} results for varying L_o.

selected as $L_{o(min)}$ =5mm.

Figure. 3.9 demonstrates the final dimensions of the frequency tunable liquid metal monopole antenna. The ground plane width was set to W_G=40mm. Large ground plane lengths L_G were found to distort the omnidirectional characteristic of the radiation pattern at frequencies higher than 4GHz [80]. The minimum ground plane length required was 17.5mm to be able to retract the entire volume of the liquid metal monopole inside the feed overlap channel. However, to accommodate an SMA connector, the ground plane length was enlarged to L_G=25mm. This length was found to preserve the omnidirectional nature of the radiation pattern up to 5GHz. Although the antenna can be tuned to higher frequencies, the maximum operational frequency was

therefore set to f_{max}= 5GHz. Consequently, the antenna was designed to be operating over a ~4:1 bandwidth from f_{min} =1.2GHz to f_{max}= 5GHz. This frequency range includes the amateur radio 23cm (1.24-1.3GHz), PCS (1.85-1.99GHz), AWS mobile phone downlink (2.11-2.155GHz), ISM (2.4-2.483GHz), amateur radio 9cm (3.3-3.5GHz), C-band communication satellite downlink (3.7-4GHz) and aeronautical radio navigation (4.2-4.2GHz) bands.

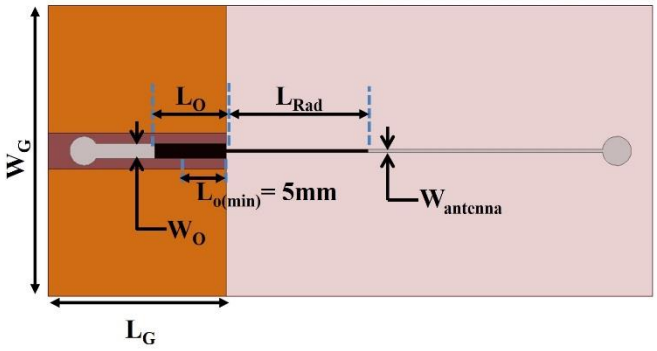

Figure 3.9: Layout with detailed dimensions of the final antenna.

To demonstrate the radiation performance, the antenna model was simulated by changing the radiating length L_{Rad} from 50mm to 10mm. The antenna provides continuous frequency tuning and representative radiation performances are specifically presented at 1.2GHz (LRad=50mm), 2.3GHz (L_{Rad}=25mm), 3.3GHz (L_{Rad}=20mm) and 4.8GHz (L_{Rad}=10mm). As shown in Figure. 3.10(a), the antenna operates with $|S_{11}|$<-10dB impedance matching performance throughout the entire frequency tuning range. The $|S_{11}|$<-10dB bandwidth varies between 8.33% and 16.9%. Figure. 3.10(b) depicts the realized peak gain as a function of tuning frequency along with the corresponding radiation efficiency. As seen, the radiation efficiency is relatively constant and larger than 84%. This implies that the variation in realized peak gain is associated with pattern

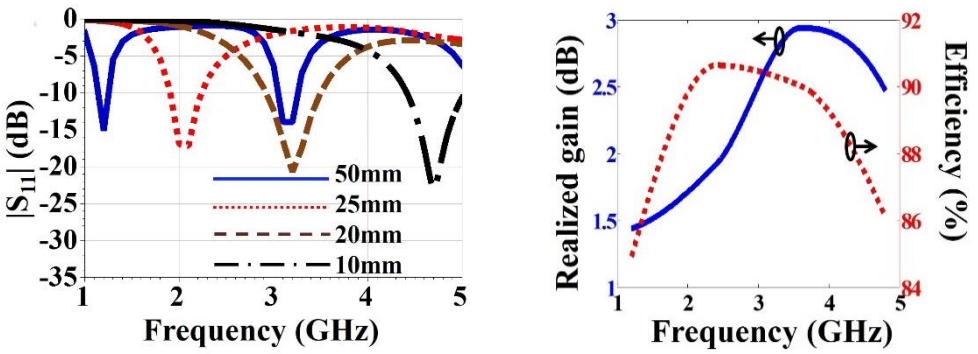

(a) (b)

Figure 3.10: (a) Simulated S11 of the wideband tunable antenna; (b) Plot of the realized gain of the antenna vs frequency.

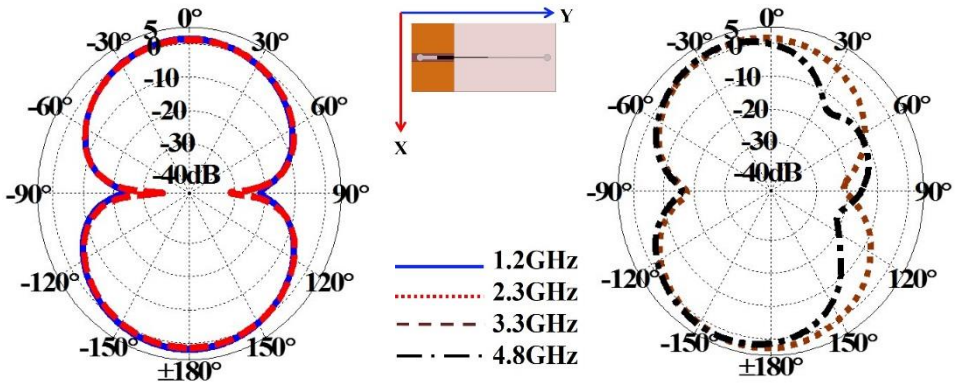

Figure 3.11: Radiation pattern of the antenna at different frequencies of the operating bandwidth along θ=90°

shaping due to the frequency dependent change in electrical size of the ground plane. Figure. 3.11 demonstrates the realized gain patterns in the θ=90° plane. Due to the designed ground plane size, the pattern maintains a shape closely resembling the conventional 8-Figureure across the frequency tuning range. In addition, the antenna performs with an omnidirectional radiation pattern in the θ=0° plane.

3.4.3 Fabrication

The microfluidic channel was fabricated using the soft lithography steps illustrated in Figure. 3.12(a). The mold of the channel was prepared using 250µm thick SU8 (SU8-2075) photoresist spun on top of a polished silicon wafer. The PDMS polymer (Sylgard 184 Elastomeric

Kit, Dow Corning) was mixed with its curing agent in 10:1 ratio, degassed in a vacuum box to remove trapped air bubbles, and poured on top of the SU8 mold. The PDMS volume was adjusted to provide 2mm thickness after curing. The curing was accelerated by baking it in a vacuum oven at 100°C for 45mins. The microfluidic connectors were formed as PDMS blocks and attached at the inlet and outlet of the channel using oxygen plasma bonding at 20W for 30s. After the PDMS layer carrying the channel was peeled off from the wafer, it was bonded with a 0.25mm thick LCP substrate by customizing a 3-Aminotriethoxysilane (APTES) based bonding process [81]. The

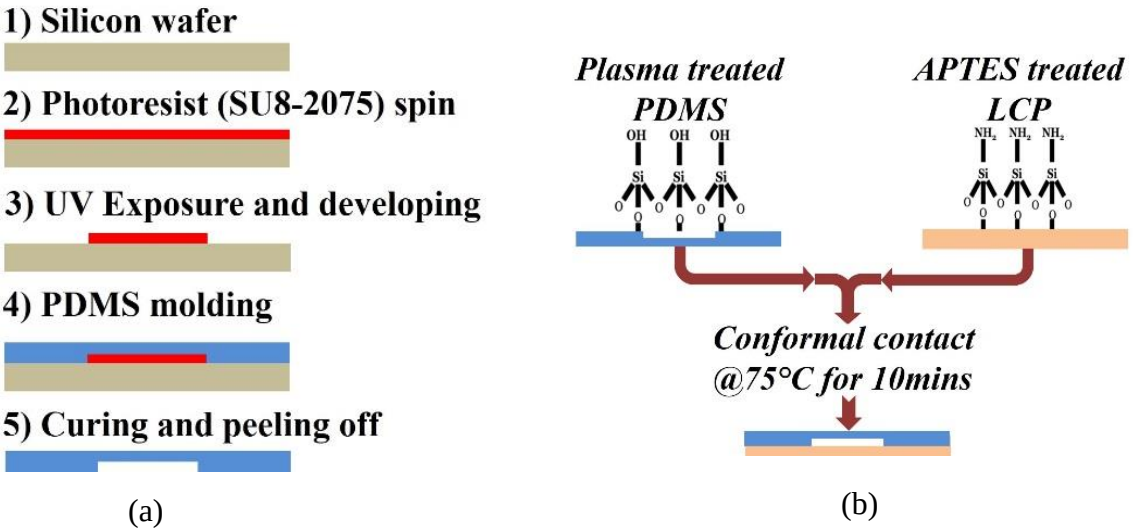

Figure 3.12: Fabrication procedure of the antenna, (a) Soft lithography procedure of fabricating the channels; (b) Procedure for irreversible bonding between PDMS and LCP.

process is demonstrated in Figure. 3.12(b). The LCP layer was immersed in a 5% volume solution of APTES in DI water heated to 80°C for 20mins. This results in the formation of the Si-NH2 groups on the surface of the LCP substrate. The PDMS layer was exposed to oxygen plasma at 20W for 30s to create Si-OH groups on the top surface. The two layers were then brought in contact with care to ensure that there were no trapped air bubbles in between. The layers bond instantaneously due to formation of Si-O-Si bonds. To further strengthen the bond, the bonded

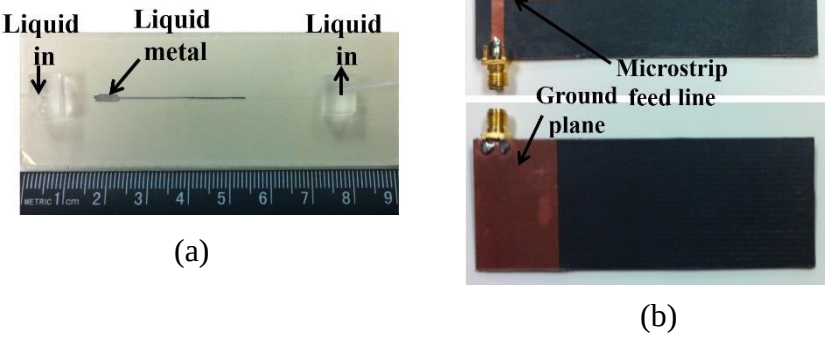

(a) (b)

Figure 3.13: Fabricated antenna; (a) Liquid metal enclosed in the PDMS channel, (b) RF feed board with 50Ω microstrip line.

layers was kept in a vacuum oven at 75°C for 10mins. The fabrication of the feed board was carried out with well-known PCB etching procedures. The feed line had a 90° bend to separate the SMA and microfluidic connectors from each other. The feed board and channel mold masks carried features to generate alignment holes. After preparing the holes, the channel and the feed board were aligned and glued together to form the final fabricated antenna assembly as shown in Figure. 3.13.

3.4.4 Experimental Verification

Figure 3.14(a) depicts the snapshots of the fabricated liquid metal monopole antenna as it is reconfigured to operate at various resonance frequencies. In the initial phase of the experiments, syringes were used to control the position of the liquid metal volume. The calculated mercury volume of 11.25mm3 was injected into the microchannel using the syringes. For each case shown in Figure 3.14(a), the radiating lengths were set to the values described in the simulation study (i.e. L_{Rad} = 50mm, 25mm, 20mm, 10mm) and the corresponding resonance frequencies were measured as shown in Figure 3.14(b). The measured response of the antenna shows a shift from the simulated value by 7.5% possibly due to the non-rectangular shape of the liquid metal and increase in insulator thickness due to the use of glue. The measured θ=90° plane realized gains are depicted

in Figure 3.14(c) and match to the radiation patterns expected from the simulation based studies presented in Figure. 3.11. Specifically, the measured peak realized gains are 1.38dB, 1.81dB, 2.23dB and 2.29dB at 1.29GHz, 2.48GHz, 3.53GHz and 5.17GHz, respectively. The second phase of the experiments were performed with commercially available piezo-actuator based micropumps obtained from Bartels Mikrotechnik GmbH [82] to automate the working of the liquid metal monopole antenna. The pumps had overall dimensions of $30\times15\times3.8mm^2$ with 2g weight and less than 200mW power consumption. Since the micropumps were unidirectional; two

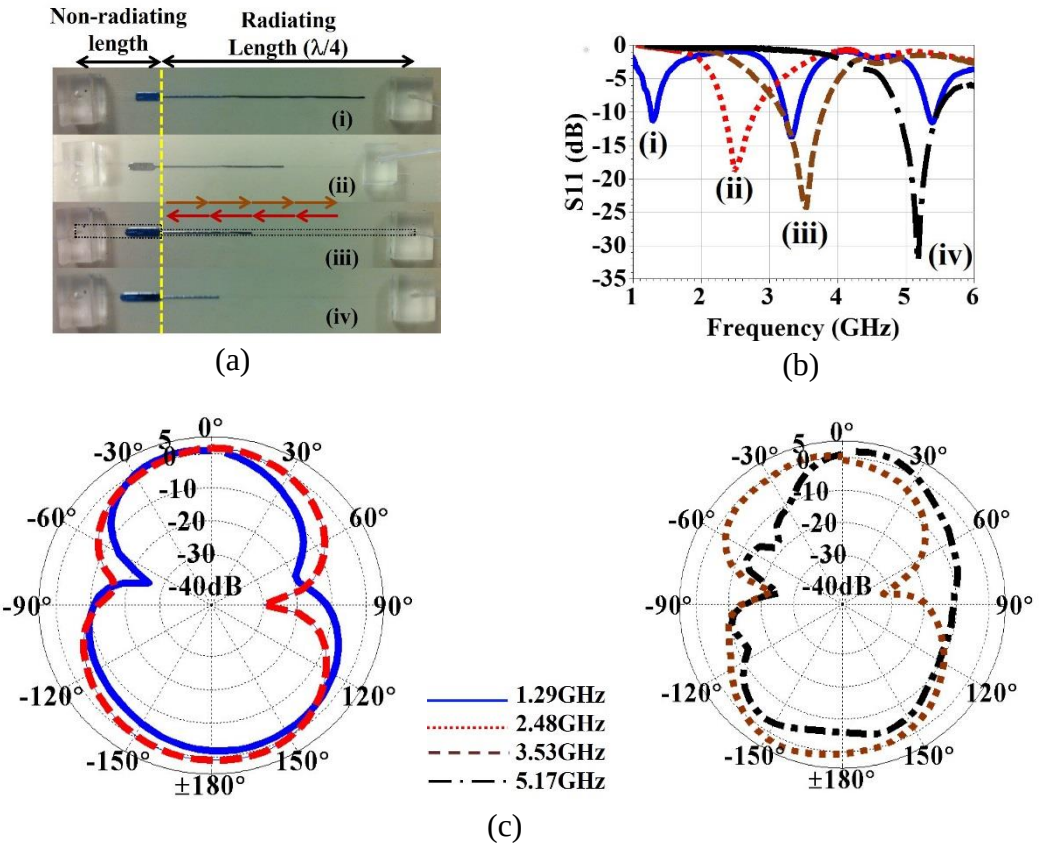

Figure 3.14: (a) Snapshots of the antenna being reconfigured from 1.29GHz to 5.17GHz; (b) Measured shift in resonance frequency as liquid metal is retracted over the ground plane; (c) measured radiation pattern along the θ=90° elevation plane for different operating frequencies of the antenna.

of them were connected in series to form the closed loop fluidic system with a bidirectional flow as shown in Figure. 3.15. To attain maximum flow rate (Q) inside the channel, flow

characterizations were performed to determine the amplitude and frequency of the low frequency (<15 Hz) alternating voltage signal used to drive the micropumps. The amplitude and frequency of the waveform control the pump membrane's displacement and vibration rate, respectively. The alternating voltage signal was generated by the mp-x control unit of the micropump manufacturer. Specifically, the sine wave signal exhibiting 250 peak to peak voltage (Vpp) and 10Hz frequency were observed to provide a maximum flow rate of Q=0.3 mm^3/sec. This is significantly lower than the maximum 120mm^3/s water flow rate reported in the manufacturer's data sheet. The drop in

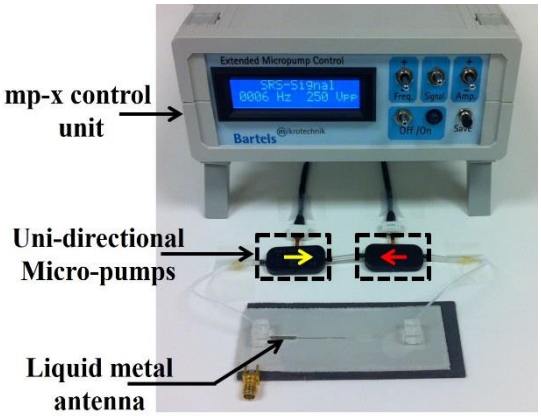

Figure 3.15: Set-up for liquid metal flow characterization using micro-pumps.

flow rate is partially attributed to the higher viscosity of the Teflon solution (>4.1cP) as compared to that of the water (0.894cP). In addition, the series connection of two pumps with opposing flow direction contributes to the reduced level of the flow rate by increasing the backpressure. Reconfiguration speed (t) is calculated as t=V/Q, where V denotes the volume of the liquid to be displaced. With the characterized maximum flow rate Q=0.3mm^3/s, microfluidic channel height (H=0.25mm) and antenna dimensions (L_{Rad}=50mm at 1.29GHz, and L_{Rad}=10mm at 5.17GHz, Wantenna=0.5mm), the total time needed to tune the antenna across to entire frequency range can be calculated as t=16.66s. This matches well with the 16s reconfiguration time measured from the manufactured antenna assembly. To decrease the reconfiguration time, bidirectional micropumps

capable of providing higher flow rates for viscous materials can be utilized (e.g. external gear and peristaltic pumps).

In the third phase of the experiment, the possibility of implementing the antenna with non-toxic liquid metal Galinstan [83] was considered. Since Galinstan is an eutectic alloy of Gallium, Indium and Tin, it oxidizes rapidly and requires advanced packaging. To avoid the oxidization related sticking, the realization of the fabricated antenna from Galinstan was carried out inside an

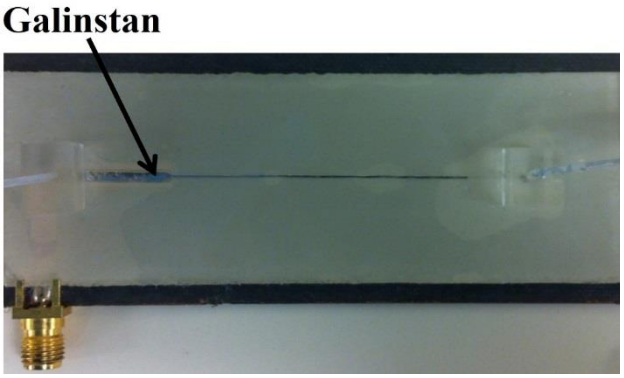

Figure 3.16: Implementation of the antenna using Galinstan.

Inert Lab Glove Box (Innovative Technology Inc.) that maintained the oxygen and moisture content to <1ppm. The antenna was observed to perform reliably inside the glove box (Figure 3.16). The antenna fails to operate once taken outside of the glove box as a result of Galinstan oxidization and sticking to the channel walls. This is due to the porous nature of the PDMS. Nevertheless, the experiment demonstrates that hermetically sealed implementations resorting to hard substrates (e.g. glass) could allow to realize the proposed antenna with non-toxic Galinstan for long-term operation.

Recent publications have investigated techniques to address this problem and potentially replace pumps with alternative actuation techniques. In reference [84], the technique of continuous electrowetting to implement a reconfigurable slot antenna was introduced. Reference [85] applies

a similar approach to develop a tunable amplifier using reconfigurable liquid metal based double-stub tuners. Different from electrowetting on dielectric, electrocapillary actuation has been shown as a low power means to tune a liquid metal bandpass filter [86]. In [61] and [66], detailed discussions on practical implementation of liquid metal antennas with non-toxic Galinstan for long-term operation are provided. The non-toxic and high-boiling point of Galinstan make it an ideal candidate for implementing reconfigurable liquid metal components and circuits at room temperature.

3.5 Liquid Metal Monopole Array

The antenna shows wideband tunability that is not achieved using conventional reconfiguration techniques. To develop a stand-alone system though, it needs the incorporation of micro-pumps as discussed earlier. These pumps offer the advantage of introducing automation but at the same time their usage to run a single tunable antenna is not completely justified. The use of this microfluidic reconfiguration technique can be extended to control multiple antennas. Several of the liquid metal antennas arranged in the form of an array could all be connected and controlled using a single bi-directional pump (or two unidirectional pumps). The antennas can then be reconfigured similar to the single antenna element thereby resembling a wideband frequency tunable antenna array. The array provides the advantage of high gain as compared to a single element. This concept is demonstrated by developing a 4×1 frequency tunable monopole array discussed as follows.

3.5.1 Design

Four of the single liquid metal monopole antennas are linearly arranged along y-axis and interconnected to each other. The inlet and outlet of the array is connected to a single bi-directional pump unit (comprising of two unidirectional pumps). The concept figure of the 4×1 antenna array

is shown in Figure 3.17. The array represents a broadside antenna array with all the elements of the array fed in phase (β=0°). The distance between each array element (d) (Figure. 3.18(a)) had to be chosen in a way that it does not affect the pattern at the high frequency end of the bandwidth or the matching at the low frequency end.

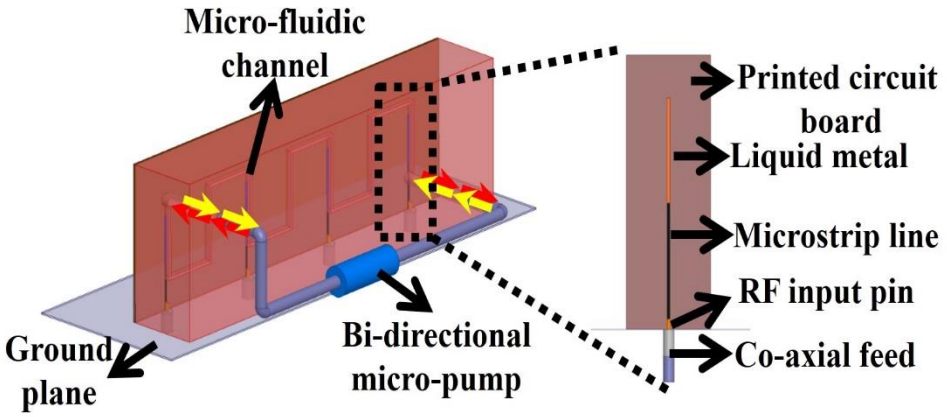

Figure 3.17: Liquid metal monopole broadside array implemented using a single bidirectional unit

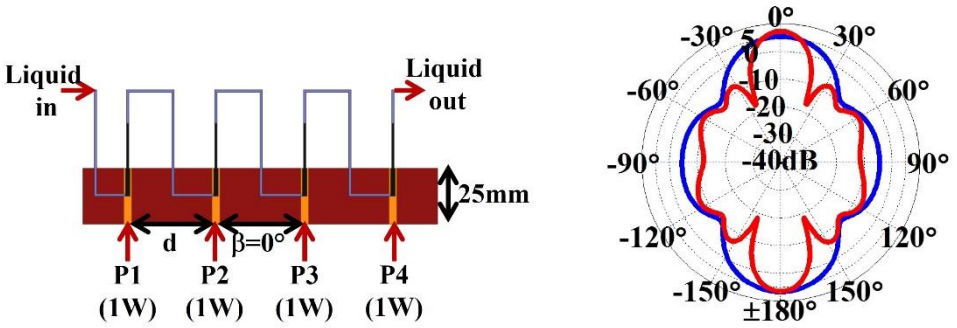

(a) (b)

Figure 3.18: (a) Layout of the broadside array; (b) Radiation pattern of the tunable array at 2.5 GHz and 5 GHz

With the higher end of the operating bandwidth set at 5GHz, the inter element spacing (d) had to be set <60mm (λ_0@5Ghz) to prevent the appearance of grating lobes. Different values of d starting from 10mm were investigated by HFSS simulations and the corresponding coupling (S_{21}) between the array elements was observed. With increase in d, the coupling decreases as well as the lower frequency at which the array can operate (with coupling of less than 10dB). Taking the

above stated points into consideration along with the fabrication capabilities, the inter element spacing was set at d=40mm. The radiation pattern of the array along the θ=90° cut is shown in Figure 3.18(c). The radiation patterns shown for the array operating at 2.5GHz and 5GHz demonstrate the broadside pattern.

3.5.2 Experimental Verification

In order to automate the working of the antenna micro-pumps were incorporated as mentioned earlier. The pumps obtained from Bartels Mikrotechnik were characterized using an mp-x control unit. This unit is capable of changing the frequency and amplitude of the signal being supplied to the micro-pumps but only controls one pump at a time. Furthermore, the unit is bulky and not ideally suited for portable applications. It does serve the purpose of characterizing the signal specifications (100Hz, 250Vpp) needed to drive the pumps. Taking the specifications into consideration a microcontroller (Arduino Uno) was used in conjunction with the driving circuit (mp6-OEM controller) to develop the bi-directional pumping unit. The driving circuit takes two inputs in the form of AMPLITUDE and CLOCK to define the output signal being delivered to the pump. These two inputs can be defined using the microcontroller. Two push button switches were incorporated to sense which pump needs to be activated. By pressing and holding down these two switches accordingly the antenna array can be reconfigured to the desired resonant frequency. Figure 3.19 shows the final pumping control unit developed along with the fabricated array.

Similar to the operation of a single liquid metal antenna the array is made to reconfigure by pumping the liquid metal using the two unidirectional pumps. Prior to the array operation, an initialization step is involved. This involves inserting the same volume of liquid metal in each antenna element using syringes. The corresponding inlet and outlet of each antenna are then connected to form a closed system with the inlet and outlet of the outside array elements connected

to each other through the pumping unit. As the liquid inside the channels is moved using the pumps the operating frequency of the array shifts. Figure 3.20(a) shows the array being reconfigured to the lowest operating frequency of 2.5GHz. To make the array tune to the highest operating frequency of 5GHz the left pump is switched on which pushes the Teflon solution and the liquid

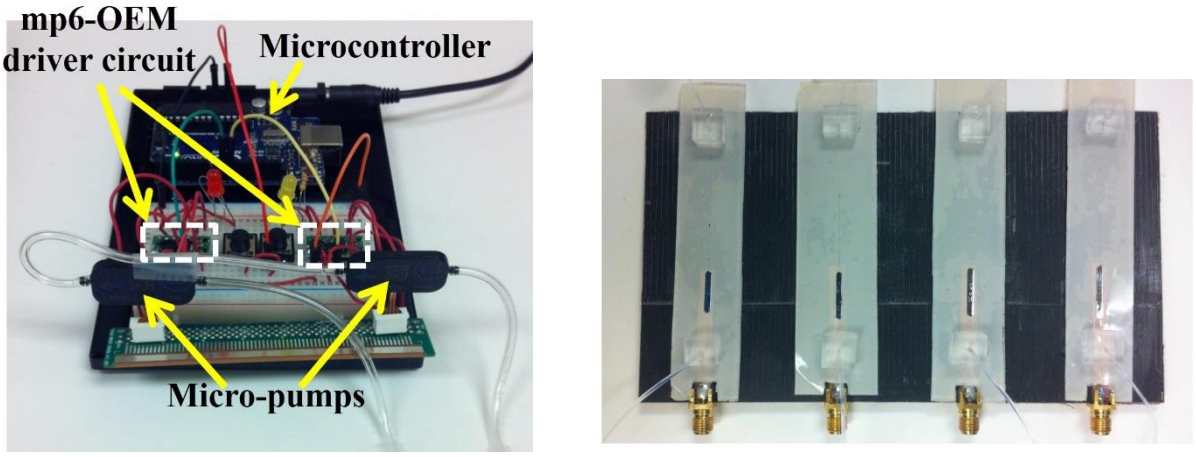

(a) (b)

Figure 3.19: (a) Portable pumping unit for the antenna array; b) Initialized antenna array before reconfiguration.

metal downwards (Figure 3.20(b)). The measured gain is 6.2dB @ 2.5GHz and 8.06 dB @ 5GHz. The tuning speed of the array was calculated by measuring the time taken to tune from 2.5GHz to 5GHz. The measured time was 20s which represents a tuning speed of 125MHz/s for the 2.5GHz to 5GHz operating bandwidth.

3.6 Conclusion

In this chapter microfluidically reconfigured wideband frequency tunable liquid metal monopoles were presented. The antenna relied on continuous moving of the liquid metal volume over the capacitively coupled microstrip line feed network with a micropump unit. The capacitive coupling at the feed point was realized by bonding microfluidic channel molds prepared in PDMS with thin LCP substrate. The antenna implemented using meandered couple line approach

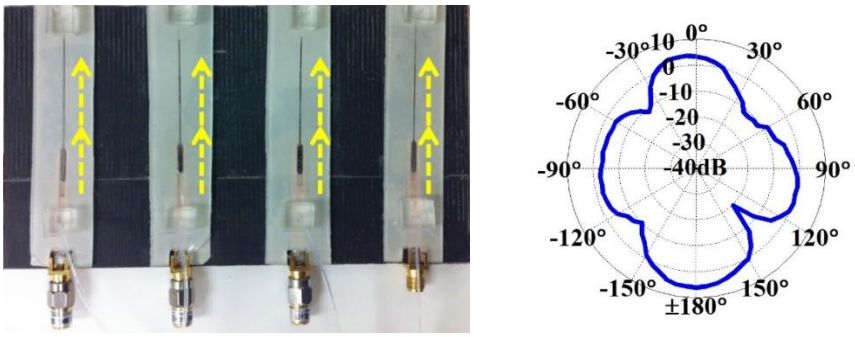

(a)

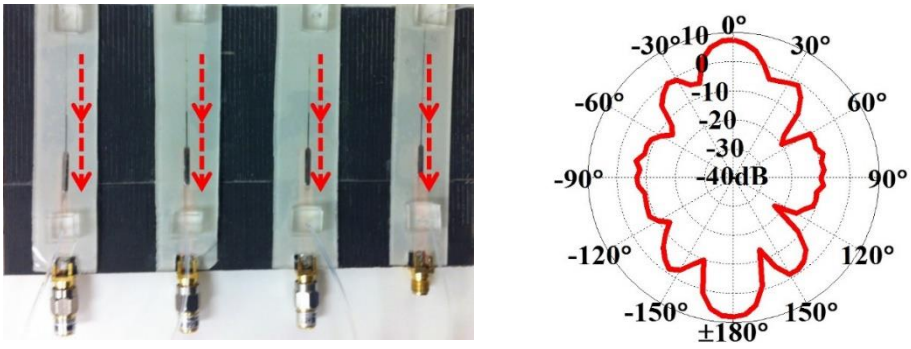

(b)

Figure 3.20: Snapshots of the array being reconfigured and the corresponding measured radiation pattern at; (a) Low frequency (2.5GHz), (b) High frequency (5GHz) of the operating bandwidth

demonstrated a tuning range of 1:2.9. This was improved by resorting to a tapered feed line approach. The antenna was measured to operate from 1.29GHz to 5.17GHz, providing ~4:1 frequency tuning range. To ensure reliability, the antenna design was carried out by resorting to flow characterization studies performed over different microfluidic channel shapes. To demonstrate the applicability of the presented monopole in antenna arrays, a 4×1 frequency tunable array was developed. The array was measured to operate from 2.5GHz to 5GHz and operated with a single bidirectional micropump unit by resorting to interconnected microfluidic channels. In order the address the issue with rapid oxidation of Galinstan a new approach for implementing the monopole antenna is discussed in the next chapter.

CHAPTER 4: MICROFLUIDICALLY CONTROLLED FREQUENCY TUNABLE ANTENNA FOR HIGH POWER APPLICATIONS

4.1 Note to Reader

Portions of this chapter have been previously published in [88,93], and have been reproduced with permission from IEEE. Permission is included in Appendix A.

4.2 Introduction

Microfluidic based reconfigurability has been recently proposed as an alternative technique to implement novel microwave components [59-77] due to its promise for achieving low cost, high linearity, high power handling, and wideband frequency tunability. Several frequency tunable antennas demonstrating these advantages have been recently introduced. For example, [87] has utilized liquid metal driven by continuous electro-wetting to reconfigure the electrical length of a slot antenna to achieve frequency tunability from 2.52GHz to 2.88GHz in discrete steps. Reference [59] has demonstrated a patch antenna that can be switched between GPS and ISM bands by using pressure driven liquid metal. Liquid metal has also been used as a reactive load to tune both bands of a dual band slot antenna in two discrete steps [63]. Instead of employing liquid metals as the tuning element, [65] has demonstrated a slot antenna that is frequency reconfigured over 3.3GHz-4.2GHz for first resonance and 5.2GHz-8GHz for second resonance using fluids of different permittivity values.

To achieve continuous and significantly increased frequency tuning range, the liquid metal monopole antenna realized in Chapter 3 was implemented with a capacitively coupled feed

mechanism. This utilized a very thin (25.4um) liquid crystal polymer (LCP) layer to seal the microfluidic channels prepared in PDMS [78]. This antenna operated from 1.2GHz to 4.8GHz with a tuning ratio of ~4:1. In this chapter, we improve the reliability of this monopole antenna by replacing the liquid metal with a metalized plate that can be reconfigured within the microfluidic channel [88] (see Figure 4.1). In addition, the microfluidic channel prepared in PDMS is chemically bonded to the feed board substrate RO4003C by spinning a 12µm thick layer of BCB insulator in contrast to the manual clamping used in our previous work. The higher conductivity of metalized plate, lower loss factor of BCB, and the higher thermal conductivity of the RO4003C substrate increases the power handling capability of this monopole antenna over the previous implementation. To show this, the power handling capability of these monopole antennas are studied for the first time through multiphysics simulations and experiments. Specifically, the presented monopole operates over a wide frequency tuning range from 1.7GHz to 3.5GHz (~2:1) with a measured realized gain >2.4dB. It exhibits 200% more power handling capability as compared to the prior implementation.

4.3 Microfluidically Controlled Monopole Antenna

4.3.1 Antenna Topology

The layout and the substrate stack-up of the reconfigurable monopole antenna is shown in Figure 4.1. The antenna consists of a 0.51mm thick metallized plate (RO4003C, ε_r = 3.38, tanδ= 0.0027 with a metallization thickness of 0.01mm) enclosed within a 0.75mm thick microfluidic channel. The microfluidic channel is fabricated in a 2mm thick Polydimethydisiloxane (PDMS, ε_r = 2.8, tanδ= 0.02) layer using soft lithography technique. A low loss ultra-thin dielectric layer of Benzo-cyclobutene (BCB, ε_r = 2.65, tanδ= 0.0005) is spun on top of the 1.52mm thick RO4003C feed board that carries the 50Ω microstrip line. The microchannel containing the metallized plate

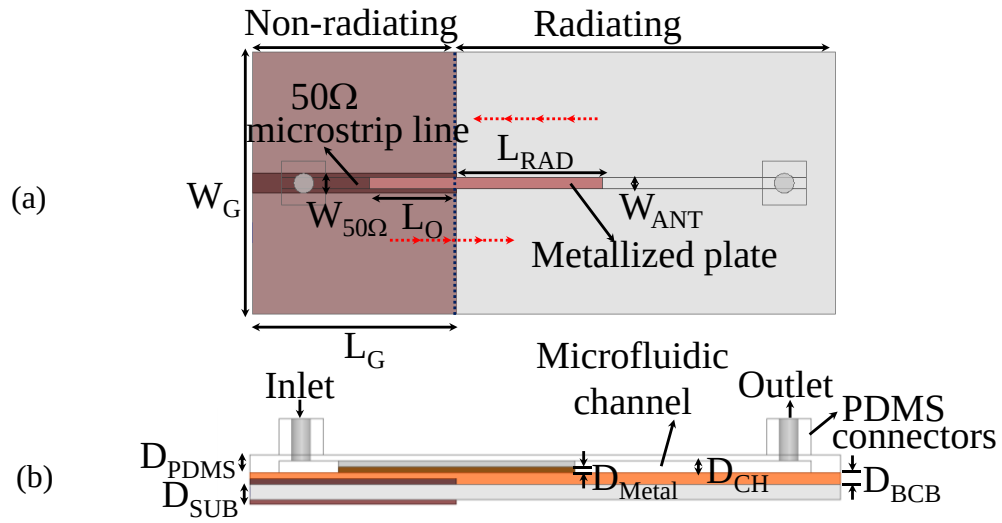

Figure 4.1: (a) Layout of microfluidically controlled monopole antenna; (b) Cross section view of the antenna.

is bonded to the BCB layer and then filled up with a low loss dielectric solution (FC-40, ε_r=1.9, tanδ=0.0005) using external micro-pumps. The pressure exerted by the pumps on the FC-40 solution is used to push the metallized plate inside the microchannel.

4.3.2 Antenna Design

Tunability of the antenna is achieved by partially retracting the metallized plate over the ground plane as shown in Figure 4.2(a). The lowest operation frequency of the antenna was selected as 1.5GHz. The minimum overlap area needed to exhibit an RF short between the feed line and the metalized plate at this frequency was determined by observing the $|S_{21}|$ response of two back to back metallized plate to microstrip line transitions as depicted in Figure 4.3(a) and (b). The overlap area between the metallized plate and the microstrip line is governed by the W_{ANT} and L_O values [89]. Increasing W_{ANT} lowers the insertion loss as seen in Figure 4.3(c). However, this also increases the fractional bandwidth of the antenna. To keep the fractional bandwidth less than 20%, W_{ANT} was selected as 2mm. Similarly, increasing L_O lowers the insertion loss as shown in Figure 4.3(d). However, choosing a small value for L_O is important since retracting the antenna

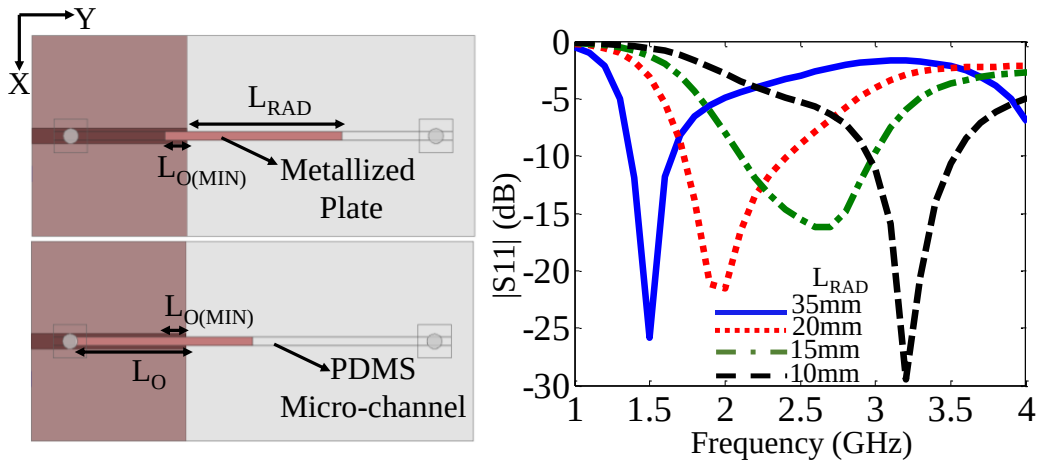

(a) (b)

Figure 4.2: (a) Frequency tuning principle of the metallized plate monopole antenna; (b) Corresponding simulated $|S_{11}|$ response of the antenna.

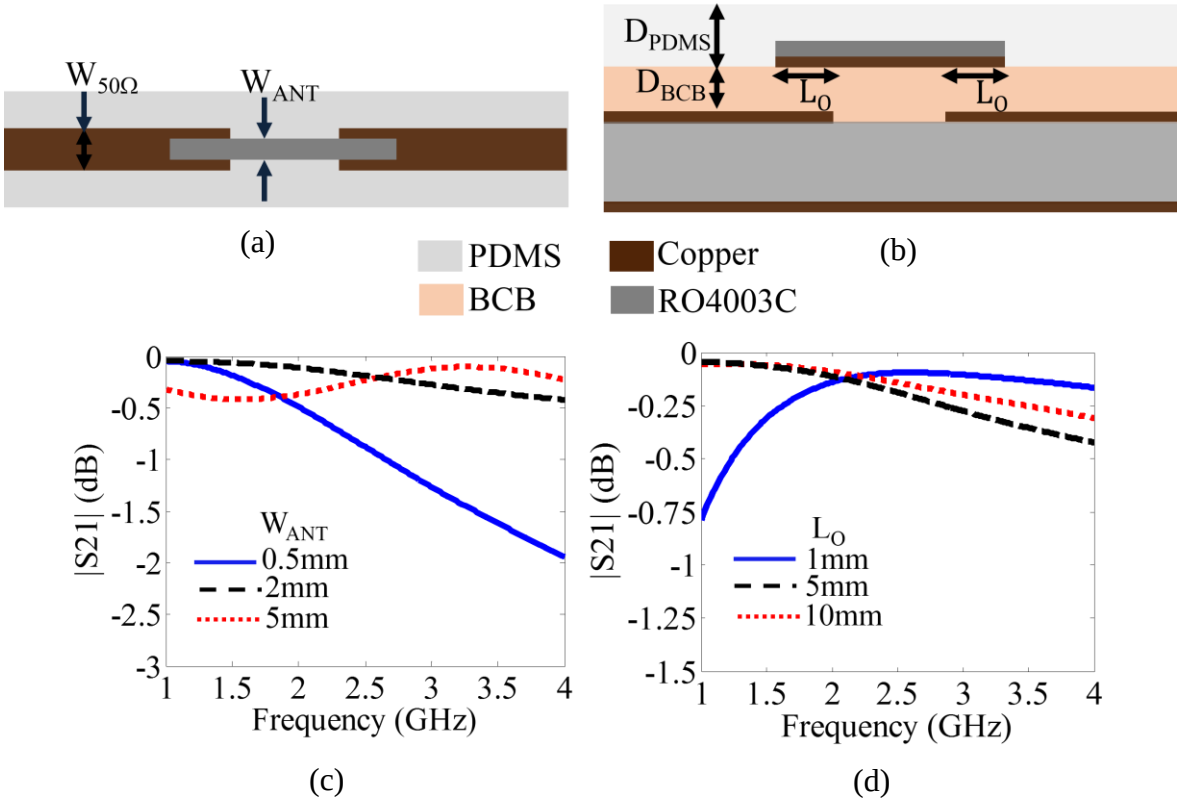

(c) (d)

Figure 4.3: Back to back non-contact feed model of the monopole; (a) Top view; (b) Side view; Corresponding simulated $|S_{21}|$ response of the feed model with change in; (c) Width of the antenna (W_{ANT}); (d) Overlap length (L_O).

over the feed line creates a coupled line resonance that eventually determines the highest operation frequency. The minimum value of the overlap length ($L_{O(MIN)}$) was set to 5mm. With this choice, the plate was retracted to tune the antenna to higher frequencies and it was observed that the coupled line resonance did not appear up to 3.3GHz. Hence, the operation band of the antenna was from 1.5GHz to 3.3GHz with a 2.2:1 tuning ratio. Figure 4.2(b) demonstrates the simulated $|S_{11}|$ performances as the antenna is tuned to different frequencies by retracting the metalized plate. The remaining dimensions of the antenna are shown in Table 4.1.

Table 4.1 Dimensions (mm) of the antenna

W_G	45	D_{PDMS}	2
L_G	35	D_{BCB}	0.012
$W_{50\Omega}$	3.5	D_{SUB}	1.52
W_{ANT}	2	D_{CH}	0.75

4.4 Experimental Verification

4.4.1 Fabrication

The microfluidic channel was fabricated using the soft lithography technique [90]. The feed board carrying the microstrip line and the ground plane was prepared using traditional photolithography and copper etching procedure. BCB was used for bonding the two substrates together using a customized recipe used for bonding liquid crystal polymer (LCP) and PDMS. The thickness of the metallized plate was selected from readily available RO4003C substrates (0.51mm). Experiments were conducted by fabricating microchannels of different height to determine the height needed for reliable movement of the metallized plate inside the microchannel. Experimental results yielded that for a metallized plate thickness of 0.51mm, microchannel thickness of 0.75mm allowed reliable movement of the plate. Figure 4.4 shows the final fabricated antenna prototype.

Commercially available mp-6 piezoelectric micro-pumps (Bartles Mikrotechnik) were connected to the fabricated antenna for driving the dielectric liquid FC-40 inside the microchannel. Two unidirectional pumps were used to implement a bidirectional pumping system using y-connectors. The pumps were controlled using an on-chip driver circuit and two push button switches as shown in Figure 4.4. The driver was configured to supply a sine wave (235VPP, 100Hz) signal. Based on the supplied data sheet, these values provide a maximum flow rate for water. The time taken to move the metallized plate to cover the entire tuning range was measured to be 1.15s implying 1565MHz/s tuning speed.

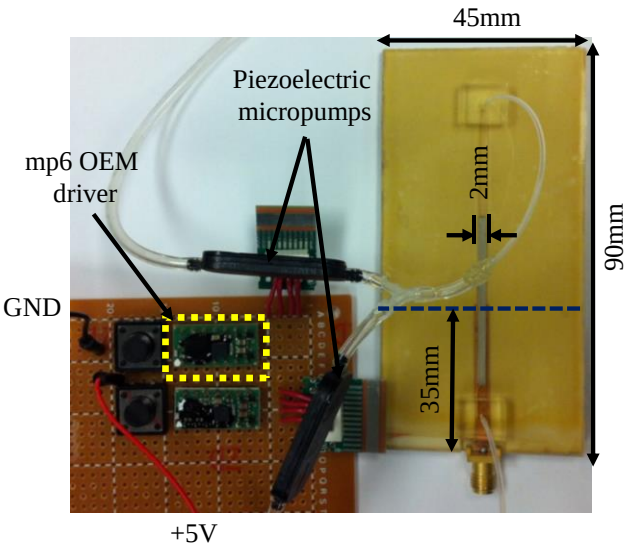

Figure 4.4: Fabricated antenna.

4.4.2 Antenna Performance

Figure 4.5(a) shows snapshots of the monopole as it is being reconfigured. The corresponding measured reflection coefficient for each state is shown in Figure 4.5(b). The measured performance of the antenna demonstrates the 2:1 tunability from 1.7GHz to 3.5GHz with 0.2GHz shift towards higher frequency as compared to simulated performance. Since BCB thickness was comparable to the conductor thickness, the top surface of the BCB layer over the microstrip line was not uniformly planar as was also observed in [91]. The plate location along the

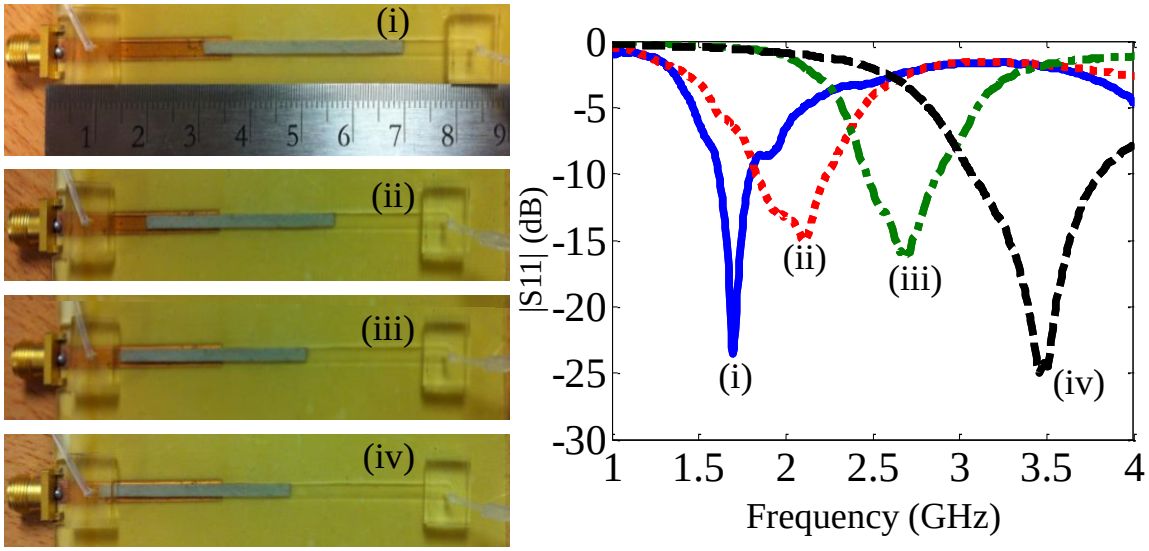

Figure 4.5: (a) Snapshots of the different configurations of the antenna; (b) Corresponding $|S_{11}|$ response

depth of the channel is another potential reason for this frequency shift since the plate can be surrounded with dielectric liquid instead of being rest at the bottom. The radiation pattern was measured at different reconfiguration states along the θ=90° plane. Figure 4.6(a) shows the measured and simulated normalized radiation patterns at 2GHz. The measured and simulated realized gains are also plotted over the frequency range in Figure 4.6(b) with solid dots denoting the data points taken at 1.6GHz, 1.75GHz, 2GHz, 2.6GHz and 3.3GHz. As seen, the measured data is in agreement with the simulations with less than 0.2 dB gain difference. The radiation efficiency was measured with modified Wheeler cap method and was found to be in well agreement with simulations by being 92.4%, 88.9%, and 87.4% at 2GHz, 2.6GHz, and 3GHz, respectively. In experiments, it was observed that switching the pumps on/off instantaneously started/stopped the plate movement without any overshoot. However, a larger number of experiments should be carried out in a microprocessor controlled setting to verify the accuracy and repeatability limits of this observation.

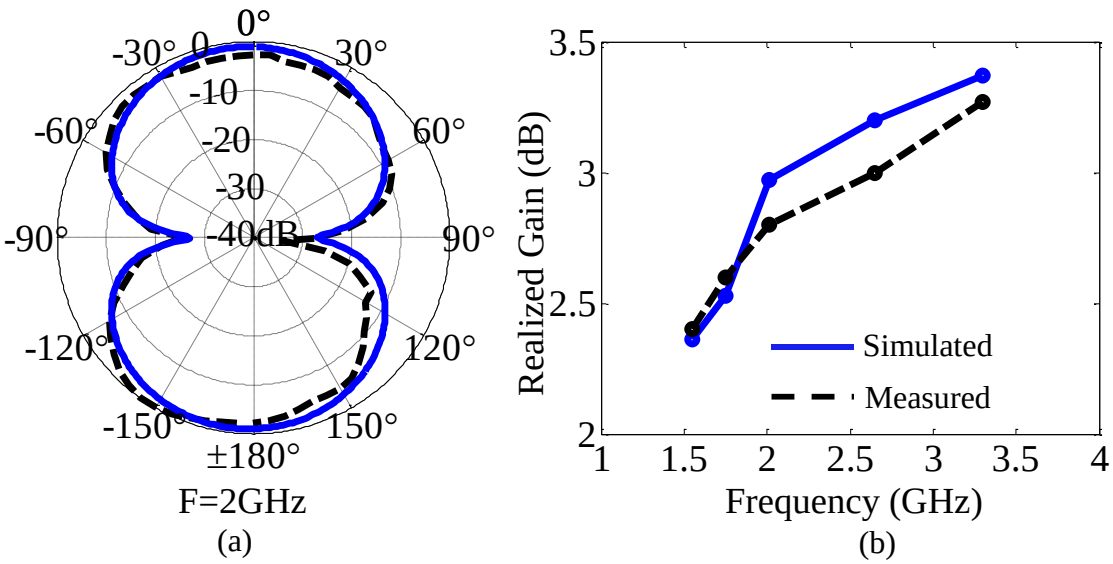

Figure 4.6: (a) Normalized radiation pattern of the antenna at 2GHz; (b) Plot showing simulated and measured realized gain at different frequency states (circle denotes the data points).

4.5 Power Handling

Microfluidically controlled antennas have been stated to have higher power handling capabilities due to their linear reconfiguration nature [92]. However, to the best of our knowledge, no work has been presented to demonstrate their power handling capability. To assess the power handling capabilities of the monopole antenna through simulations, the full wave electromagnetic model of the antenna in Ansys HFSS was imported into Ansys Workbench to perform steady state thermal simulations under different RF power excitations. In order to test the high power handling capability of the metallized plate monopole, the antenna was simulated in ANSYS Workbench Platform. The antenna substrate stack-up defined in Figure 4.1 was simulated in ANSYS HFSS at the resonant frequencies of 1.5GHz, 2GHz, 2.5GHz, 3GHz and 3.5GHz. This was done to cover the entire frequency of operation of the monopole (1.5GHz-3.5GHz). The simulated structure was then imported into the ANSYS Workbench Platform. This operation imports the geometry and the associated electro-magnetic field distribution over the antenna. The EM solution of the antenna

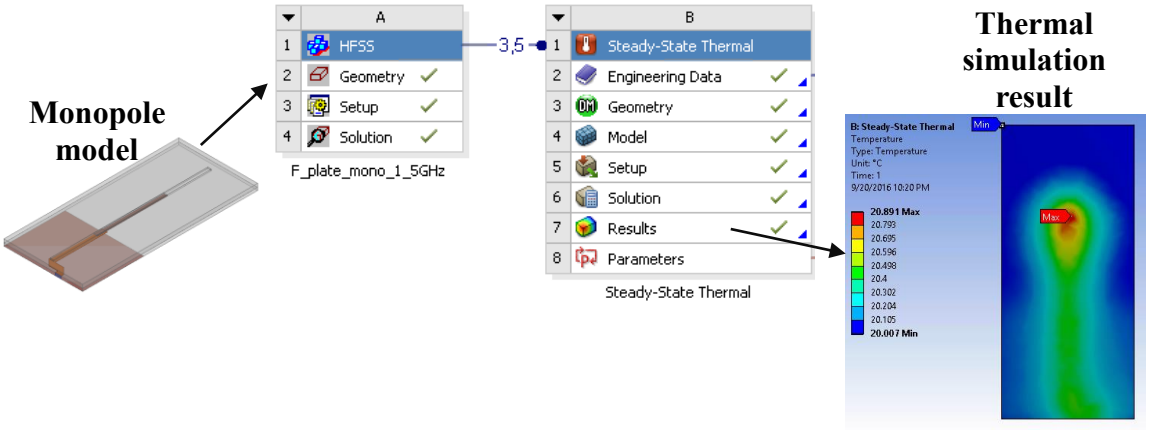

Figure 4.7: Simulation set-up in ANSYS Workbench for evaluating power handling capability of the monopole antenna.

model is then coupled to a steady state thermal block which then computes the thermal distribution over the antenna for a specified RF input power. The simulation set-up is shown in Figure 4.7.

The steady state simulation block in the Workbench platform has several key inputs which have to be defined appropriately for achieving accurate simulation accuracy. The *Engineering Data* state holds the properties of the materials assigned to the substrate stack-up of the antenna. The key property required for the thermal simulation is the isotropic thermal conductivity of the material. Table 4.2 shows the values for thermal conductivity that were used for the simulation. The *Geometry* state defines the structure on which the thermal simulation is being performed. In this case it was same as the geometry used for the full wave electromagnetic simulations. In the Model state we define the parts of the antenna geometry that will be used for the thermal simulation. Figure 4.8 shows the set-up used, a check mark next to a substrate component means it's being used for the thermal simulation while the parts that are not are marked by a cross. In this simulation set-up all the geometries imported from the HFSS simulation were used except for the radiation box and the rectangle used to define the electrical excitation port. In the *Setup* state is where the settings for the thermal simulation are defined. The settings include state initial

Table 4.2 Thermal conductivity of antenna materials

Material	Thermal conductivity (W/ m ºC)
RO4003C	0.71
BCB	0.29
FC-40	0.065
PDMS	0.15
RT5880	0.2
Copper	401

temperature, convection, load - heat flux or heat generation. The initial temperature was set to the room temperature where the measurement was performed (22ºC). The convection input defines the thermal boundary condition and it was assigned to all the antenna surfaces that are exposed to the surrounding air. The load input was imported from the electromagnetic simulation results. All the metals present in the structure were assigned as Heat Flux and all the dielectric were assigned as Heat Generation. Figure 4.9 shows the simulation settings described above. The results can be observed under the *Solution* state after the simulator completes the simulation. In the present case

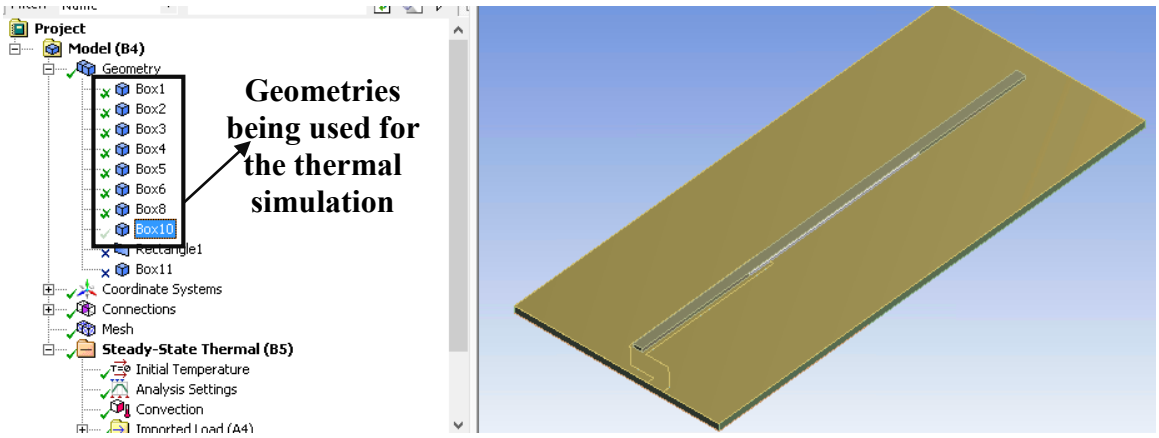

Figure 4.8: Settings showing antenna geometries used in the thermal simulation

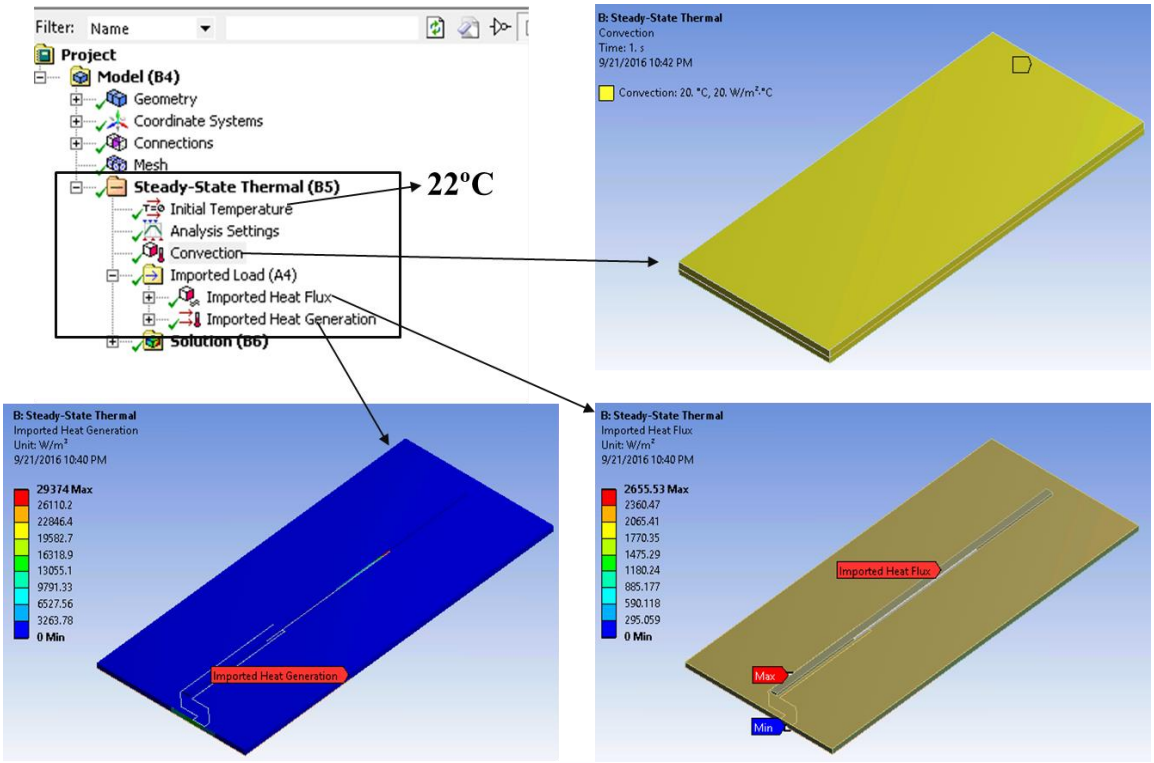

Figure 4.9: Steady-state thermal settings

we observed the surface temperature distribution over the antenna model. This exercise was important as it helped in developing a simulation model that closely matched the measurement results. The simulation model could then be trusted to predict the thermal behavior of the antenna at higher RF power levels than that was available in our measurement lab. It also helps in predicting the failure point of the antenna i.e., when the surface temperature is so high that the fluid (FC-77) used to re-configure the antenna is compromised.

The simulated results were then compared with measurements taken with the set-up shown in Figure 4.10(a). Figure 4.10(b) depicts the frequency dependent measured (dots) and simulated (solid lines) maximum temperature values observed on the antenna surface when the antenna was excited with 5W, 10W, and 15W RF power levels. Figure 4.11 also shows a comparison of the simulated and measured thermal profiles at 2GHz, 2.5GHz and 3GHz when the antenna was

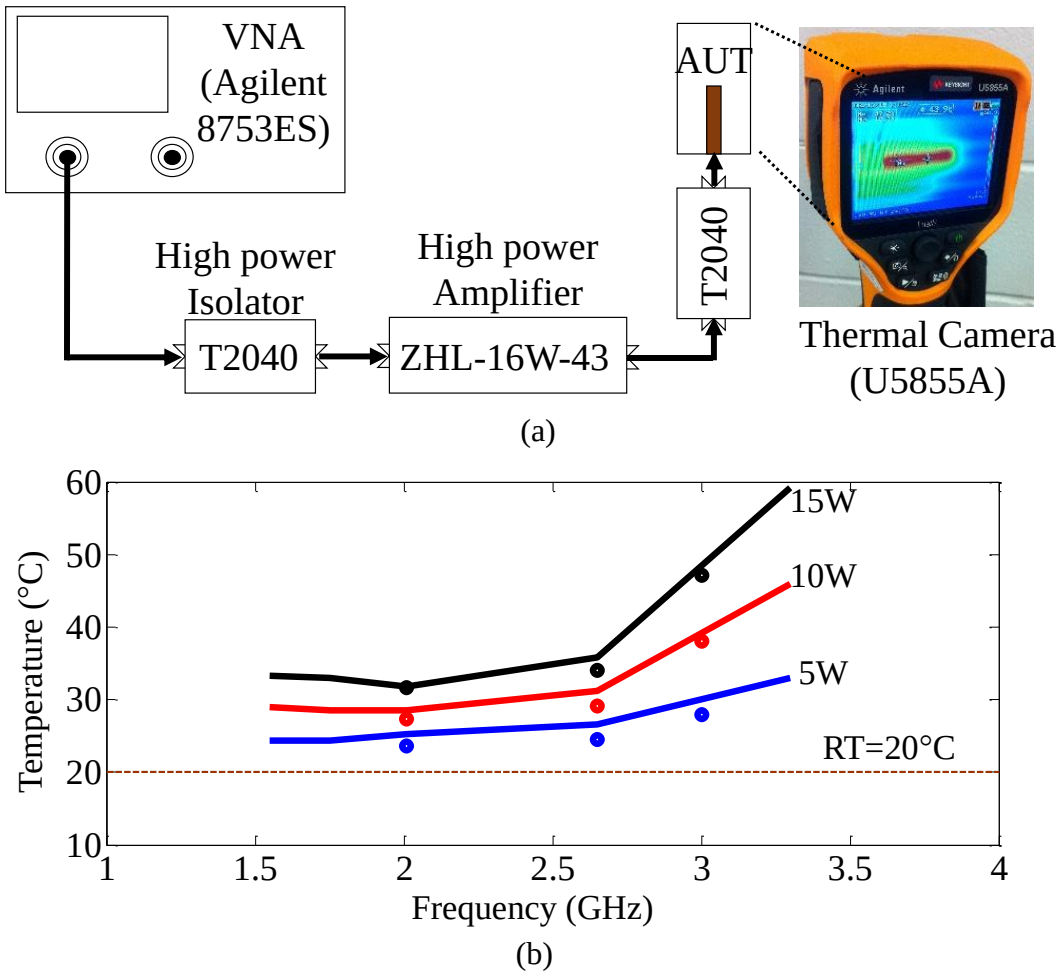

Figure 4.10: (a) Experimental set-up for measuring the thermal profile of the antenna under high RF power excitation; (b) Variation of the maximum temperature values on the antenna surface with change in the resonating frequency for different RF input power

excited with 15W RF input power. Specifically, after exciting with the RF power, the antenna temperature reached to a steady state in 35 min, 30 min, and 20 min at 2GHz, 2.5GHz, and 3GHz, respectively. The thermal images and reported temperatures were recorded at 45th min for all cases. The measured surface temperature matched with an accuracy of +/- 2°C to those obtained from simulations; hence, providing confidence for the simulation accuracy. The thermal profiles showed that the highest temperature is achieved at the feed section of the antenna. The temperature of the antenna increases at higher frequencies. This is expected since the simulated efficiency of the antenna drops with frequency increase (from 95% to 90%). Specifically, under 15W RF power

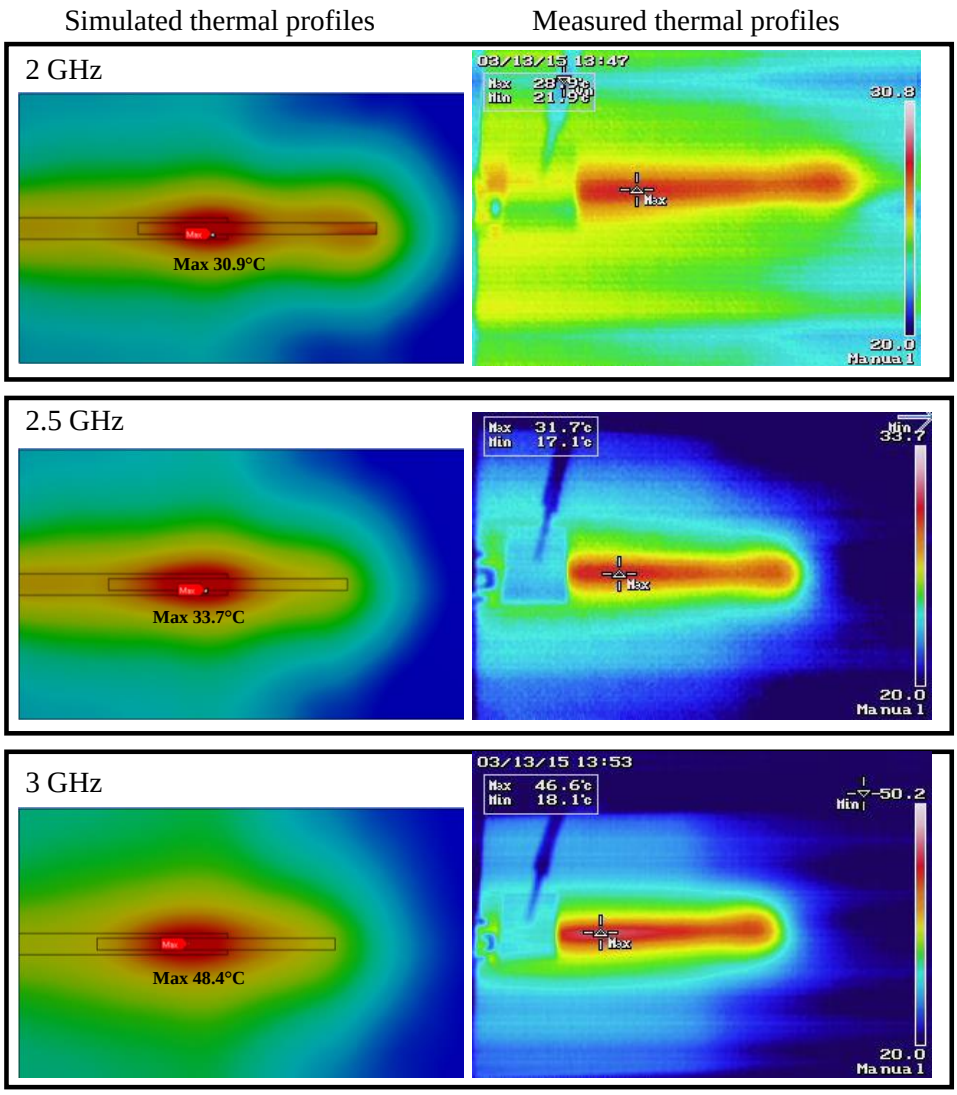

Figure 4.11: Comparison between simulated and measured thermal profile of the antenna under 15W RF excitation power at different operating frequencies.

excitation, the maximum temperature on the antenna surface is 48°C, implying 28°C increase over the room temperature at 3GHz. It is expected that in the presented implementation, the power handling of the antenna will be limited by the maximum operating temperature of the micropumps (70°C) which is much lower than the boiling point of the FC-40 (165°C). Based on simulated data, 15W would be approximately the maximum power handling at the highest operational frequency of 3.5GHz if no additional heat sinking or cooling is employed. It is important to compare the

power handling capability of the presented antenna with the previous implementation reported in [78] that relied on liquid metal, LCP, and RO5880 substrate. A simulation based performance comparison was carried out at 2.5GHz. It was found that in the previous antenna implementation a surface temperature of 35°C is reached with 5W RF power, whereas the presented antenna exhibits the same surface temperature with 15W RF excitation. Similar comparison trend was also observed for other operating frequencies and RF input powers. Hence, it can be concluded that the power handling capability of the presented antenna is 200% better than the previous implementation. In addition, in the presented antenna, replacing metalized plate with liquid metal (mercury, σ= 1.1e6 S/m) is found to decrease the power handling capability by a factor of 2.14. Although liquid metal has a significantly higher thermal conductivity than the plate material (8.30 vs 0.71 W/m/K), both materials are located inside of an identical substrate stack-up that dominates the heat extraction. On the other hand, conductivity of liquid metal is about 50 times lower than copper. As a result, the liquid metal antenna has a lower radiation efficiency (77% vs. 92%) and dissipates the RF power more to generate heat. This shows the suitability of the metalized plate approach for high power handling.

4.6 Miniaturization of Microfluidically Controlled Monopole

We further investigated a similar reconfigurable monopole and miniaturize its height by resorting to a selectively metalized plate. This selectively metalized plate is movable inside the microfluidic channel and used to realize a capacitively (i.e. top) loaded monopole [93]. The presented monopole operates over a wide frequency range of 1.8GHz to 3.2GHz (~1.7:1) with a measured gain of >2.2dB. The antenna height is $0.09\lambda_0$, which is significantly shorter than the monopole in the preceding section. The antenna is also capable of handling the same level of RF

power as shown in the previous section because the same substrate stack-up used for both the antennas.

4.6.1 Antenna Topology

The substrate stack-up and the layout of the frequency tunable miniaturized monopole antenna is shown in Figure 4.12. The antenna consists of a printed circuit board (PCB, R4003C, H_{PCB}=1.52mm, ε_r=3.38, tanδ=0.0027, 17µm thick copper metallization) integrated with a microfluidic channel realized within HPDMS=2mm thick polydimethylsiloxane (PDMS) (ε_r=2.8, tanδ=0.02). The top and bottom surfaces of the PCB partially host the 50Ω microstrip feed line

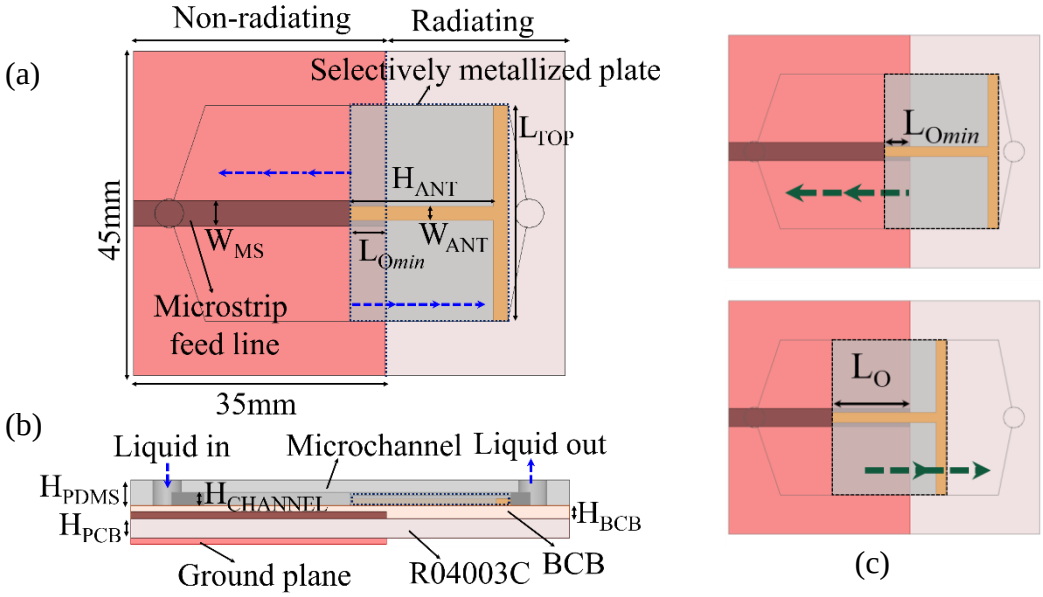

Figure 4.12: Top loaded monopole antenna: (a) Top-view; (b) Substrate stack-up; (c) Frequency tuning mechanism.

(W_{MS}=3.5mm) and ground plane. The microfluidic channel is 0.3mm ($H_{CHANNEL}$) in height and separated from the PCB surface with a 20µm (H_{BCB}) thick Benzocyclobutene polymer (BCB, ε_r=2.6, tanδ=0.0009) coating. Due to the 17µm thick PCB metallization and curvature of the cured BCB film, the BCB thickness on the feed line is expected to vary within the 3-5µm range if no polishing/lapping is applied to the surface. The metallized plate is realized from another PCB board

(RT6006, ε_r=6.15, tanδ=0.0027) that has a thickness of 0.25mm. The PDMS layer and the feed PCB are bonded to each other with BCB. The PDMS layer has the inlet and outlet holes that are connected to external micropumps. The pumps are used to flow a dielectric solution FC-40 (ε_r=1.9, tanδ=0.0005) inside the channel to push the metallized plate. The metalized plate is moved over the feed line (and the ground plane) to achieve continuous frequency tuning by changing the radiating length (Figure 4.12(c)).

4.6.2 Antenna Design

The lower frequency of operation is kept at 1.6GHz as it was selected in the prior work [88]. The size of the ground plane was also kept unchanged (45mm×35mm). At 1.6GHz, the overlap length between the antenna trace and feed line (i.e. L_{Omin}) is designed as 5mm to realize capacitive coupling for an effective RF short [88]. The remaining antenna parameters (monopole height (H_{ANT}), length of the top loading trace (L_{TOP}), and the width of the antenna trace (W_{ANT})) were investigated to obtain a wideband impedance match over the operating frequency range. Parametric studies of H_{ANT}, L_{TOP} and W_{ANT} were performed by simulating the antenna structure in Ansys HFSS v15.0. First, the width of the antenna trace was fixed (W_{ANT}=2mm) and the effect of H_{ANT} and L_{TOP} on impedance matching were investigated while keeping the resonance frequency at 1.6GHz by reducing H_{ANT} and increasing L_{TOP}. From Figure 4.13(a), it is observed that H_{ANT}=20mm and L_{TOP}=20mm provide a good impedance match ($|S_{11}|$<-10dB) whereas smaller H_{ANT} values are not readily matched. Next, the impedance matching at the higher frequencies were investigated as the antenna was retracted over the feed line by overlap length (L_O). The impedance matching especially degrades as the top loading approaches to the ground plane due to the enhanced capacitive loading. This impedance degradation can be alleviated to a certain point by

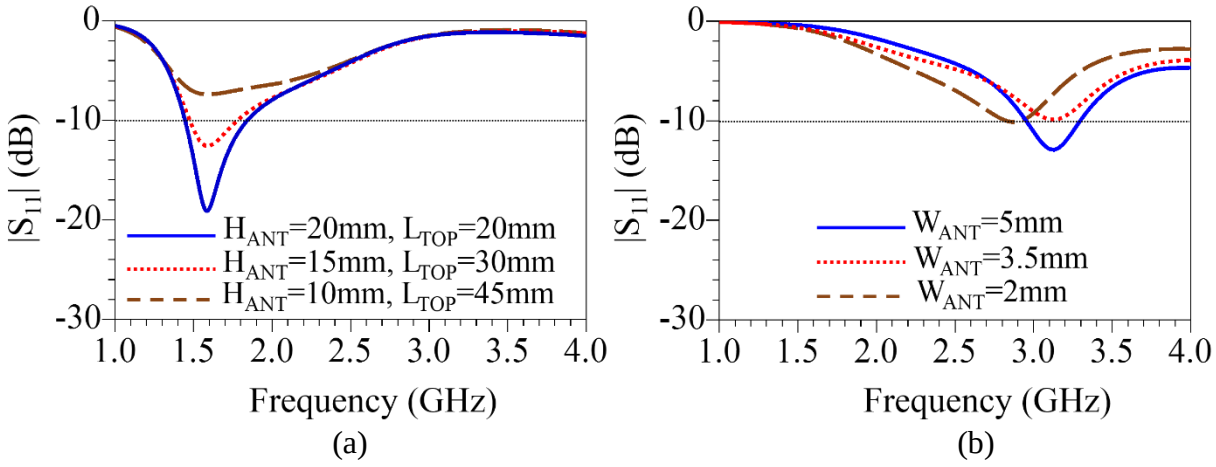

Figure 4.13: Simulated $|S_{11}|$ response of the antenna for different (a) H_{ANT} and L_{TOP} and (b) W_{ANT}.

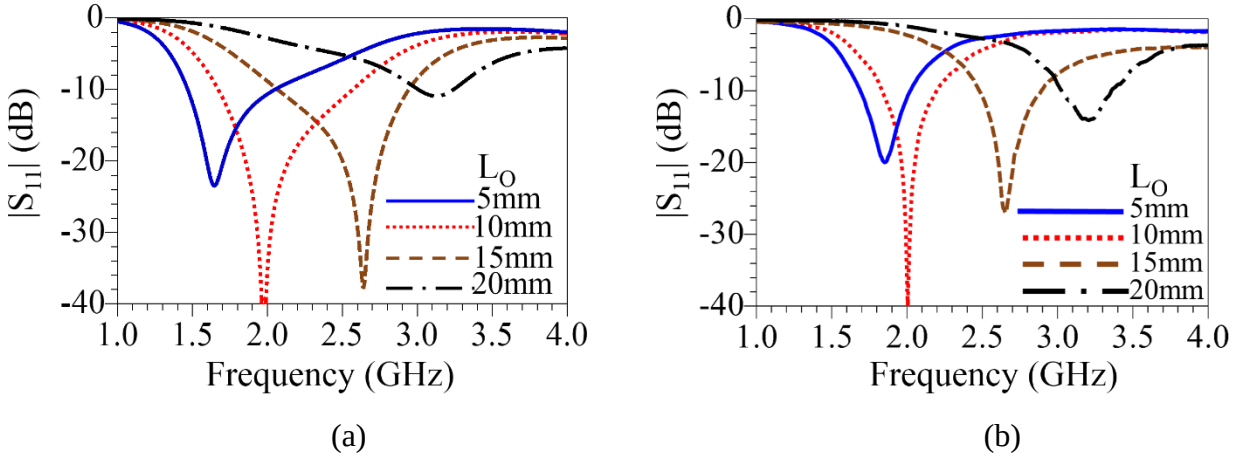

Figure 4.14: $|S_{11}|$ response of the antenna as overlap length L_O is varied: (a) Simulation; (b) Measurement.

optimizing the antenna width (W_{ANT}). As seen in Figure 4.13(b), at the high frequency end, W_{ANT}=3.5mm provides an improvement. However, although larger values of W_{ANT} (such as 5mm) improved high frequency matching further, they cause impedance mismatches at 1.6GHz. Hence, these impedance matching conditions defines the antenna geometry (WANT= 3.5mm, H_{ANT}=20mm, LTOP=20mm). Consequently, the maximum achievable antenna tuning range gets determined as 1.6GHz to 3.2GHz. Figure 4.14(a) depicts the simulated $|S_{11}|$ performance as L_O is varied from 5mm to 20mm with 5mm increments. This agrees well with the measured data in Figure 4.14(b) that shows an operating range from 1.8GHz to 3.2GHz. The simulated peak gain

and radiation efficiencies are (2.2dB, 63.4%), (2.2dB, 68.3%), (2.1dB, 65.1%) and (2.3dB, 58.7%) at the resonance frequencies of 1.6GHz, 2.0GHz, 2.6GHz and 3.2GHz, respectively.

4.6.3 Experimental Verification

The microstrip feed line was etched on top of the RO4003C substrate using standard photolithography and copper etching techniques. The insulating layer of BCB was then spun on top of the antenna substrate and thermally cured. The microchannel was fabricated using soft-lithography technique. The channel containing the selectively metallized plate was then bonded to the antenna substrate using the customized bonding recipe discussed in [94]. The piezo-electric micropumps (mp6-OEM, Bartels) were configured to operate with 235Vpp 100Hz signal for

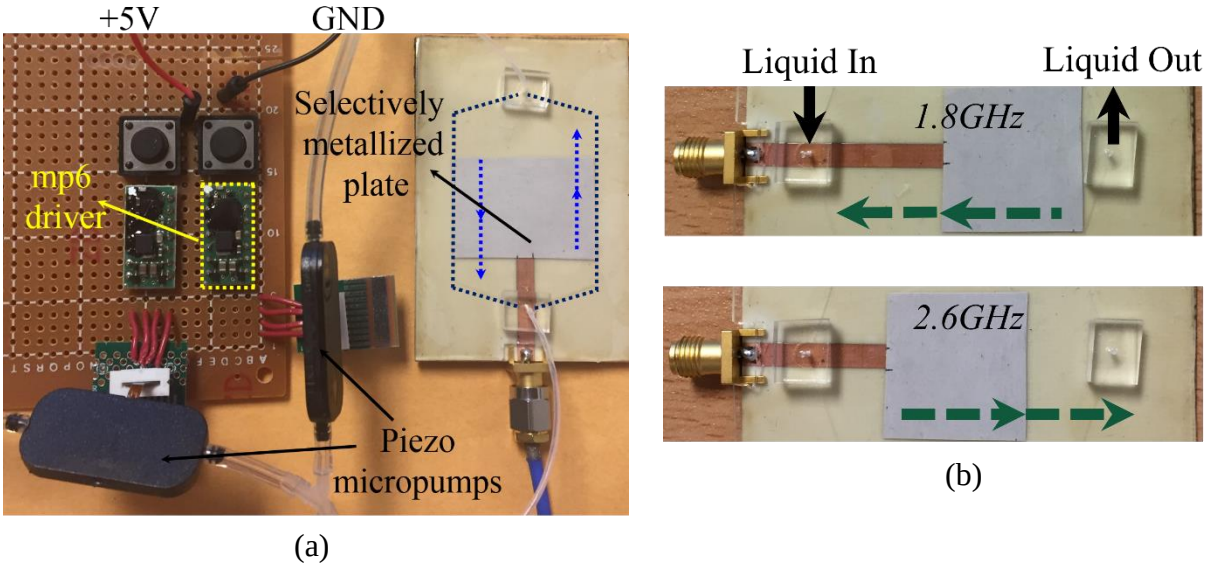

Figure 4.15: Antenna prototype (a) Entire set-up including pumps; (b) Snapshots of the antenna being reconfigured.

optimum flow rate of the FC-77 dielectric solution. The dielectric solution fills up the channel and in turn pushes the metallized plate. Figure 4.15 shows the antenna prototype and the snapshots as it is being reconfigured over the operating bandwidth. The measured and simulated normalized radiation patterns in E and H-planes at 1.8GHz and 2.6GHz are shown in Figure 4.16. The

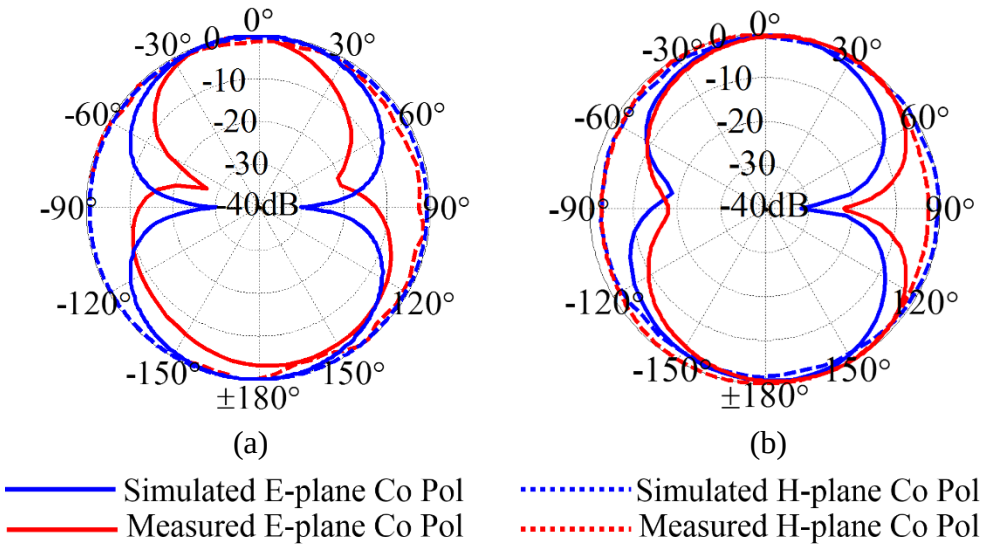

Figure 4.16: Normalized radiation pattern of the antenna at (a) 1.8GHz; (b) 2.6GHz.

measured and simulated patterns are in good agreement. The peak gain of the antenna was measured to be 2.2dB which is in good agreement with simulation values.

4.7 Conclusion

A microfluidically controlled frequency tunable monopole antenna was presented. The monopole was implemented from a metallized plate within a microfluidic channel and excited through capacitive coupling. The antenna exhibited a frequency tuning range from 1.7GHz to 3.5GHz with >2.4dB realized gain. Specifically, it was found that the presented compact antenna could operate with 15W of continuous RF power being limited by the highest operation frequency and maximum temperature handling of the utilized micropumps. The concept of microfluidically controlled selectively metallized plate was then used to realize a top loaded monopole antenna. The antenna is $0.09\lambda_0$ in height and exhibits a wide 1.7:1 tuning range with stable radiation pattern. It can be concluded that using metallized plate as the reconfigurable element offers the advantage of developing miniaturized reconfigurable antennas with high efficiency and power handling capability.

CHAPTER 5: MICROFLUIDICALLY SWITCHED FREQUENCY TUNABLE DIPOLE ANTENNA

5.1 Note to Reader

Portions of this chapter have been previously published in [100], and have been reproduced with permission from IEEE. Permission is included in Appendix A.

5.2 Introduction

The increasing demand for compact communication systems that can dynamically access different frequencies of the spectrum has generated strong interest for small, frequency-reconfigurable antennas. As discussed in Chapter 2 integration of PIN diodes [7-9], MEMS switches [13-16] and varactors [10-12] with the antenna structures have shown to achieve frequency reconfiguration capabilities. To provide enhanced reconfiguration and power handling capabilities, liquid metals were recently proposed for frequency tuning. For such microfluidically controlled systems, liquid metal shape is altered to mechanically change the radiating length [79] or, alternatively, to act as a shorting switch that tunes the antenna electrical length [67]. Although antennas implemented using liquid metal have shown wide tunability range other aspects such as power handling and oxidization of liquid metals remain as challenges to overcome.

As an alternative, in this chapter we propose a frequency tunable dipole antenna that utilizes a selectively metallized plate within the microfluidic channel. The metalized plate acts as a shorting switch and changes the current path or antenna geometry to tune its resonance frequency. We note that the microfluidic channel carrying the metalized plate is bonded to the printed antenna

with a 12 µm-thick low-loss Benzo-cyclobutene (BCB) layer (ε_r=2.65, tanδ=0.008). The proposed method of using a selectively metallized plate as a microfluidically controlled switch paves the way for various microfluidically reconfigurable RF devices that are liquid-metal-free, non-toxic, and reliable.

5.3 Microfluidically Switched Dipole Antenna

5.3.1 Antenna Topology

Figure 5.1 depicts the antenna and associated microfluidic channel. The antenna is a conventional meandered dipole, fed with a 50Ω coaxial cable. It is printed on a 0.0254 mm-thick Rogers Ultralam 3850 liquid crystal polymer (LCP) based substrate (εr=2.9, tanδ=0.0025). A 0.75

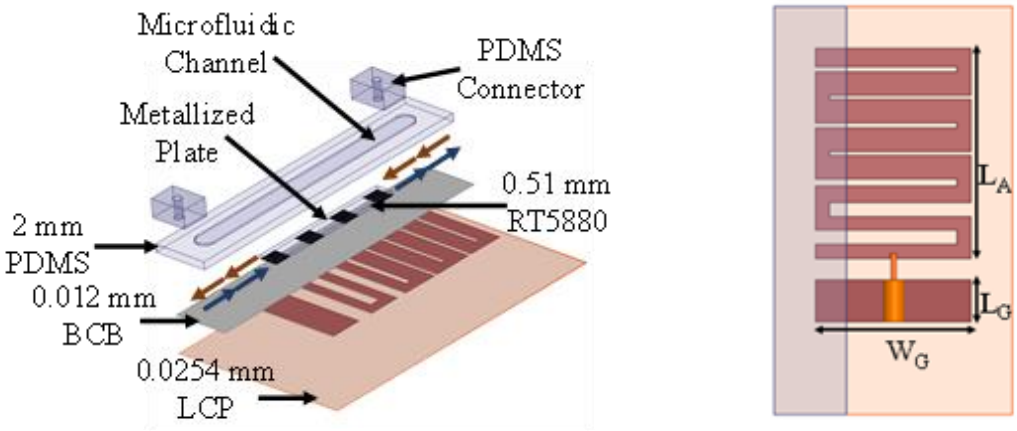

(a) (b)

Figure 5.1: (a) Substrate stack-up of microfluidically tunable dipole antenna; (b) Top view of the antenna.

mm-thick, 5.2 mm-wide microfluidic channel, prepared in 2 mm-thick 15 mm-wide polydimethylsiloxane (PDMS, εr=2.8, tanδ=0.02), is bonded to the edge of the antenna using a 12 µm-thick BCB layer. The microfluidic channel carries a selectively metalized plate (RT5880, ε_r=2.2, tanδ=0.0009) that moves over the antenna slots to selectively short the antenna arms and therefore its current path. Figure 5.1(b) shows the antenna dimensions. The reconfiguration principle is shown in Figure 5.2. As shown in the figure, when the selectively metallized plate is

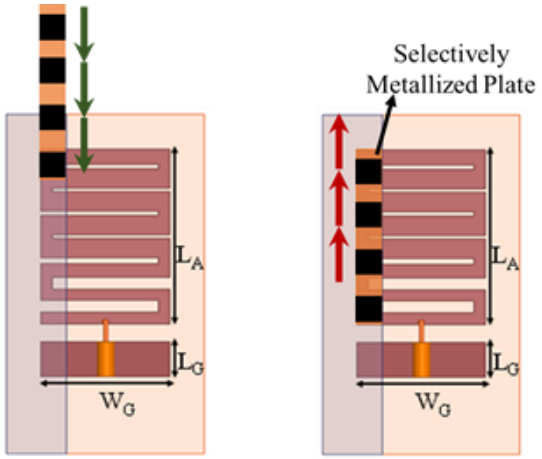

Figure 5.2: Frequency reconfiguration technique of the dipole antenna

made to slide over the antenna trace, it shorts the radiating slots of the antenna and thereby reducing the electrical length of the antenna.

5.3.2 Design

Simulation studies were initially carried out to determine the dimension of the metallized area needed to create an RF short across two adjacent antenna traces. A 50Ω microstrip line (printed on 1.57mm-thick RT5880 substrate) loaded with the BCB (0.012 mm) and PDMS (2 mm) layer was modelled in Ansys HFSS v15.0. A gap of 0.5 mm width (same dimension as the maximum slot width) was placed along the length of the line. Different sizes of metallized plates were then used to capacitively short the line gap, and the corresponding $|S_{21}|$ was observed. We note that a metallization area of 5mm x 5mm was found to create an RF short with < 0.25 dB insertion loss.

The antenna was designed to resonate at 0.9 GHz when none of the slots were shorted. To tune the antenna to a different frequency, the metallized plate moves along the antenna's edge (see Figure 5.1(a)) creating a shorting effect between adjacent meandered traces. As the adjacent traces are shorted sequentially, the current density over the antenna geometry changes (see Figure 5.3). When the plate completely resides on the antenna, all adjacent traces are shorted and the highest

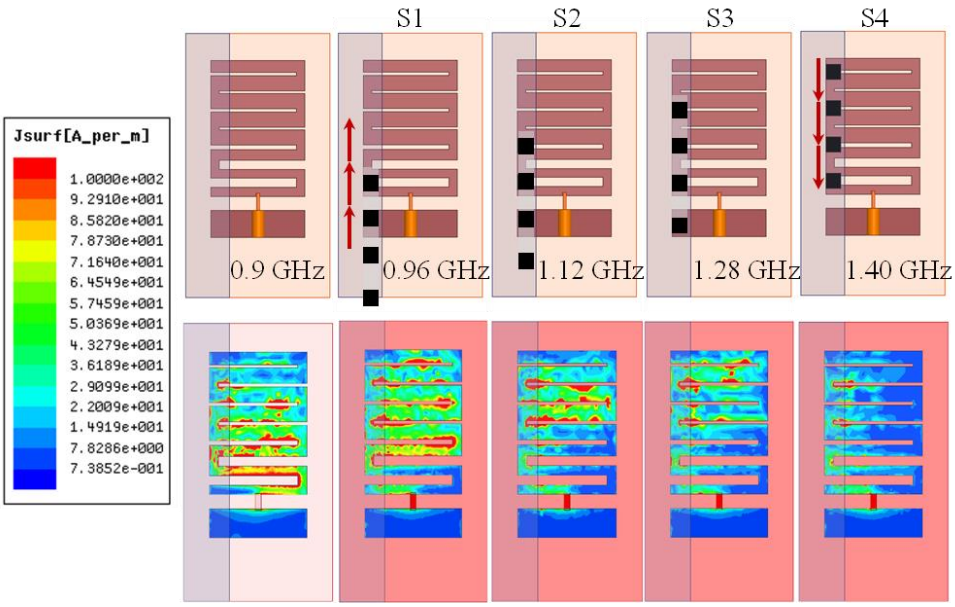

Figure 5.3: Current density distribution on the antenna's surface at different resonance frequencies

resonance frequency is achieved, viz. 1.4GHz. Due to the capacitance-based RF shorting, the current density shifts to the left side of the antenna and flows over a physically shorter length. Figure 5.4(a) shows the simulated $|S_{11}|$ as the metalized plate moves along its edge. Specifically, the antenna exhibits $|S_{11}|$<-10dB resonances at 0.9 GHz, 0.96 GHz, 1.12 GHz, 1.28 GHz and 1.4 GHz with 2.68%, 4.23%, 4.19% 5.85% and 9.23% bandwidths, respectively. The corresponding simulated realized gain patterns are shown in Figure 5.4(b). The antenna exhibits 1.02 dB, 1.15 dB, 1.17 dB, 1.47 dB and 1.82 dB realized peak gains with 82.17%, 80.15%, 78.27%, 78.15% and 75.32% radiation efficiencies, respectively.

5.3.3 Experimental Verification

Standard PCB etching procedures were used to fabricate the antenna (on 0.0254 mm Ultralam 3850) and the metallized plate (on 0.51 mm RT5880). The steps involved resist spinning, photolithography, and copper etching. The microfluidic channel was fabricated in PDMS using soft-lithography. A very thin layer of BCB was then spun on top of the antenna and baked in an

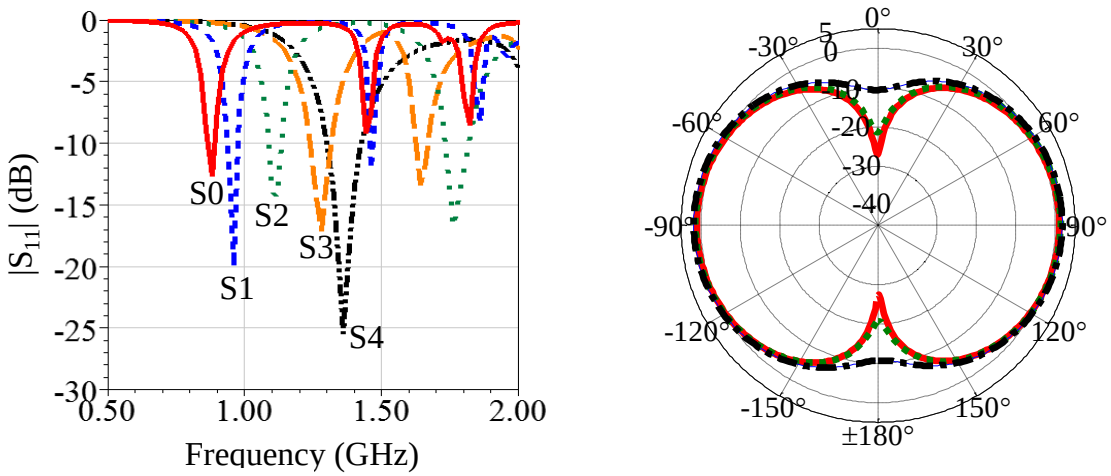

Figure 5.4: (a) Simulated $|S_{11}|$ of the antenna; (b) Simulated gain pattern of the antenna at different frequencies of the operating bandwidth.

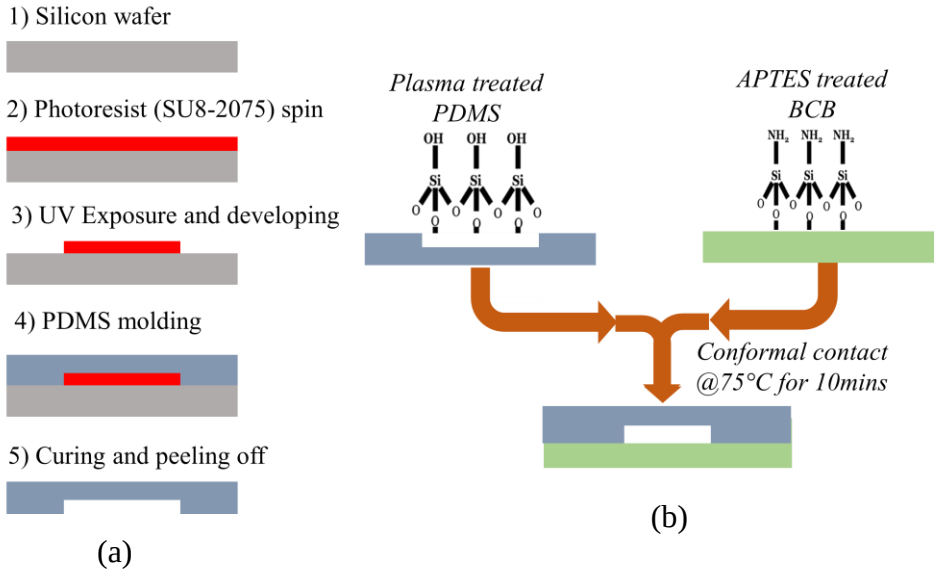

Figure 5.5: Fabrication process for (a) Making the channel; (b) Recipe for bonding the channel to the BCB coated printed circuit board.

oven at 200°C to harden the BCB layer and ensure that no air bubbles were trapped in it. After the BCB was cured, a customized recipe was used for bonding the BCB to the PDMS layer (Figure 5.5). The channel was then filled with low-loss FC-40 (ε_r=1.9, tanδ=0.0005) solution, and two unidirectional micropumps were used to generate a bi-directional flow system. The fabricated

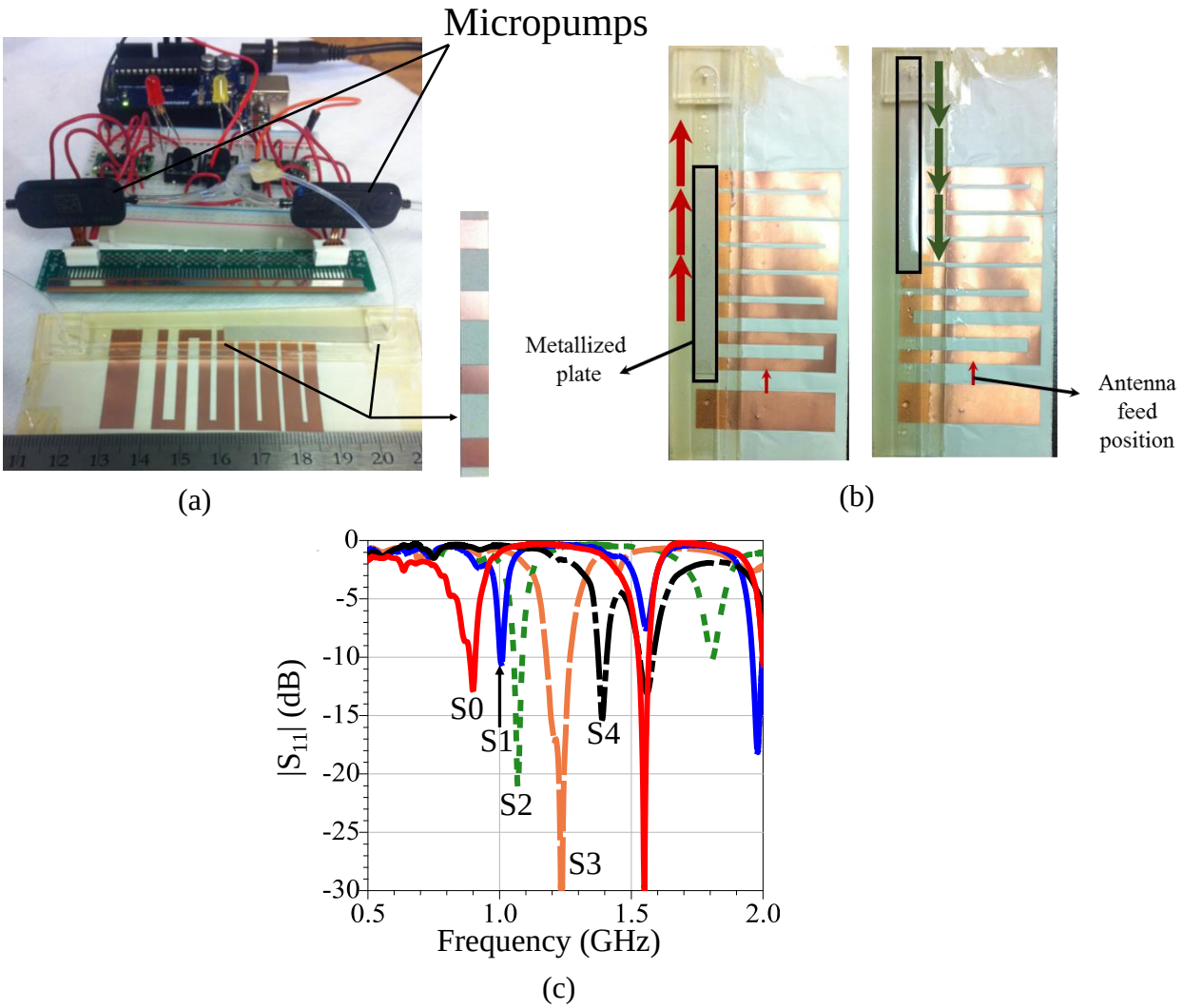

Figure 5.6: (a) Fabricated antenna on liquid crystal polymer substrate; (b) Snapshots of the antenna being tuned; (c) Measured $|S_{11}|$ response of the antenna.

prototype is shown in Figure 5.6(a). Figure 5.6(c) shows the $|S_{11}|$ response of the antenna as the plate moved over its radiating slots. It is seen that the antenna resonance shifts from 0.88 GHz to 1.39 GHz.

5.4 Microfluidically Tunable Textile Antenna

5.4.1 Antenna Topology

A textile version of the dipole antenna described above was fabricated and experiments were conducted to incorporate the microfluidic reconfiguration technique on it. A major challenge

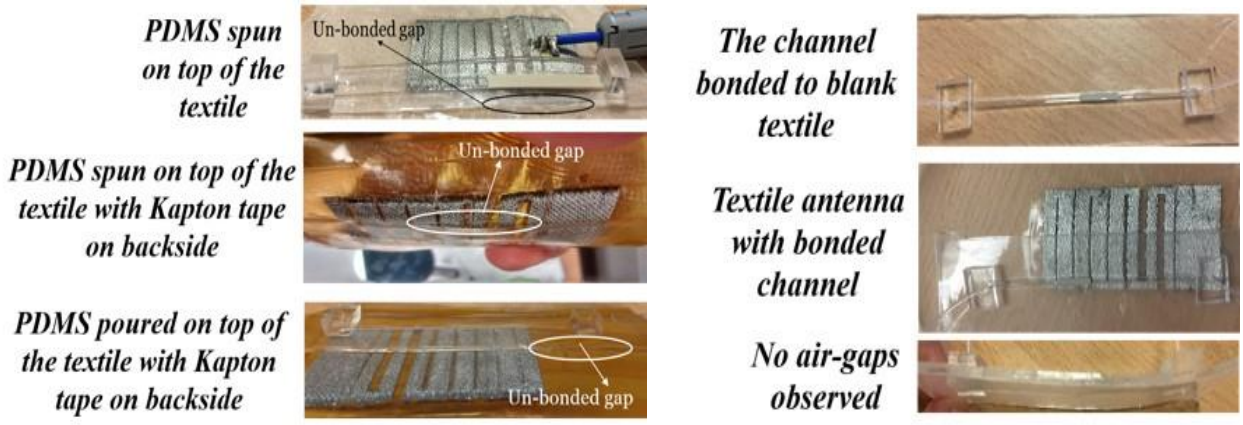

Figure 5.7: (a) Experimental results with bonding the microfluidic channel to the textile antenna; (b) Alternative bonding technique which uses an intermediate blank textile layer.

has been the ability to bond the PDMS microchannel enclosing the metallized plate onto the textile surface. Figure 5.7 summarizes the results of our bonding experiments. At first, the bonding was carried out using PDMS as the intermediate layer between the open side of the channel and the textile surface. As seen in Figure 5.7(a) this resulted in un-bonded air gaps between the two surfaces, leading to leakage of the liquid as it would flow through the channel. To prevent this, an alternative technique of using textile itself as the intermediate layer was investigated (Figure 5.7(b)). In this technique, a blank textile surface was coated by spinning PDMS on top of it. The PDMS seeps inside the pores of the textile and forms an impermeable PDMS-textile layer. The microfluidic channel enclosing the metallized plate was then bonded to the PDMS-textile layer. This sealed channel was then adhered to the textile antenna surface using BCB as an adhesive.

$|S_{11}|$ measurements for the antenna that utilizes the PDMS-textile as the intermediate layer demonstrated that the effective separation between the textile trace and the metallized plate inside the channel was increased. Consequently, the metallized plate area (5mm×5mm) that was found to be sufficient to create an RF short in the PCB version of the antenna did not provide the same shorting effect and frequency tuning capability was lost. To determine the metallized plate overlap

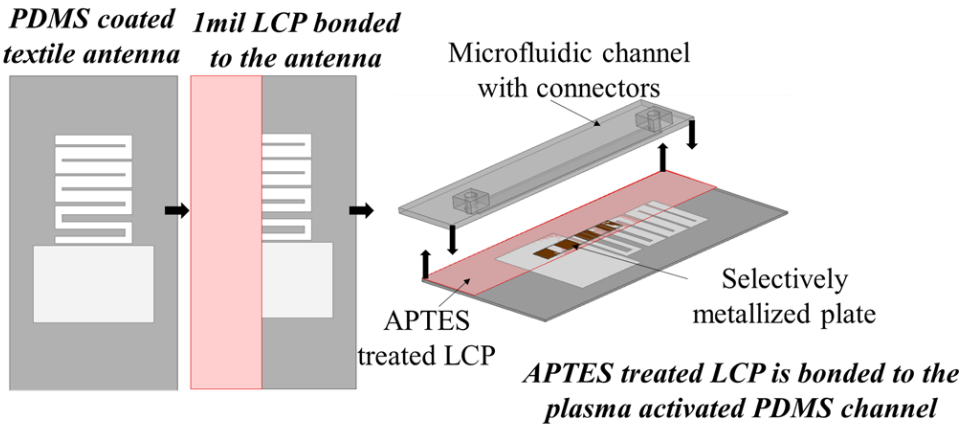

(a)

(b)

Figure 5.8: (a) Fabrication process of the microfluidically tunable textile antenna; (b) Fabricated prototype.

area needed to create the RF short, experimental studies were conducted by enclosing the metallized plate between the microchannel and the textile antenna with the PDMS-textile being used as the intermediate layer. From these experiments, it was observed that the metallized area was needed to be increased considerably (22mm×10mm) to short the antenna slots. This was a hindrance to the conformability/flexibility of the antenna.

To prevent this excessive increase in the metallized plate dimensions, we continued to investigate alternatives to bond the channel to the textile surface with minimal separation between two. The process that yielded success can be described as follows (see Figure 5.8). PDMS was spun on top of the textile surface (2000pm). Subsequently, 1 mil thick LCP layer was placed on

top of the PDMS. Pressure was applied to ensure the LCP layer was adhering to the textile surface with no air gaps. This stack-up under the applied pressure was left to cure overnight. The thin intermediate PDMS layer cured and acted as the adhesive layer between the textile and the LCP surface. Next, the channel enclosing the metallized plate was bonded to the LCP layer (using the procedure described in Chapter 2). Different metallization areas were again experimentally investigated and it was concluded that metallization area of 11mm×8mm was adequate to provide an RF shorting capability.

5.4.2 Experimental Verification

The experimental set-up with the micropump control unit and the antenna is shown in Figure 5.9(a). The corresponding measured $|S_{11}|$ response of the antenna at different switching states is shown in Figure 5.9(b). As the metallized plate is moved over the radiating slots (similar to the tuning principle described in Figure 5.2), the resonance frequency of the antenna shifts from ~900MHz to 1.4GHz as also predicted with the simulation based studies. The resonance frequencies recorded at the different switching states are: S0=893.8MHz, S1=993.8MHz, S2=1206MHz, S3=1322MHz, and S4= 1400MHz.

The radiation performance of the fabricated antenna was measured in an anechoic chamber. The initial gain measurements demonstrated a low realized gain value (-5dBi) although the antenna was well matched to the feed line. Further investigations demonstrated that the leakage to the unbalanced coaxial cable feed from the smaller ground plane of the antenna was the reason for this gain drop. This leakage situation may have been exacerbated in the anechoic chamber as well due to the usage of physically long coaxial cables. Due to the time constraints in constructing a differential balanced feed, the alternative of enlarging the ground plane during the anechoic chamber simulations was adopted. In addition, the feed cable transition was improved by soldering

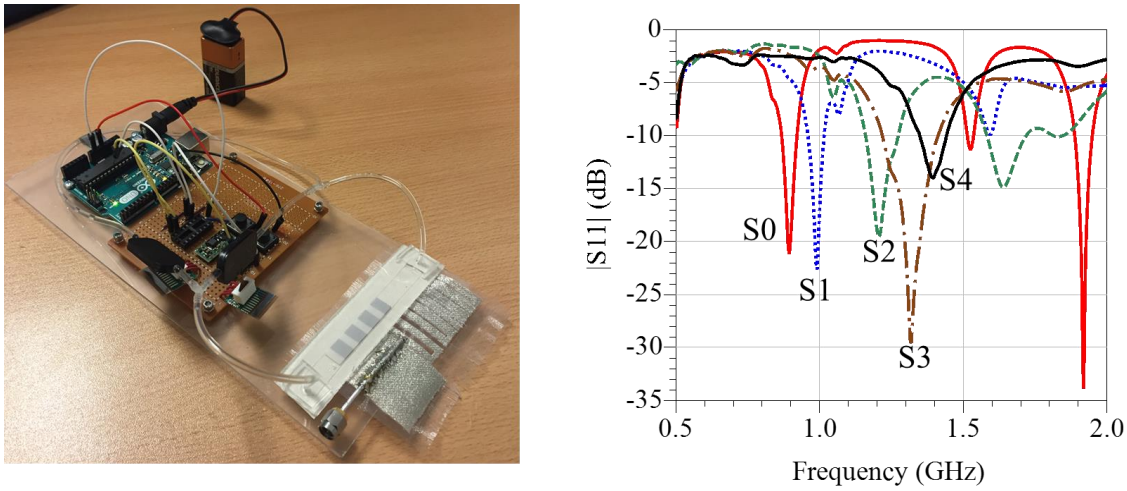

(a) (b)

Figure 5.9: (a) Experimental set-up; (b) Measured $|S_{11}|$ response of the antenna.

the outer conductor of the coaxial cable to the ground plane. The enlarged ground plane is approximately 2-3 times the ground plane area of the fabricated textile antenna. Due to this enlargement, the radiation patterns were slightly tilted than expected from a small monopole antenna. Figure 5.10 presents the measured radiation patterns in two primary cuts as the antenna is reconfigured to operate at different frequencies. The measured peak gain in these cuts remains around ~0.7dBi for the un-tuned monopole (S0), ~0.98dBi for first tuning position (S1), ~1.32dBi for the second (S2), ~0.67dBi for the third (S3) and ~0.76dBi for the last position (S4). These results agree with simulation based expectations. Further implementations of the antenna should consider larger ground planes or differential feeds.

5.5 Conclusion

A microfluidically tunable textile antenna was demonstrated in this chapter. The antenna is shown to tune over a frequency range of 900-1400MHz. The antenna performance was comparable to its printed circuit board prototype. The usage of a selectively metallized plate as a shorting switch was demonstrated for the first time to tune a textile antenna. Through the implementation of tunable monopoles and dipoles the advantages of microfluidics based

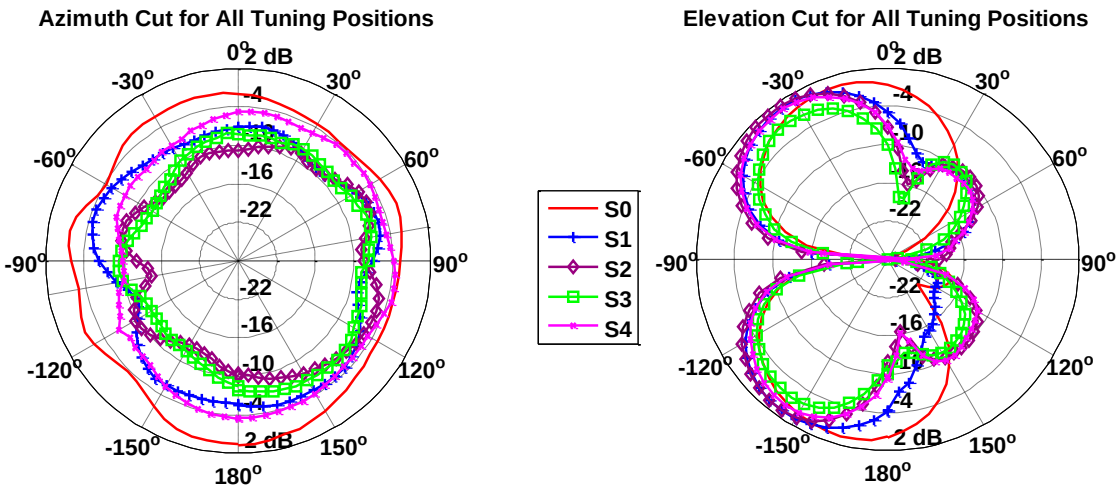

Figure 5.10: Measured realized gain patterns of the antenna at different switching states.

reconfiguration have been established. Although such devices show wide improvement in performance, they limit the application of microfluidic reconfiguration to discrete components. To demonstrate a system level integration of microfluidic reconfiguration a surface microwave imaging system is discussed in the next chapter.

CHAPTER 6: HIGH RESOLUTION SURFACE MICROWAVE IMAGING SYSTEM USING MICROFLUIDICALLY CONTROLLED METALLIZED PLATE

6.1 Introduction

Microwave imaging has progressively found its application in varied fields such as breast cancer screening [96] on account of its non-destructive and non-invasive diagnostic capabilities. Commonly used imaging configurations observe the interaction of the sample with microwaves and then use the scattered fields for reconstructing the image. Scanning imaging systems measure the amplitude and/or phase values of the reflected signals from the sample and post process the variations to determine the material properties. To reduce the post processing complexity, the imaging system presented in this chapter uses the shift in resonant frequency of a complementary open loop resonator when loaded with the sample to be imaged. A novel technique based on microfluidically controlled metallized plate has been employed as a low-cost RF readout circuitry to select and measure the response of each resonator from the 1D measurement plane [95]. In this chapter we have discussed the design procedure of the microfluidic controlled imaging system, the fabrication procedure of the sensor array and the control mechanism used for accurate positioning of the metallized plate inside the microchannel. The results from experimental verification of the system have also been included in this chapter.

6.2 Operating Principle

High resolution microwave imaging arrays have been a challenge due to the need to tightly pack many pixels and individually access them. This section introduces the utilization of

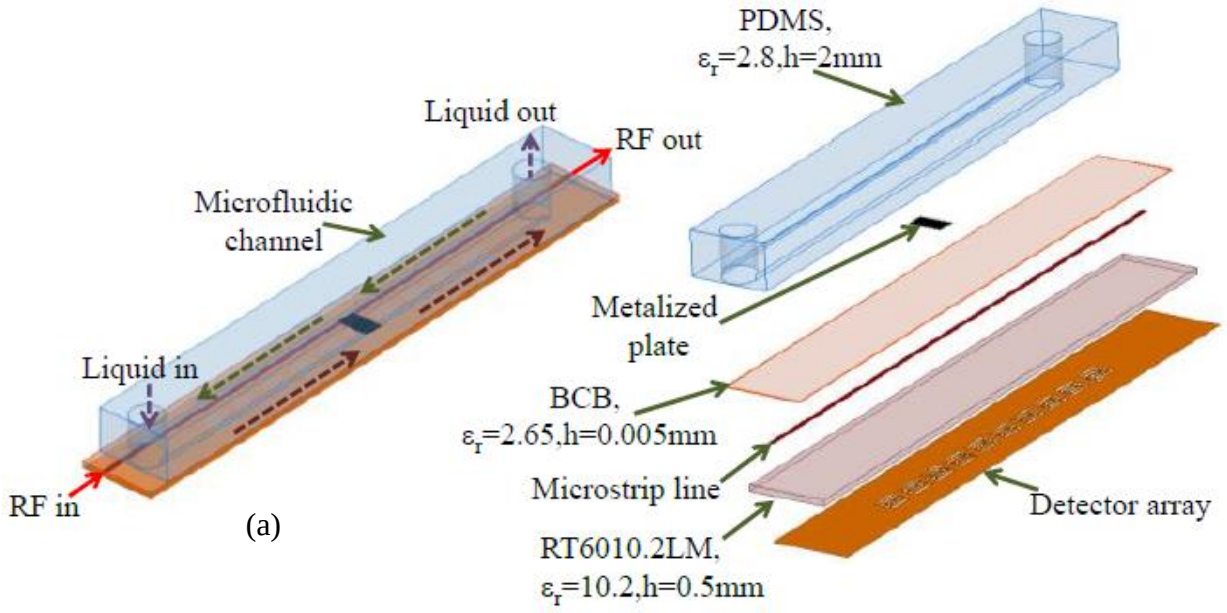

Figure 6.1: Sub-wavelength high resolution sensor array (1D) consisting of microfluidically loaded microstrip line based read-out circuit.

microfluidic reconfiguration techniques as RF read-out circuitries. The novel approach is shown in Figure 6.1 for a 1D setup. It relies on using a microfluidically repositionable metalized plate within a microfluidic channel. The proposed system consists of the microfluidic channel (made using Poly-dimethyl siloxane, PDMS) bonded to a printed circuit board (PCB) that carries the pixels (complementary open loop resonators) using benzocyclobutene (BCB). This bonding technique involves chemical treatment of the BCB layer which will be discussed later in the chapter. This bonding technique ensures the close proximity of the variable RF load (metallized plate) to the stationary metallization traces on the PCB (microstrip lines). As such, this close proximity to the microstrip line can be utilized as an effective RF short between the line and the plate. When the plate is repositioned to bridge the gap between the microstrip line and a resonator, the S_{21} reading can be used to detect the resonance frequency (or voltage) of the resonator. This technique is depicted in Figure 6.2. The resonance frequency of the resonator is visible in the S_{21}

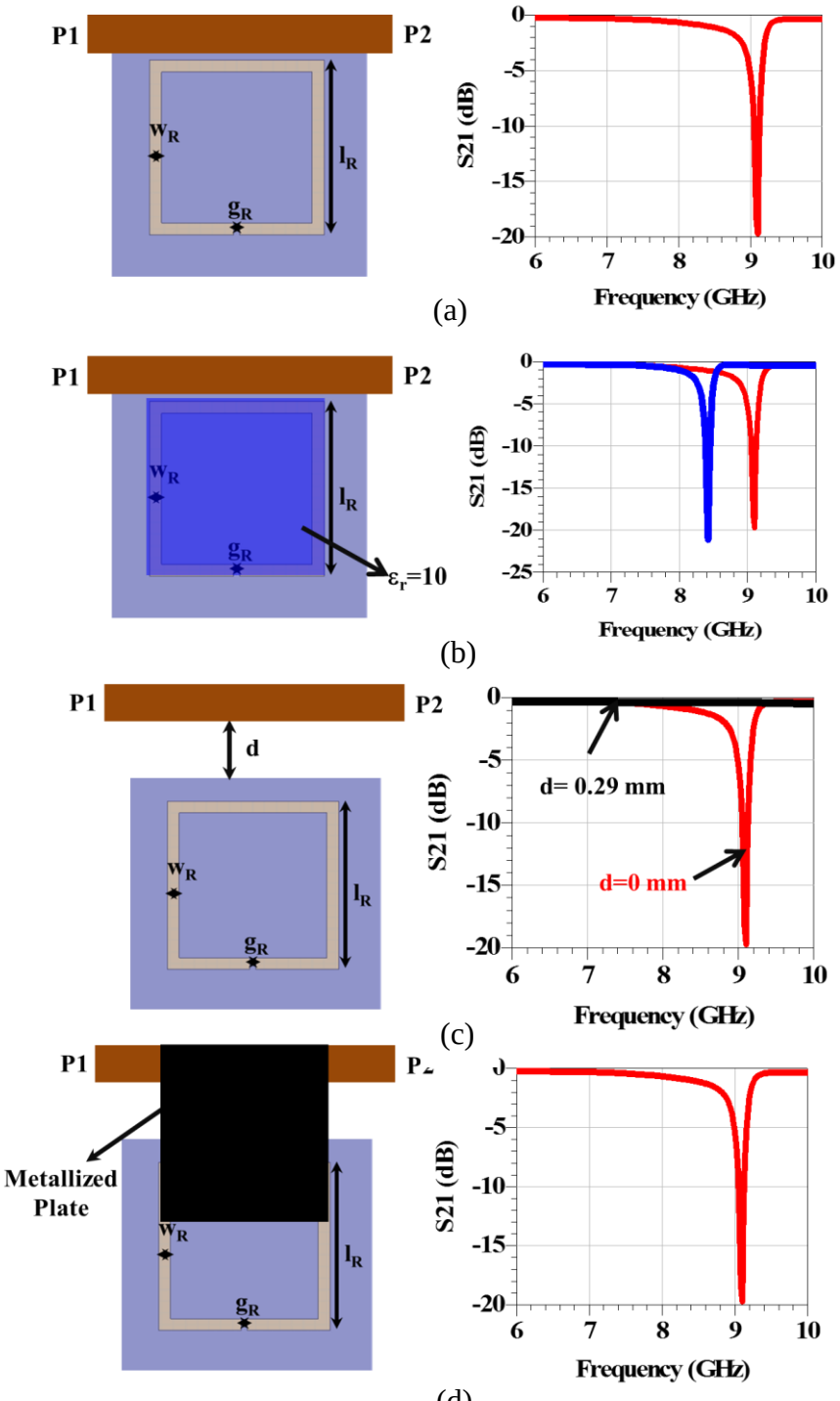

Figure 6.2: Operating principle of the microfluidically controlled imaging array; (a) Microstrip line loaded with the resonator; (b) Resonator loaded with sample to be investigated; (c) Effect of separation between microstrip line and resonator; (d) Resonator coupled to microstrip line using metallized plate.

response of the microstrip line when the resonator is placed next to it (d = 0mm) (Figure 6.2(a)). As the distance between them is increased the electromagnetic coupling between them decreases. At a certain distance (e.g. d =0.29mm in this case) the resonator does not show any effect on the S_{21} response (Figure 6.2(c)). To re-couple the resonator and the microstrip for this increased distance, the metallized plate is used (Figure 6.2(d)). When the resonator is loaded with a dielectric material, the shift in the resonance frequency and the drop in quality factor of the resonator can be used to determine the electrical permittivity of the material. This operation of individually investigating each resonator is show in Figure 6.3. This approach allows to closely pack many resonators within available area and can be straightforwardly extended to 2D imaging with either a motor controlled stage or addition of multiple rows. The next section discusses in detail the design procedure of the sensing array.

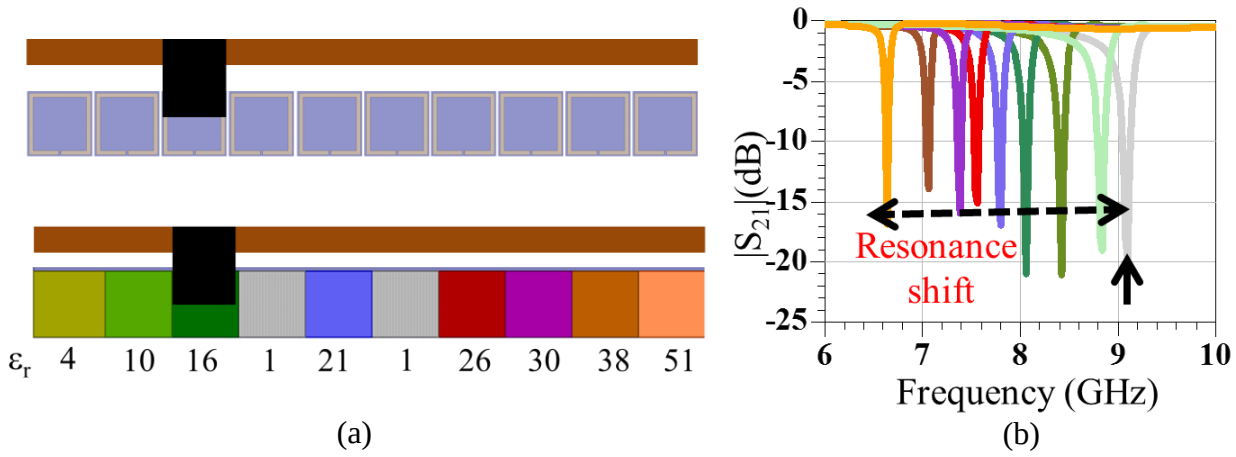

(a) (b)

Figure 6.3: (a) 1D array of resonators loaded with materials of different electrical permittivity; (b) Corresponding $|S_{21}|$ response of the resonators.

6.3 Sensing Array

6.3.1 Design

The 1D array of resonators as described in the previous section form the sensing/detecting part of the imaging system. The first step towards designing the sensor array is choosing the

substrate for the microstrip line. In this design Rogers 6010 substrate (h = 25mils, ε_r = 10.2, tanδ = 0.0025) was selected as the substrate of the microstrip line. The high permittivity of the material enables implementation of thinner 50Ω microstrip lines which reduce the pixel size of the imaging system. The 50Ω microstrip line was designed using the substrate stack-up depicted in Figure 6.1. The width of the microstrip line was tuned to obtain a good match (|S11| < 15dB) over the desired frequency range 6-12GHz. (The selection of this frequency range was determined from the availability of off the shelf voltage controlled oscillators. This was done with a goal to potentially replace the vector network analyzer with VCO as the RF signal source. This will lead to implementation of the imaging system as a standalone unit). In the next step the complimentary open loop resonator (COLR) was designed. At first, the COLR was etched on the ground plane in the same vertical plane as the microstrip line (Figure 6.4(a)). The dimensions of the COLR (Figure 6.4(b)) were chosen to set its resonance frequency to 11.8GHz in order to utilize the entire frequency band of interest (6-12 GHz). The dimensions of the resonator obtained from full wave simulation

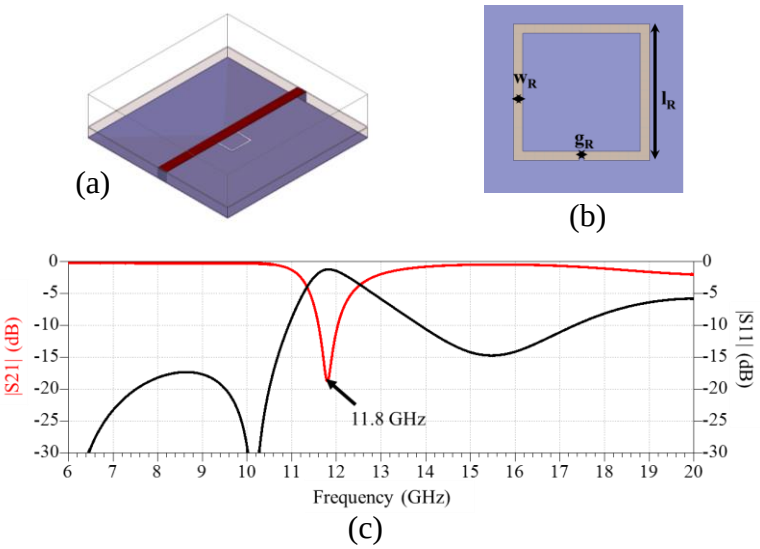

Figure 6.4: (a) Simulation set-up for designing a single open loop resonator; (b) Dimensions of the resonator; (c) Simulated response of the resonator loaded microstrip line.

of the structure were l_R = 1.45mm, w_R = 0.1mm, g_R = 0.05mm. The response of the single resonator loaded microstrip line is shown in Fig. 6.4 (c). The resonance is observed at 11.8GHz as expected.

To determine the spacing needed to de-couple the resonator from the microstrip line parametric. studies were performed wherein the distance d (Figure 6.5(a)) was incremented and the corresponding $|S_{21}|$ was observed (Figure 6.5(b)). When the sensor array is comprised of just a single resonator d = 0.8mm is needed to obtain a flat $|S_{21}|$ response. For an 8x1 array of resonators (Figure 6.5(c)), the same distance d = 0.8mm does not de-couple the resonators from the read-out line. Parametric studies were further performed till no coupling was observed in the $|S_{21}|$ and it is observed that d=1.2mm is needed for the de-coupling for the 8×1 array. These parametric studies help in understanding the correlation between the number of sensing elements (resonators) and the pixel size (smallest detectable area) of the imaging system. For e.g., keeping the separation

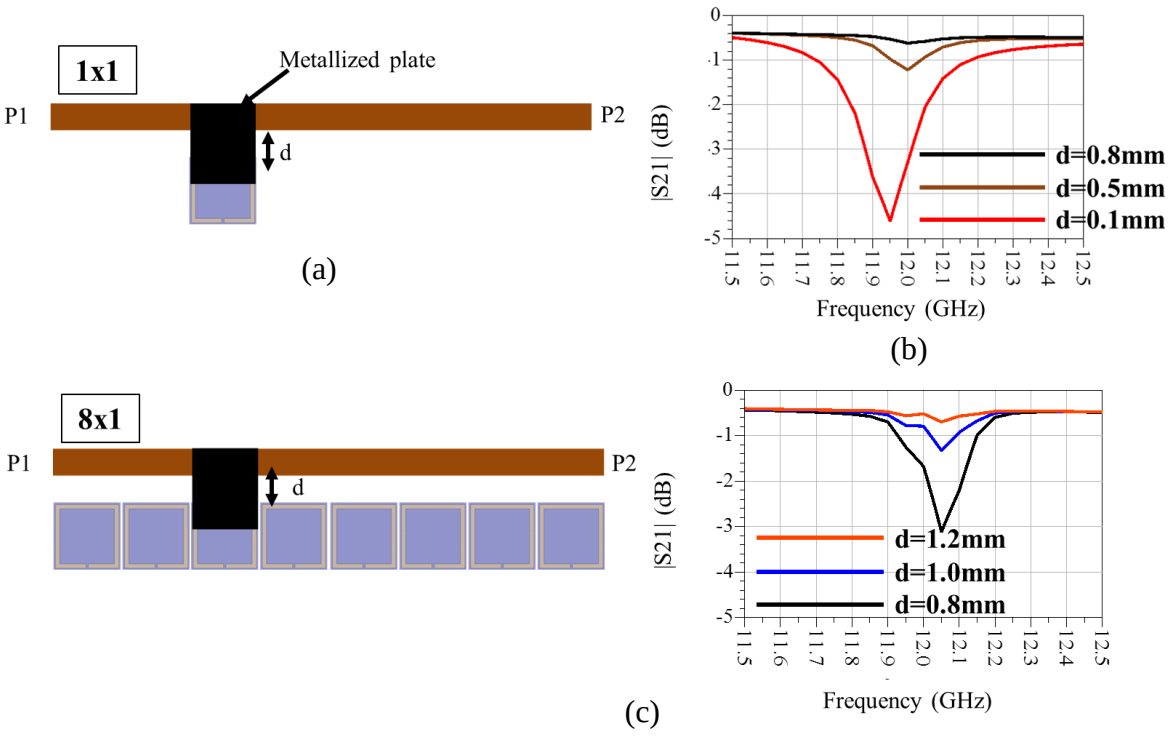

Figure 6.5: (a) 1x1 array of resonator coupled to read-out microstrip line; (b) $|S_{21}|$ response of the system as d increases; (c) 8×1 array of resonators and its corresponding $|S_{21}|$ response.

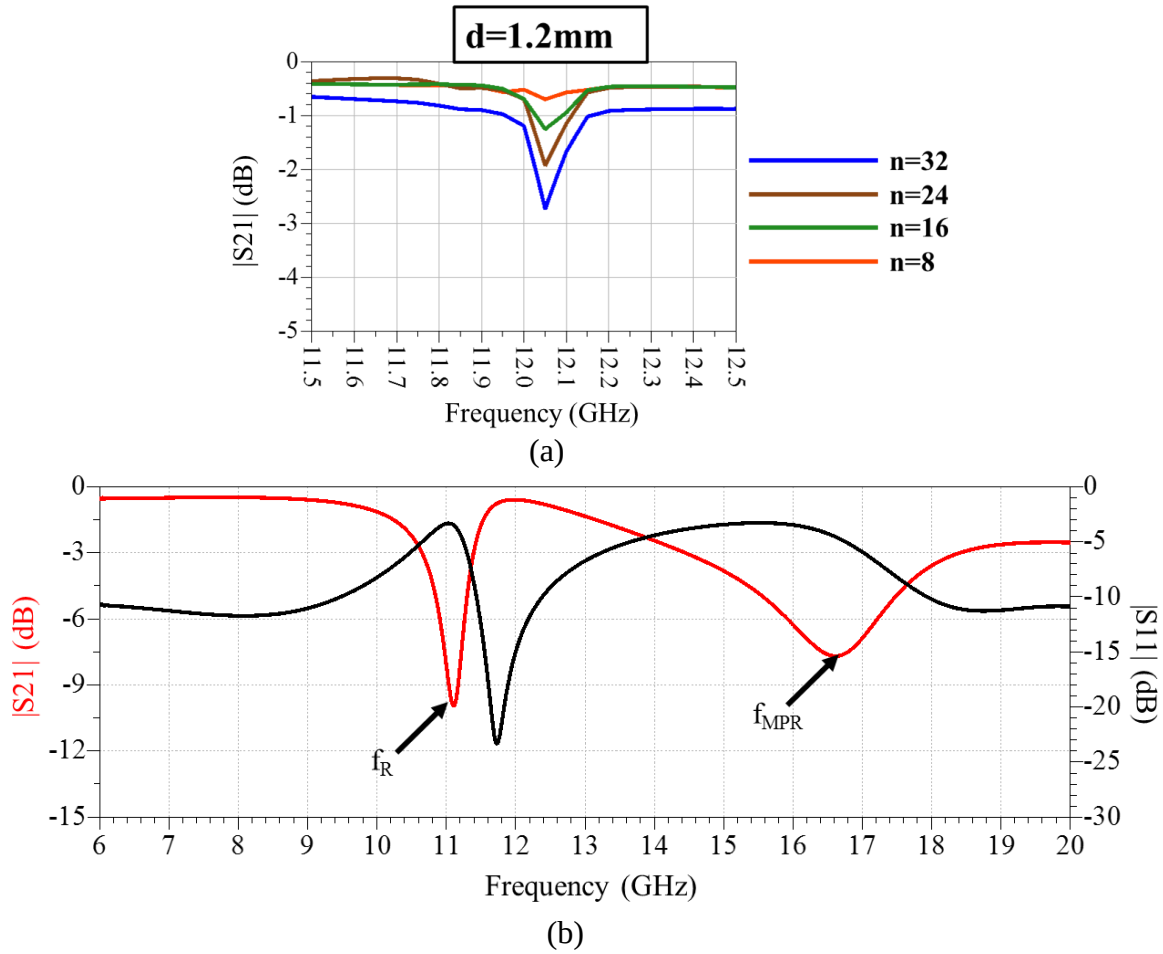

Figure 6.6: (a) Effect of increase in number of resonators on $|S_{21}|$ response of the sensing array; (b) $|S_{21}|$ response of a single resonator of the 24×1 1D sensing array and its corresponding $|S_{11}|$ response.

distance d=1.2mm (as obtained above for an 8x1 array) the effect on the $|S_{21}|$ response can be observed as the number of elements in the array are increased (Figure 6.6 (a)). The increase in the number of resonators increases the coupling between them and the read-out microstrip line. Hence for the same de-coupling distance an array with higher number of elements will exhibit the resonant frequency in the $|S_{21}|$ response even when there is no metallized plate present between them. The distance (d) between the resonators and the read-out line needs to be increased to de-couple them but that leads to a bigger pixel size. The increased separation distance would also need a longer metallized plate for coupling. Care needed to be taken to ensure that the self-

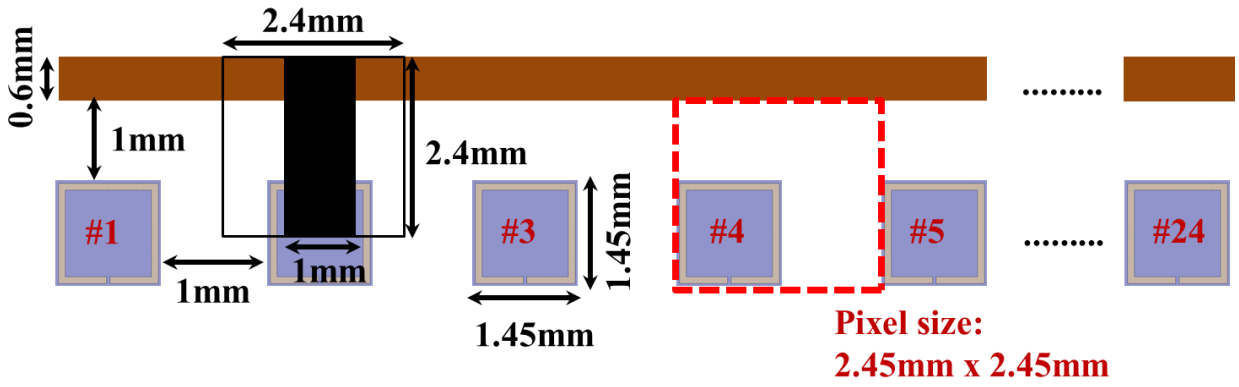

Figure 6.7: Final dimensions of the 1D 24×1 imaging array

resonance frequency of the metallized plate (as it acts as an open circuited stub) did not appear in the frequency band of interest (6-12GHz). In the present design to keep the pixel size small as well as prevent appearance of the self-resonance frequency of the metallized plate, the number of elements in the sensing array were chosen to be 24 from the above parametric studies. Figure 6.6(b) shows the overall response of the 24×1 sensing array with the metallized plate. As can be seen, there are two resonance frequencies in the $|S_{21}|$ response, one due to the coupling between the plate and the resonator (f_R) and the other due to self-resonance of the plate (f_{MPR}). The final dimensions of the 24×1 1D imaging array is shown in Fig. 6.7. The pixel size of the array is 2.45mm×2.45mm.

6.3.2 Fabrication

The substrate carrying the microstrip read-out line and the open loop resonators was fabricated using standard photolithography and copper etching techniques. The alignment between the microstrip line on the top surface and the open loop resonators on the ground plane was done by using a backside mask aligner. Both the patterns were defined on the corresponding copper surface of the substrate using lithography and then subsequent copper etching. Benzocyclobutene

(a)

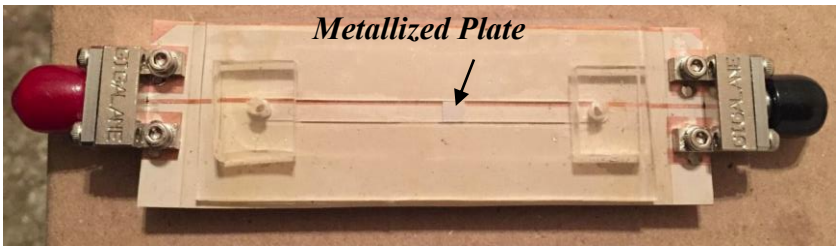

(b)

Figure 6.8: (a) Final fabricated array; (b) Open loop resonator array etched on the ground plane used for sensing the sample

(BCB) was then spun on top of the microstrip lines and cured overnight in a convection oven. The microchannels fabricated using soft-lithography were then bonded to the BCB coated surface of the microstrip lines using APTES and oxygen plasma treatment technique described earlier in Chapter 4. The final fabricated array is shown in Figure 6.8.

6.4 Micropump Control Unit

Accurate control over the movement of the metallized plate inside the microfluidic channel is one of the key cornerstones for successful operation of the imaging system. This is achieved by

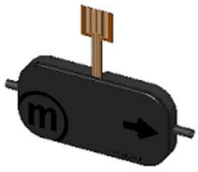

Piezo-electric micro-pumps
Dimensions: 12 x 22x 11mm3
Current consumption: 40mA@3.3V

(a)

(b)

Figure 6.9: (a) Piezo-electric micropump; (b) On chip driver (mp6) for the micropump.

the use of electronically controlled piezo-electric micropumps obtained from Bartels Mikrotechnik (Model: mp6) (Figure 6.9(a)). The operation of the micropumps was controlled through the use of

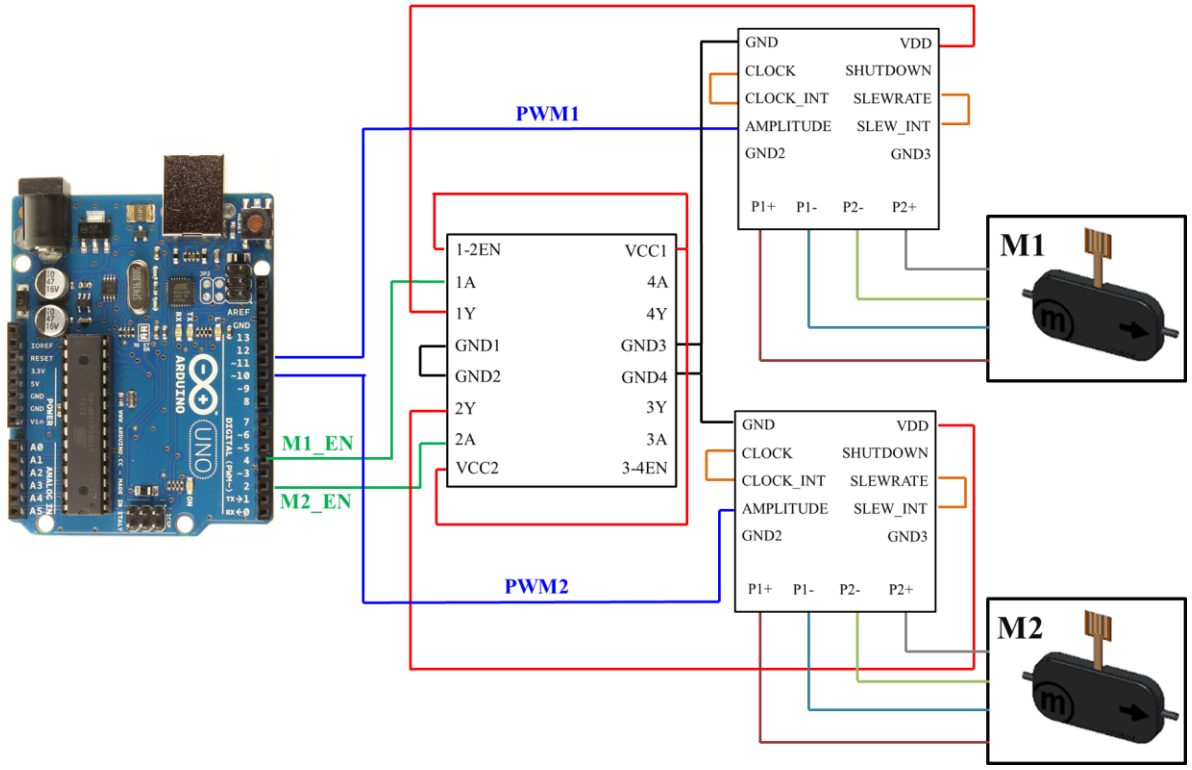

Figure 6.10: Control circuit diagram for controlling the micropumps using a microcontroller.

on-chip driver circuits (mp6-OEM) (Figure 6.9(b)) which generate the alternating voltage signal needed to operate the pumps. In order to obtain bi-directional movement of the metallized plate inside the microchannel, two mp6 micropumps were inter-connected. The control signals for operating the micropumps were generated using an Arduino Uno microcontroller board. The signals were used to switch power between the micropumps as well as control the speed of the metallized plate movement. In order to prevent the microcontroller board from being overloaded by the current drawn by the micropumps a L293D driver circuit was used to power the micropumps. The circuit layout used for interfacing the mp6-OEM driver with the Arduino Uno is shown in Figure 6.10. The power signal from the controller was used to switch the appropriate micropump depending on the desired movement of the metallized plate i.e., either forward or backward inside the microchannel. This signal was supplied to the L293D driver which in turn

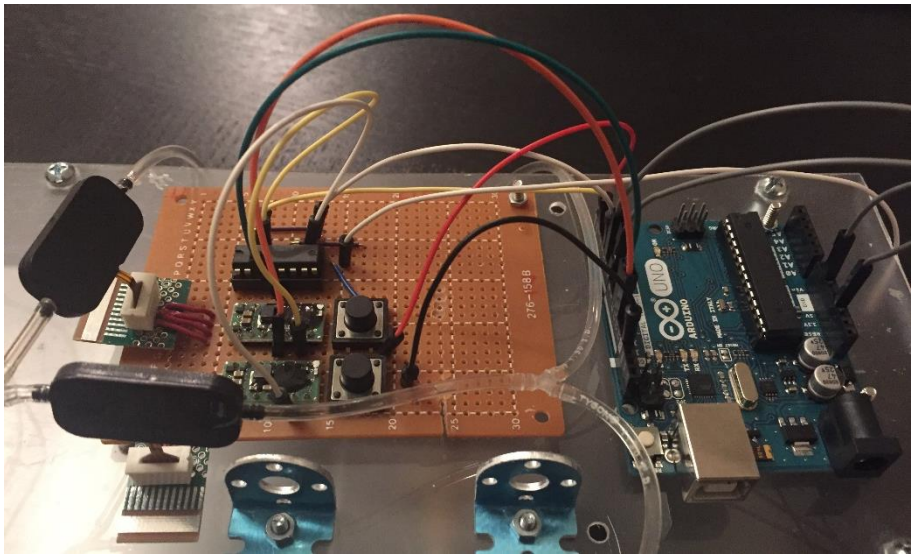

Figure 6.11: Micropump control unit.

supplied the power to the selected micropump. The amplitude signal was used to control the speed of the metallized plate. It was generated using the pulse width modulation (PWM) output pin from the Arduino Uno. By selecting appropriate duty cycle of the PWM signal, the average voltage supplied to the mp6-OEM driver circuit was varied. The higher the duty cycle of the pulse, the faster the movement of the plate. Several duty cycle values were experimented with emphasis on fine control of the plate movement. The value of 55 was observed to provide the best control over the movement of the plate. For the current design the clock signal of the mp6-OEM driver circuit was hardwired to 100Hz. Different clock cycles were experimented with and 100Hz was found to be the value for which maximum speed was observed. The hardwiring was done by connecting the clock input of the driver to the clock INT pin. The assembled micropump control unit is shown in Figure 6.11.

6.5 Stepper Motor Controlled Stage

The metallized plate moving inside the microchannel is used to scan the sample in the x-direction. For scanning in the y-direction, the sample to be imaged is mounted on a stepper motor

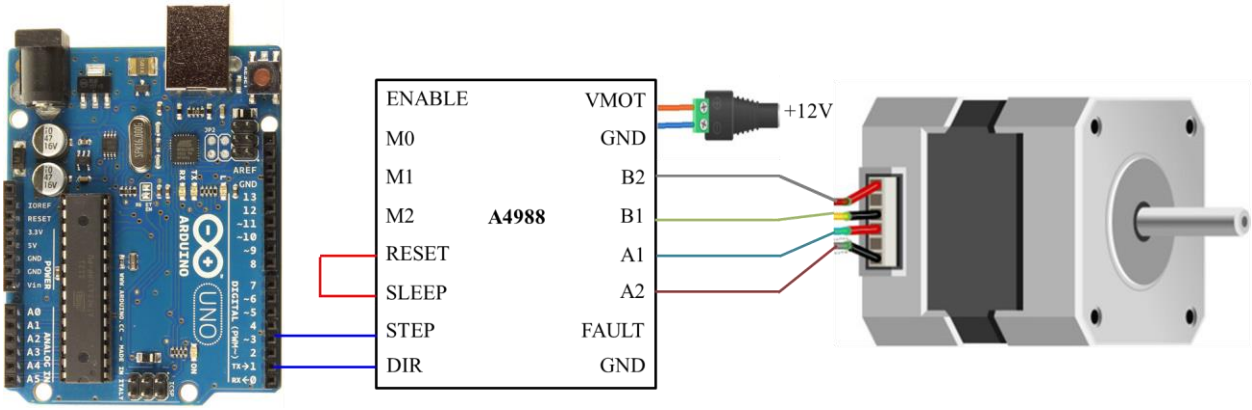

Figure 6.12: Stepper motor interface for controlling sample stage movement.

controlled stage. The Arduino Uno microcontroller was used to send control signals to a A4988 driver circuit that generates all the synchronization signals needed to turn the stepper motor (Figure 6.12). The stepper motor used is a bipolar motor with a lead screw mounted to its shaft. The sample stage is fixed to the shaft using a travelling nut. The nut with the mounted sample stage moves linearly with every rotation of the motor. The control signals from the microcontroller set the

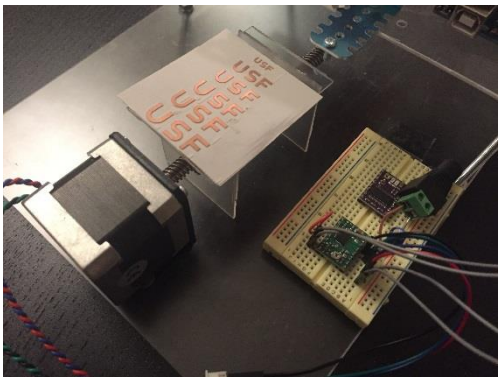

Figure 6.13: Assembled stepper motor controlled sample stage.

direction and movement of the sample stage. The resolution of the linear movement of the sample stage is set by the number of steps of the motor. Experimental studies performed to determine the number of steps needed to obtain a linear resolution of 2.45mm (determined from the pixel size) concluded number of steps to be 61. The assembled stepper motor controlled sample stage is shown in Figure 6.13. This stage enables scanning the sample in the y-direction.

6.6 Computer Interface Using LabVIEW

The individual components of the imaging system mentioned above i.e., the 1D sensor array, micropump control unit, stepper motor controlled stage were integrated and controlled using a computer interface built in LabVIEW (Figure 6.14). The in-built functions of LabVIEW Interface

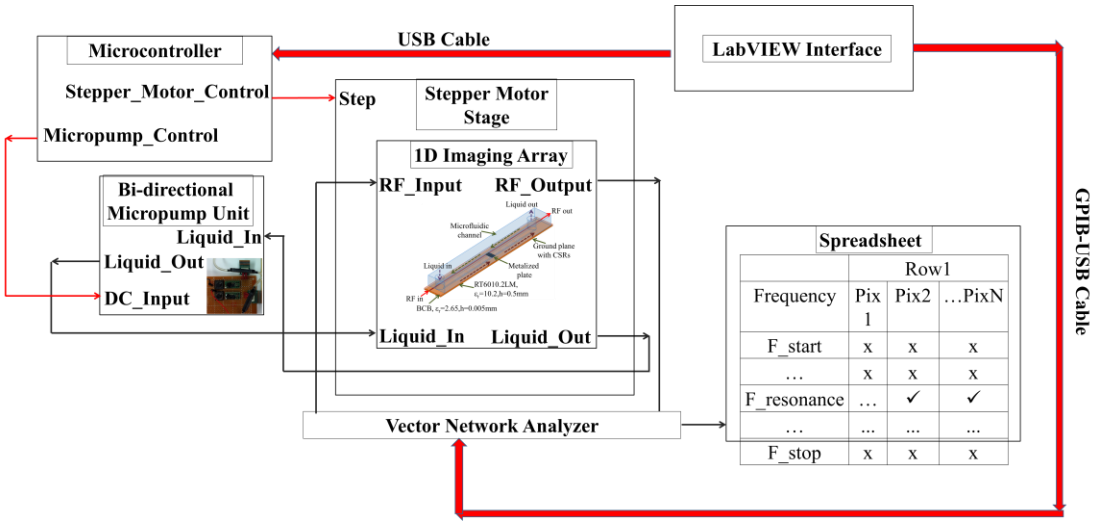

Figure 6.14: Block diagram of the imaging system interfaced with LabVIEW.

for Arduino (LIFA) library were used to build and set-up the control system of the Arduino Uno microcontroller. As discussed in the previous sections, the microcontroller was interfaced with the micropump unit to control the scanning in the x-direction (using the microfluidically controlled metallized plate) while the stepper motor stage controlled using the microcontroller was used to control the scanning in the y-direction (moving the sample stage mounted on the lead screw of the stepper motor). The LabVIEW interface controls the microcontroller which in turn sends control signals to the micropumps and the stepper motor. Each time the S_{21} response of the sensor array is to be recorded, the GPIB-USB interface between the VNA and LabVIEW is used to save the data in a file on the computer.

The interface is described in detail in Figure 6.15. In the interface the on time and duty cycle for the micropumps is defined which determines the movement of the metallized plate,

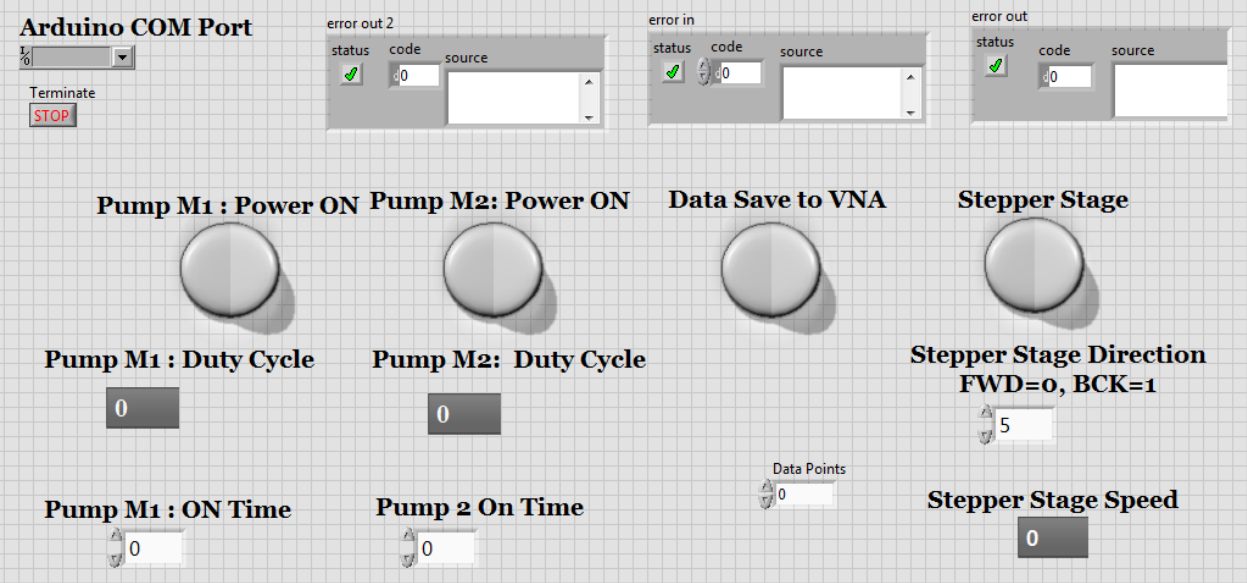

Figure 6.15: LabVIEW interface for the imaging system.

thereby the resolution of the scanning in the x-direction. The stepper stage speed input defines the movement of the sample stage in the y-direction, thereby the resolution of the scanning in the y-direction. When the program is executed, it scans the sample in the x-direction using the metallized plate and saves the corresponding S_{21} response of the 1D sensor array from the vector network analyzer (VNA). Once the plate reaches the end of the sensor array (24th element), the stepper motor drives the sample stage by one step (2.45mm) in the y-direction. The sample is scanned in the x-direction again using the metallized plate but in the reverse direction as compared to the previous scan. This process is repeated till the entire sample is scanned.

6.7 Experimental Verification

The final assembled system is shown is Figure 6.16. To demonstrate the imaging capability of the assembled system, a test sample was developed with a metallized pattern etched on its surface. The motivation behind using such a sample was to simplify the post-processing of the collected data while still demonstrating the imaging procedure. When one of the resonators in the 1D sensor array is loaded with a metal patch it exhibits a flat S_{21} response. The reason being

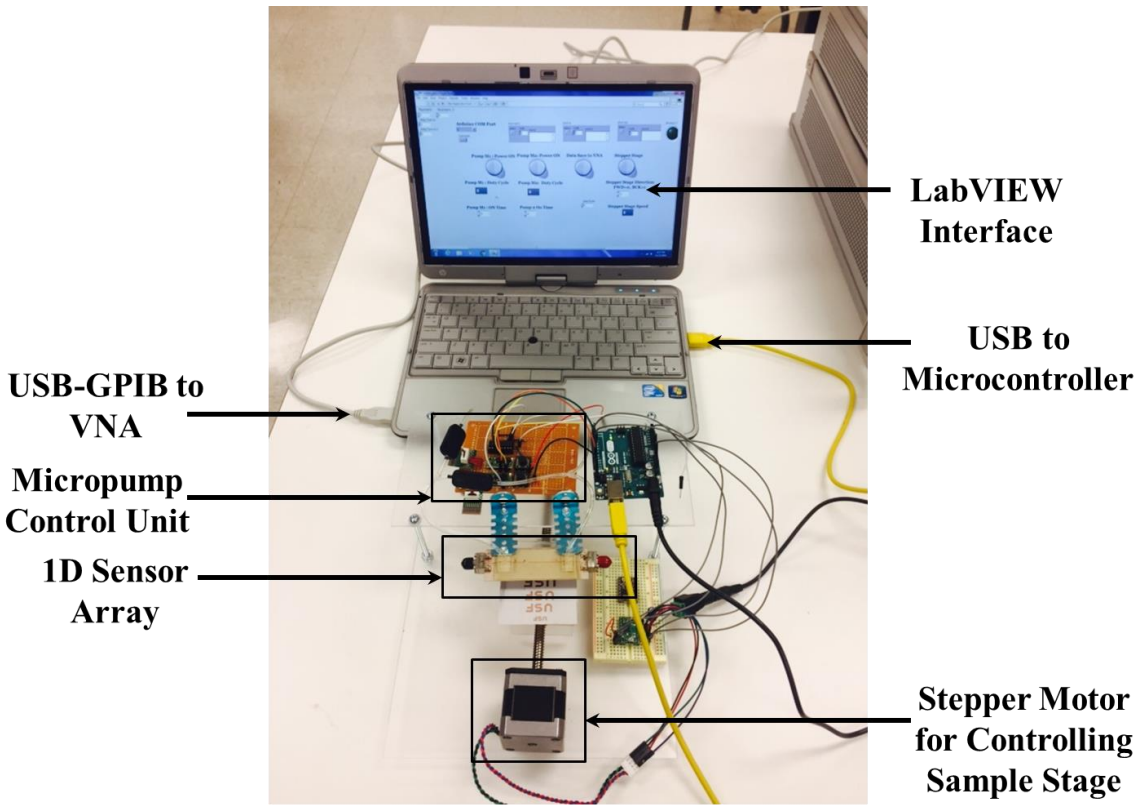

Figure. 6.16: Assembled imaging system.

that the resonator gets shorted by the overlying metal which in turn can be used to develop a binary image of the sample. This simplifies the need of post-processing the collected data.

The metallized pattern of the sample is shown in Figure 6.17(a). The sample was designed to fit within the 24×24 pixel scanning area of the imaging system. The size of a pixel is 2.45mm× 2.45mm. The grid of the 24×24 pixels is overlaid on top of the fabricated sample to help in correlating with the imaged result shown later in the chapter. As discussed in the previous section, when the resonator is loaded with a metal patch it exhibits a flat S_{21} response. It was observed that the same behavior is exhibited by the resonator even in cases of partial overlapping with a metal patch. For the all cases shown in the Figure 6.18, the resonator when interrogated by the metallized plate does not show any resonance in its S_{21} response. All these cases are read as '1' meaning metal is present on top of the resonator while a '0' is read when the resonance is present.

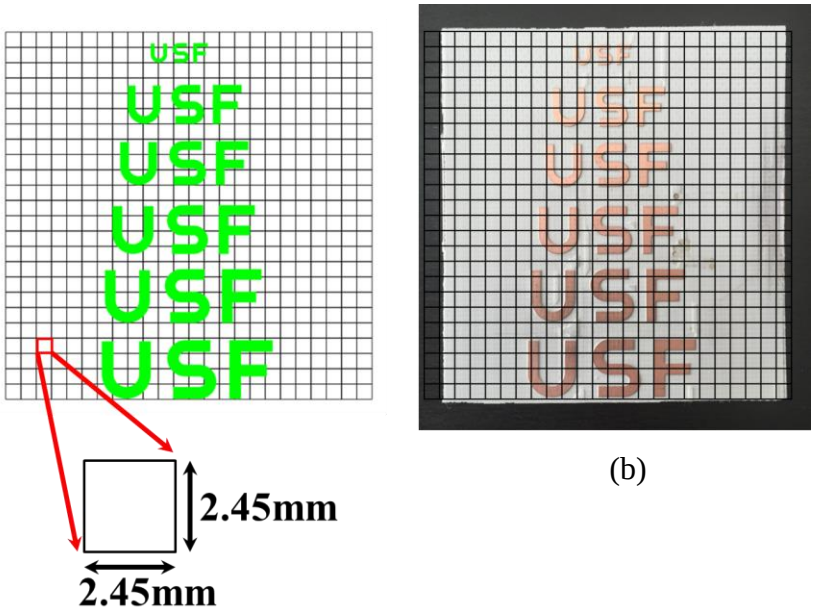

(a) (b)

Figure 6.17: (a) Pattern of the sample to be imaged; (b) Fabricated sample on Rogers 4003 substrate.

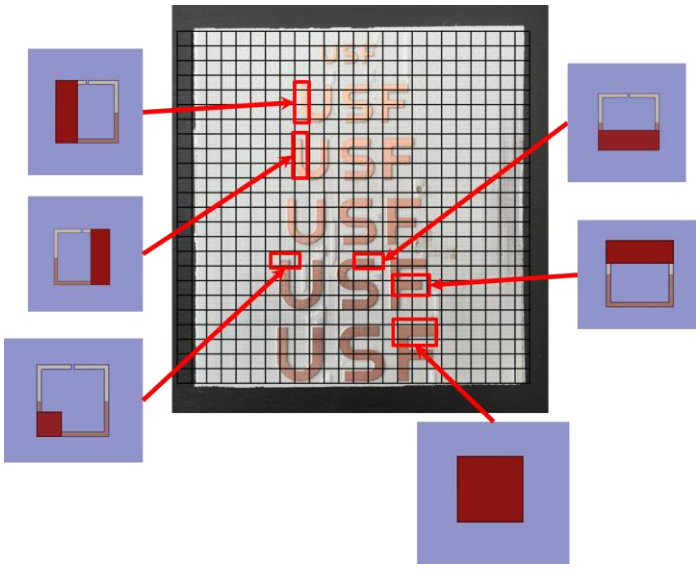

Figure 6.18: Demonstrating the test cases of metal overlap with the resonators.

The binary image generated by the system is shown in Figure 6.19(b). The different size of the letters etched on the sample were used as different test cases. These cases help in

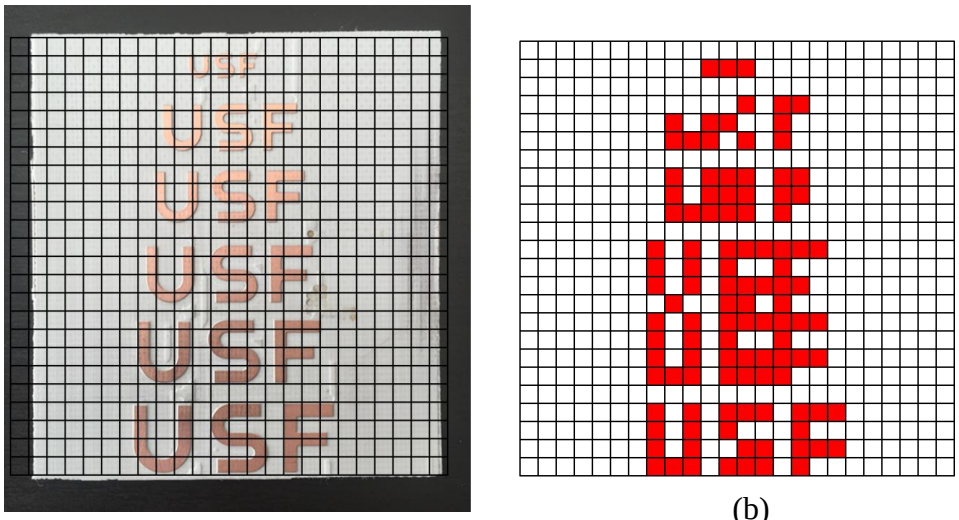

(a) (b)

Figure 6.19: (a) Pattern of the sample to be imaged; (b) Imaged data.

understanding the imaging resolution of the current system. As can be seen from the imaged data, for many of the test cases the imaged data does not resemble the etched metal pattern. For example, when the metal pattern is smaller than the pixel itself, the system is not able to distinguish between the different letters. The last case on the test sample is the one which the system was able to distinguish as separate distinct letters. This experiment thus demonstrates the imaging resolution of the present system.

6.8 Conclusion

In this chapter a microfluidically controlled imaging system is presented. The 1D array of complimentary open loop resonators is interrogated with a microfluidically controlled metallized plate. A stepper motor driven sample stage is incorporated under the sensor array for extending 2D imaging capability to the system. The system is also interfaced with a computer to provide automated control over the movement of the plate, the stepper motor controlled stage and saving the data from the VNA. The imaging capability is demonstrated by scanning a test sample with a metal pattern etched on its surface. The prospects of such an imaging system towards dielectric imaging is discussed in the next chapter.

CHAPTER 7: CONCLUSION

7.1 Summary

The ever-increasing demand for multifunctional wireless communication systems has generated a lot of interest towards developing frequency reconfigurable antennas. These antennas offer the advantage of dynamically adjusting their resonating frequency over fixed operation ones. To alleviate the drawbacks of conventional reconfiguration techniques, in this dissertation microfluidics based reconfiguration was proposed as an alternative technique. The advantages of microfluidic reconfiguration were then demonstrated through the design and experimental verification of frequency tunable monopole and dipole antennas as summarized below.

A wideband frequency tunable liquid metal monopole antenna was demonstrated. The liquid metal monopole was shown to have a 4:1 tuning range. The antenna was measured to have a tuning speed of 250MHz/s and exhibited stable radiation pattern over the entire tuning range. This technique of microfluidically manipulating liquid metal slugs inside microchannels was further implemented to develop a 2:1 frequency tunable high gain antenna array. The 4 × 1 antenna array demonstrated >6dB broadside gain and tuning speed of 125MHz/s. The reliability of the liquid metal monopole antenna was improved by resorting to using metallized plate as the radiating element. The antenna was shown to exhibit similar wide tuning range, stable gain and radiation pattern over the tuning range. An experimental set-up was developed to verify the high-power handling capability of the microfluidically reconfigured monopole. The antenna demonstrated stable operation for up to 15W of RF input power.

Different from the above mentioned approach wherein the microfluidic load was used as the main radiating element, a frequency tunable dipole antenna was developed using microfluidic loads (selectively metallized plate) as RF switches. The selectively metallized plate acts as the shorting switch and changes the current path on the antenna geometry to tune its resonance frequency. A bonding procedure was developed to bond the microfluidic channel to a thin layer of low loss dielectric. This enabled proximity between the antenna trace and the metallized plate leading to a high level of RF coupling which was required to short out the radiating slots. The antenna showed a measured tunability of 0.88 GHz to 1.39 GHz. The concept was then applied to develop a frequency tunable textile antenna intended for body worn applications.

To further demonstrate the advantage of microfluidics based reconfigurability, a surface imaging system was presented. A microfluidically controlled metallized plate was used as a RF shorting switch to develop a convenient read-out mechanism for interrogating a high resolution planar array of sub-wavelength resonators. The read-out of the array was carried out using a single bi-directional micropump unit. To achieve 2D imaging capability, a stepper motor controlled sample stage was placed under the resonator array. All the components of the system were assembled on a single board. For the sake of experimental demonstration, the vector network analyzer (VNA) was used as the signal source and detector. Computer interface for controlling all the components of the system was build using LabVIEW. An image of a test sample with metal pattern etched on its surface was imaged using the system. The extracted image showed good correlation to the fabricated sample. This work demonstrated low-cost realization of a microwave imaging system which can be extended to develop large format high resolution imaging arrays. There are still certain aspects which need to be explored and have been summarized in the next section.

7.2 Future Work

7.2.1 Improvement in 2D Imaging Technique

The imaging system presented in this dissertation involved using a stepper motor controlled stage to achieve 2D imaging capability. Although this is a convenient way of controlling the imaging resolution in the y-dimension, the bulky stepper motor increases the power consumption and increases the overall footprint of the system. An alternative technique for achieving 2D imaging is shown in Figure 7.1. The read-out of the array can be performed with a single bi-directional micropump unit. The S21 measurements of each line can be carried out sequentially (using SP2T switch per line) or simultaneously (using individual S21 measurement circuitry per line). This arrangement eliminates the requirement of the stepper motor stage at the cost of more RF components such as switches.

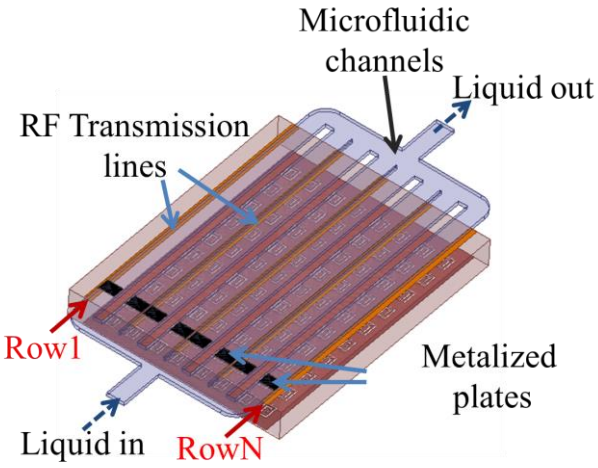

Figure 7.1: 2D microwave imaging system consisting of microfluidically loaded transmission line based read-out circuitries.

7.2.2 Dielectric Imaging

A major goal of the future work would be to employ the system for dielectric imaging. The current system is capable of imaging dielectrics with dielectric constant as high as 50. To demonstrate the concept through a preliminary study, an 8 × 8 array of resonators was modeled in

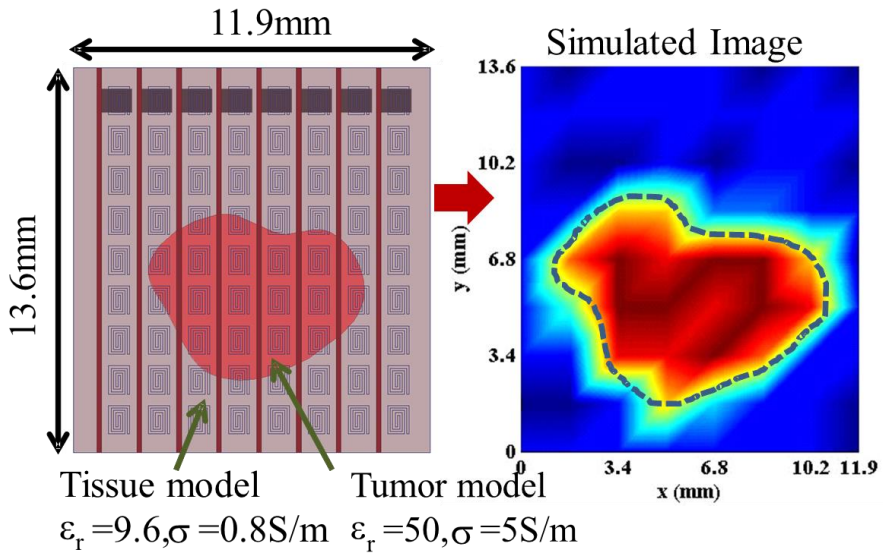

Figure 7.2: Example of a 2D image extracted from simulated S_{21} readings as the metallized plate slides over the resonators placed over the tissue sample.

close proximity of a breast tissue slice (ε_r=9.6, σ=0.8S/m) [97, 98] having a tumorous (ε_r=9.6, σ=0.8S/m) [97, 98] inclusion. The array and tissue size were chosen to keep the numerical simulations less time consuming. As shown in Figure 7.2, the image extracted from simulated S_{21} readings (as the metallized plate slides over the resonators) could resolve the tumor inclusion. A major goal of the future work will be to experimentally verify dielectric imaging using the system.

7.2.3 Standalone Imaging System

In the design procedure of the imaging system it was mentioned that the operating frequency range of the system was chosen to be 6-12GHz. The reason for choosing this range was to incorporate a voltage controlled oscillator (VCO) as the RF source of the imaging system. By using an RF detector at the other end of the microstrip line, the motivation was to replace the bulky VNA being used to perform the measurements in the current set-up. This would lead to the imaging system working as a standalone system. A concept figure of the standalone system is shown in Figure 7.3.

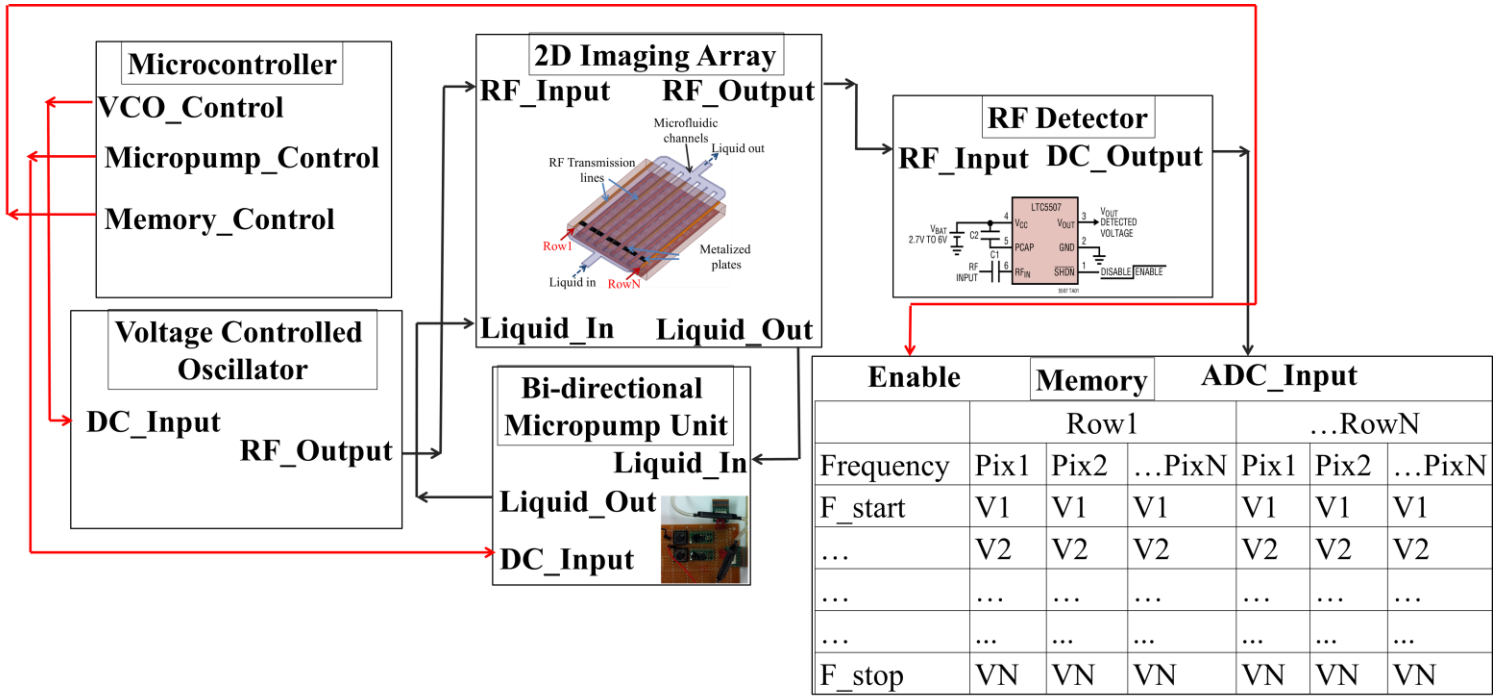

Figure 7.3: Concept block diagram of the envisioned 2D microwave imaging system.

REFERENCES

[1] G. Srinivasan, A. S. Tatarenko, and M. I. Bichurin, "Electrically tunable microwave filters based on ferromagnetic resonance in ferrite-ferroelectric bilayers," Electronics Letters, vol. 41, pp. 596-598, 2005.

[2] G. Subramanyam, F. A. Miranda, R. R. Romanofsky, F. W. Van Keuls, C. L. Canedy, S. Aggarval, et al., "A ferroelectric tunable microstrip Lange coupler for K-band applications," in Microwave Symposium Digest. 2000 IEEE MTT-S International, 2000, pp. 1363-1366 vol.3.

[3] O. G. Vendik, "Ferroelectric films in microwave technique: physics, characterization, and tunable devices," in Physics and Engineering of Microwaves, Millimeter, and Submillimeter Waves, 2004. MSMW 04. The Fifth International Kharkov Symposium on, 2004, pp. 66-71 Vol.1.

[4] N. Behdad and K. Sarabandi, "Dual-band reconfigurable antenna with a very wide tunability range," Antennas and Propagation, IEEE Transactions on, vol. 54, pp. 409-416, 2006.

[5] D. Cure, T. M. Weller, T. Price, F. A. Miranda, and F. W. Van Keuls, "Low-Profile Tunable Dipole Antenna Using Barium Strontium Titanate Varactors," Antennas and Propagation, IEEE Transactions on, vol. 62, pp. 1185-1193, 2014.

[6] S. Nikolaou, R. Bairavasubramanian, C. Lugo, I. Carrasquillo, D. Thompson, G. E. Ponchak, et al., "Pattern and frequency reconfigurable annular slot antenna using PIN diodes," Antennas and Propagation, IEEE Transactions on, vol. 54, pp. 439-448, 2006.

[7] D. Peroulis, K. Sarabandi, and L. P. B. Katehi, "Design of reconfigurable slot antennas," Antennas and Propagation, IEEE Transactions on, vol. 53, pp. 645-654, 2005.

[8] A. F. Sheta and S. F. Mahmoud, "A Widely Tunable Compact Patch Antenna," Antennas and Wireless Propagation Letters, IEEE, vol. 7, pp. 40-42, 2008.

[9] O. Y. Buslov, A. A. Golovkov, V. N. Keis, A. B. Kozyrev, S. V. Krasilnikov, T. B. Samoilova, et al., "Active Integrated Antenna Based on Planar Dielectric Resonator with Tuning Ferroelectric Varactor," Microwave Theory and Techniques, IEEE Transactions on, vol. 55, pp. 2951-2956, 2007.

[10] L. Hsiao-Yun, C. Hai-Ping, C. Shiu-Cheng, T. Chun-Han, and F. Jia-Shiang, “A tunable slot loop antenna using interdigitated ferroelectric varactors,” in Antennas and Propagation Society International Symposium (APSURSI), 2012 IEEE, 2012, pp. 1-2.

[11] X. Wang, P. Bao, T. J. Jackson, and M. J. Lancaster, “Tunable microwave filters based on discrete ferroelectric and semiconductor varactors,” Microwaves, Antennas & Propagation, IET, vol. 5, pp. 776-782, 2011.

[12] M. Sazegar, Z. Yuliang, C. Kohler, H. Maune, M. Nikfalazar, J. R. Binder, et al., “Beam Steering Transmitarray Using Tunable Frequency Selective Surface with Integrated Ferroelectric Varactors,” Antennas and Propagation, IEEE Transactions on, vol. 60, pp. 5690-5699, 2012.

[13] G. Besoli and F. De Flaviis, “A Multifunctional Reconfigurable Pixeled Antenna Using MEMS Technology on Printed Circuit Board,” Antennas and Propagation, IEEE Transactions on, vol. 59, pp.4413-4424, 2011.

[14] E. Erdil, K. Topalli, M. Unlu, O. A. Civi, and T. Akin, “Frequency Tunable Microstrip Patch Antenna Using RF MEMS Technology,” Antennas and Propagation, IEEE Transactions on, vol. 55, pp. 1193-1196, 2007.

[15] W. Guoan, T. Polley, A. Hunt, and J. Papapolymerou, “A high performance tunable RF MEMS switch using barium strontium titanate (BST) dielectrics for reconfigurable antennas and phased arrays,” Antennas and Wireless Propagation Letters, IEEE, vol. 4, pp. 217-220, 2005.

[16] K. M. J. Ho and G. M. Rebeiz, “A 0.9–1.5 GHz Microstrip Antenna with Full Polarization Diversity and Frequency Agility,” Antennas and Propagation, IEEE Transactions on, vol. 62, pp. 2398-2406, 2014.

[17] Y. Koga, T. Yamagajo, and M. Shimizu, "Frequency tunable antenna design technique with MEMS switches for mobile phone," in Microwave Conference Proceedings (APMC), 2011 Asia-Pacific, 2011, pp. 441-444.

[18] M. Nishigaki, T. Nagano, T. Miyazaki, T. Kawakubo, K. Itaya, M. Nishio, et al., "Piezoelectric MEMS Variable Capacitor for a UHF Band Tunable Built-in Antenna," in Microwave Symposium, 2007 IEEE/MTT-S International, 2007, pp. 2079-2082.

[19] P. Ramachandran, P. Annamaa, R. Gaddi, P. Tornatta, L. Morrell, and C. Schepens, "Reconfigurable small antenna for mobile phone using MEMS tunable capacitor," in Antennas and Propagation Conference (LAPC), 2013 Loughborough, 2013, pp. 354-357.

[20] M. Kubo, L. Xiaofeng, K. Choongik, M. Hashimoto, B. J. Wiley, H. Donhee, et al., "Stretchable microfluidic electric circuit applied for radio frequency antenna," in Electronic Components and Technology Conference (ECTC), 2011 IEEE 61st, 2011, pp. 1582-1587.

[21] G. J. Hayes, S. Ju-Hee, A. Qusba, M. D. Dickey, and G. Lazzi, "Flexible Liquid Metal Alloy (EGaIn) Microstrip Patch Antenna," Antennas and Propagation, IEEE Transactions on, vol. 60, pp. 2151-2156, 2012.

[22] S. Jalali Mazlouman, J. Xing Jie, A. Mahanfar, C. Menon, and R. G. Vaughan, "A Reconfigurable Patch Antenna Using Liquid Metal Embedded in a Silicone Substrate," Antennas and Propagation, IEEE Transactions on, vol. 59, pp. 4406-4412, 2011.

[23] C. Murray and R. R. Franklin, "Frequency tunable fluidic annular slot antenna," in Antennas and Propagation Society International Symposium (APSURSI), 2013 IEEE, 2013, pp. 386-387.

[24] D. Rodrigo, L. Jofre, and B. A. Cetiner, "Circular Beam-Steering Reconfigurable Antenna with Liquid Metal Parasitics," Antennas and Propagation, IEEE Transactions on, vol. 60, pp. 1796-1802, 2012.

[25] C. K. Y. Kitamura, A. M. Morishita, T. F. Chun, W. G. Tonaki, A. T. Ohta, and W. A. Shiroma, "A liquidmetal reconfigurable Yagi-Uda monopole array," in Microwave Symposium Digest (IMS), 2013 IEEE MTT-S International, 2013, pp. 1-3.

[26] A. Gheethan, J. Myeong Chan, R. Guldiken, and G. Mumcu, "Microfluidic Based Ka-Band Beam-Scanning Focal Plane Array," Antennas and Wireless Propagation Letters, IEEE, vol. 12, pp. 1638-1641, 2013.

[27] J. Fitzgerald, V. P. Wallace, M. Jimenez-Linan, L. Bobrow, R. J. Pye, A. D. Puroshottam, et al., “Terahertz pulsed imaging of human breast tumors,” Radiology, vol. 239, pp. 533-540, May 2006.

[28] Z. D. Taylor, R. S. Singh, M. O. Culijat, J. Y. Suen, W. S. Grundfest, H. Lee, et al., “Reflective terahertz imaging of porcine skin burns,” Optics Letters, vol. 33, pp. 1258-1260, Jun 1 2008.

[29] Hellicar, Andrew, Li Li, and Kieran Greene. "Design and implementation of a THz imaging system, "Proceedings of the 10th Australian symposium on antennas, Sydney. 2007.

[30] Clark, Stuart, et al. "A real-time wide field of view passive millimeter-wave imaging camera." Applied Imagery Pattern Recognition Workshop, 2003. Proceedings. 32nd. IEEE, 2003.

[31] Semenov, A.D.; Richter, H.; Hubers, H.-W.; Gunther, B.; Smirnov, A.; Il'in, K.S.; Siegel, M.; Karamarkovic, J.P., "Terahertz Performance of Integrated Lens Antennas with a Hot-Electron Bolometer," Microwave Theory and Techniques, IEEE Transactions on, vol.55, no.2, pp.239,247, Feb. 2007.

[32] Su, N.; Rajavel, R.; Deelman, P.; Schulman, J.N.; Fay, P., "Sb-Heterostructure Millimeter-Wave Detectors with Reduced Capacitance and Noise Equivalent Power," Electron Device Letters, IEEE, vol.29, no.6, pp.536,539, June 2008.

[33] Abdel-Rahman, M.R.; Gonzalez, F.J.; Boreman, G.D., "Antenna-coupled metal-oxide-metal diodes for dual-band detection at 92.5 GHz and 28 THz," Electronics Letters, vol.40, no.2, pp.116,118, 22 Jan. 2004.

[34] Trichopoulos, G.C.; Mumcu, G.; Sertel, K.; Mosbacker, H.L.; Smith, P., "A Novel Approach for Improving Off-Axis Pixel Performance of Terahertz Focal Plane Arrays," Microwave Theory and Techniques, IEEE Transactions on, vol.58, no.7, pp.2014,2021, July 2010.

[35] A. Zohur, H. Mopidevi, D. Rodrigo, M. Unlu, L. Jofre and B. A. Cetiner, "RF MEMS Reconfigurable Two-Band Antenna," in IEEE Antennas and Wireless Propagation Letters, vol. 12, no., pp. 72-75, 2013.

[36] K. Van Caekenberghe and K. Sarabandi, "A 2-Bit Ka-Band RF MEMS Frequency Tunable Slot Antenna," in IEEE Antennas and Wireless Propagation Letters, vol. 7, no. , pp. 179-182, 2008.

[37] K. Topalli, E. Erdil, O. A. Civi, S. Demir, S. Koc, and T. Akin, "Tunable dual-frequency RF MEMS rectangular slot ring antenna," Sensors and Actuators A, vol. 156, no. 2, pp. 373–380, 2009.

[38] K. R. Boyle and P. G. Steeneken, "A five-band reconfigurable PIFA for mobile phones," IEEE Transactions on Antennas and Propagation, vol. 55, no. 11, pp. 3300–3309, 2007.

[39] D. Rodrigo and L. Jofre, "Frequency and Radiation Pattern Reconfigurability of a Multi-Size Pixel Antenna," in IEEE Transactions on Antennas and Propagation, vol. 60, no. 5, pp. 2219-2225, May 2012.

[40] A. Grau Besoli and F. De Flaviis, "A Multifunctional Reconfigurable Pixeled Antenna Using MEMS Technology on Printed Circuit Board," in IEEE Transactions on Antennas and Propagation, vol. 59, no. 12, pp. 4413-4424, Dec. 2011.

[41] D. Rodrigo, B. A. Cetiner and L. Jofre, "Frequency, Radiation Pattern and Polarization Reconfigurable Antenna Using a Parasitic Pixel Layer," in IEEE Transactions on Antennas and Propagation, vol. 62, no. 6, pp. 3422-3427, June 2014.

[42] D. Peroulis, K. Sarabandi and L. P. B. Katehi, "Design of reconfigurable slot antennas," in IEEE Transactions on Antennas and Propagation, vol. 53, no. 2, pp. 645-654, Feb. 2005.

[43] M. Komulainen, M. Berg, H. Jantunen, E. T. Salonen and C. Free, "A Frequency Tuning Method for a Planar Inverted-F Antenna," in IEEE Transactions on Antennas and Propagation, vol. 56, no. 4, pp. 944-950, April 2008.

[44] M. Borhani, P. Rezaei and A. Valizade, "Design of a Reconfigurable Miniaturized Microstrip Antenna for Switchable Multiband Systems," in IEEE Antennas and Wireless Propagation Letters, vol. 15, no. , pp. 822-825, 2016.

[45] M. Soltanpour and M. M. Fakharian, "Compact filtering slot antenna with frequency agility for Wi-Fi/LTE mobile applications," in Electronics Letters, vol. 52, no. 7, pp. 491-492, 4 1 2016.

[46] M. M. Fakharian, P. Rezaei, A. A. Orouji and M. Soltanpur, "A Wideband and Reconfigurable Filtering Slot Antenna," in IEEE Antennas and Wireless Propagation Letters, vol. 15, no. , pp. 1610-1613, 2016.

[47] A. S. Al-Zayed, M. A. Kourah and S. F. Mahmoud, "Frequency-reconfigurable single- and dual-band designs of a multi-mode microstrip antenna," in IET Microwaves, Antennas & Propagation, vol. 8, no. 13, pp. 1105-1112, October 21 2014.

[48] H. Y. Li, C. T. Yeh, J. J. Huang, C. W. Chang, C. T. Yu and J. S. Fu, "CPW-Fed Frequency-Reconfigurable Slot-Loop Antenna With a Tunable Matching Network Based on Ferroelectric Varactors," in IEEE Antennas and Wireless Propagation Letters, vol. 14, no., pp. 614-617, 2015.

[49] N. Nguyen-Trong, L. Hall and C. Fumeaux, "A Frequency- and Polarization-Reconfigurable Stub-Loaded Microstrip Patch Antenna," in IEEE Transactions on Antennas and Propagation, vol. 63, no. 11, pp. 5235-5240, Nov. 2015.

[50] C. Hung and T. Chiu, "Dual-Band Reconfigurable Antenna Design Using Slot-Line With Branch Edge," in IEEE Transactions on Antennas and Propagation, vol. 63, no. 2, pp. 508-516, Feb. 2015.

[51] A. Boukarkar, X. Q. Lin and Y. Jiang, "A Dual-Band Frequency-Tunable Magnetic Dipole Antenna for WiMAX/WLAN Applications," in IEEE Antennas and Wireless Propagation Letters, vol. 15, no., pp. 492-495, 2016.

[52] J. Modelski and Y. Yashchyshyn, "Semiconductor and ferroelectric antennas," 2006 Asia-Pacific Microwave Conference, Yokohama, 2006, pp. 1052-1059.

[53] C. Fritzsch, S. Bildik and R. Jakoby, "Ka-band frequency tunable patch antenna," Proceedings of the 2012 IEEE International Symposium on Antennas and Propagation, Chicago, IL, 2012, pp. 1-2.

[54] Pouria Yaghmaee, Onur Hamza Karabey, Bevan Bates, Christophe Fumeaux, and Rolf Jakoby, “Electrically Tuned Microwave Devices Using Liquid Crystal Technology,” International Journal of Antennas and Propagation, vol. 2013, Article ID 824214, 9 pages, 2013.

[55] L. Huitema, T. Reveyrand, J. L. Mattei, E. Arnaud, C. Decroze and T. Monediere, "Frequency Tunable Antenna Using a Magneto-Dielectric Material for DVB-H Application," in IEEE Transactions on Antennas and Propagation, vol. 61, no. 9, pp. 4456-4466, Sept. 2013.

[56] I. T. Nassar, H. Tsang, D. Bardroff, C. P. Lusk and T. M. Weller, "Mechanically Reconfigurable, Dual-Band Slot Dipole Antennas," in IEEE Transactions on Antennas and Propagation, vol. 63, no. 7, pp. 3267-3271, July 2015.

[57] I. T. Nassar, T. M. Weller and C. P. Lusk, "Radiating Shape-Shifting Surface Based on a Planar Hoberman Mechanism," in IEEE Transactions on Antennas and Propagation, vol. 61, no. 5, pp. 2861-2864, May 2013.

[58] R. A. Liyakath, A. Takshi and G. Mumcu, "Multilayer Stretchable Conductors on Polymer Substrates for Conformal and Reconfigurable Antennas," in IEEE Antennas and Wireless Propagation Letters, vol. 12, no., pp. 603-606, 2013.

[59] M. Kelley, C. Koo, H. McQuilken, B. Lawrence, S. Li, A. Han, and G. Huff, "Frequency reconfigurable patch antenna using liquid metal as switching mechanism," Electron. Lett., vol. 49, no. 22, pp. 1370–1371, 2013.

[60] A. J. King, J. F. Patrick, N. R. Sottos, S. R. White, G. H. Huff, and J. T. Bernhard, "Microfluidically switched frequency-reconfigurable slot antennas," IEEE Antennas Wireless Propagat. Lett., vol. 12, pp. 828–831, 2013.

[61] C. Koo, B. LeBlanc, M. Kelley, H. Fitzgerald, G. Huff, and A. Han, "Manipulating liquid metal droplets in microfluidic channels with minimized skin residues toward tunable RF applications," J. Microelectromech. Syst., vol. 24, no. 4, pp. 1069–1076, 2015.

[62] A. Pourghorban Saghati, J. Batra, J. Kameoka, and K. Entesari, "A microfluidically-switched CPW folded slot antenna," in Proc. IEEE APS-URSI, July 2014, pp. 557–558.

[63] A. Pourghorban Saghati, J. Batra, J. Kameoka, and K. Entesari, "A microfluidically-tuned dual-band slot antenna," in Proc. IEEE APS-URSI, July 2014, pp. 1244–1245.

[64] C. Murray and R. Franklin, "Frequency tunable fluidic annular slot antenna," in Proc. IEEE APS-URSI, July 2013, pp. 386–387.

[65] C. Murray and R. Franklin, "Independently tunable annular slot antenna resonant frequencies using fluids," IEEE Antennas Wireless Propagat. Lett., vol. 13, pp. 1449–1452, 2014.

[66] A. Pourghorban Saghati, J. Singh Batra, J. Kameoka, and K. Entesari, "Miniature and reconfigurabe CPW folded slot antennas employing liquid-metal capacitive loading," IEEE Trans. Antennas Propagation., vol. 63, no. 9, pp. 3798–3807, Sept. 2015.

[67] A. Pourghorban Saghati, J. Singh Batra, J. Kameoka, and K. Entesari, “A microfluidically-reconfigurable dual-band slot antenna with a frequency coverage ratio of 3:1,” IEEE Antenna Wireless Propagat. Lett., vol. 16, pp. 122–125, 2016.

[68] T. Bhattacharjee, H. Jiang, and N. Behdad, “A fluidically-tunable, dual-band patch antenna with closely-spaced bands of operation,” IEEE Antenna Wireless Propagat. Lett., vol. PP, no. 99, pp. 1–1, 2015.

[69] M. R. Moorefield, R. C. Gough, A. M. Morishita, J. H. Dang, A. T. Ohta and W. A. Shiroma, "Frequency-tunable patch antenna with liquid-metal-actuated loading slot," in Electronics Letters, vol. 52, no. 7, pp. 498-500, 4 1 2016.

[70] M. Wang, C. Trlica, M. R. Khan, M. D. Dickey, and J. J. Adams, “A reconfigurable liquid metal antenna driven by electrochemically controlled capillarity,” J. Appl. Phys., vol. 117, no. 19, 2015.

[71] A. Morishita, C. Kitamura, A. Ohta, and W. Shiroma, “Two-octave tunable liquid-metal monopole antenna,” Electron. Lett., vol. 50, no. 1, pp. 19–20, Jan. 2014.

[72] A. Morishita, C. Kitamura, A. Ohta, and W. Shiroma, “A liquid-metal monopole array with tunable frequency, gain, and beam steering,” IEEE Antennas Wireless Propagat. Lett., vol. 12, pp. 1388–1391, 2013.

[73] M. Wang; M. R. Khan; M. D. Dickey; J. J. Adams, "A Compound Frequency and Polarization Reconfigurable Crossed Dipole Using Multi-Directional Spreading of Liquid Metal," in IEEE Antennas and Wireless Propagation Letters , vol.PP, no.99, pp.1-1.

[74] A. Ha and K. Kim, "Frequency tunable liquid metal planar inverted-F antenna," in Electronics Letters, vol. 52, no. 2, pp. 100-102, 1 21 2016.

[75] S. Jalali Mazlouman, X. J. Jiang, A. Mahanfar, C. Menon, and R. Vaughan, “A reconfigurable patch antenna using liquid metal embedded in a silicone substrate,” IEEE Trans. Antennas Propagat., vol. 59, no. 12, pp. 4406–4412, Dec. 2011.

[76] K. Noda, M. Ohkado, B. K. Nguyen, K. Matsumoto, H. Fujikawa, and I. Shimoyama, “Frequency-tunable microstrip antenna with liquid actuator using gradually widened transmission line,” IEEE Antennas Wireless Propagat. Lett., vol. 14, pp. 551–555, Nov. 2015.

[77] J. H. So, J. Thelen, A. Qusba, G. J. Hayes, G. Lazzi, and M. D. Dickey, “Reversibly deformable and mechanically tunable fluidic antennas,” Adv. Funct. Mater., vol. 19, no. 22, pp. 3632–3637, 2009.

[78] A. Dey, R. Guldiken and G. Mumcu, "Wideband frequency tunable liquid metal monopole antenna," 2013 IEEE Antennas and Propagation Society International Symposium (APSURSI), Orlando, FL, 2013, pp. 392-393.

[79] A. Dey, R. Guldiken and G. Mumcu, "Microfluidically Reconfigured Wideband Frequency-Tunable Liquid-Metal Monopole Antenna," in IEEE Transactions on Antennas and Propagation, vol. 64, no. 6, pp. 2572-2576, June 2016.

[80] Z. N. Chen, T. S. P. See, and X. Qing, “Small printed ultrawideband antenna with reduced ground plane effect,” IEEE Trans. Antennas Propag., vol. 55, no. 2, pp. 383–388, Feb. 2007.

[81] V. Sunkara, D.-K. Park, H. Hwang, R. Chantiwas, S. A. Soper, and Y.-K. Cho, “Simple room temperature bonding of thermoplastics and poly (dimethylsiloxane),” Lab Chip, vol. 11, pp. 962–965, 2011.

[82] A. A. Gheethan, A. Dey and G. Mumcu, "Passive Feed Network Designs for Microfluidic Beam-Scanning Focal Plane Arrays and Their Performance Evaluation," in IEEE Transactions on Antennas and Propagation, vol. 63, no. 8, pp. 3452-3464, Aug. 2015.

[83] Liu, T; Sen, P; & Kim, CJ. (2012). Characterization of nontoxic liquid-metal alloy galinstan for applications in microdevices. Journal of Microelectromechanical Systems, 21(2), 443 – 450.

[84] J. H. Dang, R. C. Gough, A. M. Morishita, A. T. Ohta, and W. A. Shiroma, “Liquid-metal frequency-reconfigurable slot antenna using air-bubble actuation,” IET Electron. Lett., vol. 51, no. 21, pp. 1630–1632, 2015.

[85] A. M. Morishita, J. H. Dang, R. C. Gough, A. T. Ohta, and W. A. Shiroma, “A tunable amplifier using reconfigurable liquid-metal double-stub tuners,” in Proc. Texas Symp. Wireless Microw. Circuits Syst. (WMCS’15), 2015, pp. 1–4.

[86] R. C. Gough, J. H. Dang, A. M. Morishita, A. T. Ohta, and W. A. Shiroma, “Reconfigurable coupled-line bandpass filter with electrically actuated liquid-metal tuning,” in Proc Asia-Pacific Microw. Conf. (APMC’14), 2014, pp. 932–934.

[87] R. C. Gough, J. H. Dang, A. M. Morishita, A. T. Ohta, and W. A. Shiroma, “Frequency-tunable slot antenna using continuous electrowetting of liquid metal,” in Proc. IEEE MTT-S IMS, 2014, pp. 1–4.

[88] A. Dey and G. Mumcu, "Microfluidically Controlled Frequency-Tunable Monopole Antenna for High-Power Applications," in IEEE Antennas and Wireless Propagation Letters, vol. 15, no. , pp. 226-229, 2016.

[89] D. L. Diedhiou, O. de Sagazan, R. Sauleau and A. V. Boriskin, "Contactless Microstrip Transition for Flexible Microfluidic Circuits and Antennas," in IEEE Antennas and Wireless Propagation Letters, vol. 14, no. , pp. 1502-1505, 2015.

[90] Elveflow, “Introduction about soft-lithography and polymer molding for microfluidics,” 2015 [Online]. Available: http://www. elveflow.com/soft-lithography-reviews-and-tutorials/microfluidicdevice-fabrication/introduction-about-soft-lithography-and-polymermolding-for-microfluidic.

[91] T. Palomo, P. Herzig, T. M. Weller, and G. Mumcu, “Wideband bandstop X-band filter using electrically small tightly coupled resonators,” IEEE Microw. Wireless Compon. Lett., vol. 23, pp. 356–358, 2013.

[92] L. Meng and N. Behdad, “Fluidically tunable frequency selective/phase shifting surfaces for high-power microwave applications,” IEEE Trans. Antennas Propag., vol. 60, pp. 2748–2759, 2012.

[93] A. Dey and G. Mumcu, "Small microfluidically tunable top loaded monopole," 2016 International Workshop on Antenna Technology (iWAT), Cocoa Beach, FL, 2016, pp. 148-149.

[94] A. Dey and G. Mumcu, "Microfluidically controlled metalized plate based frequency reconfigurable monopole for high power RF applications," 2015 IEEE International Symposium on Antennas and Propagation & USNC/URSI National Radio Science Meeting, Vancouver, BC, 2015, pp. 2299-2300.

[95] A. Dey and G. Mumcu, "High resolution surface imaging arrays interrogated with microfluidically controlled metalized plates," 2014 IEEE Antennas and Propagation Society International Symposium (APSURSI), Memphis, TN, 2014, pp. 213-214.

[96] A. Mashal, F. Gao, and S. C. Hagness, “Heterogeneous anthropomorphic phantoms with realistic dielectric properties for microwave breast imaging experiments,” Microwave and Optical Technology Letters, vol. 53, no. 8, pp. 1896-1902, August 2011.

[97] Y. Huo, R. Bansal and Q. Zhu, “Modeling of noninvasive microwave characterization of breast tumors,” in IEEE Transactions on Biomedical Engineering, vol. 51, no. 7, pp. 1089-1094, July 2004.

[98] E. C. Fear, X. Li, S. C. Hagnes, and M. A. Stuchly, “Confocal microwave imaging for breast cancer detection: localization of tumors in three dimensions,” Biomedical Engineering, IEEE Transactions on, vol. 49, pp. 812-822, 2002.

[99] G. Mumcu, A. Dey and T. Palomo, "Frequency-Agile Bandpass Filters Using Liquid Metal Tunable Broadside Coupled Split Ring Resonators," in IEEE Microwave and Wireless Components Letters, vol. 23, no. 4, pp. 187-189, April 2013.

[100] A. Dey, A. Kiourti, G. Mumcu and J. L. Volakis, "Microfluidically reconfigured frequency tunable dipole antenna," 2015 9th European Conference on Antennas and Propagation (EuCAP), Lisbon, 2015, pp. 1-2.

APPENDICES

Appendix A Copyright Permissions

The following are Copyright permissions for use of materials in Chapters 3,4,5,6 and 7.

11/17/2016 Rightslink® by Copyright Clearance Center

Copyright Clearance Center RightsLink® Home Create Account Help

IEEE Requesting permission to reuse content from an IEEE publication

Title: Wideband frequency tunable liquid metal monopole antenna

Conference Proceedings: 2013 IEEE Antennas and Propagation Society International Symposium (APSURSI)

Author: Abhishek Dey; Rasim Guldiken; Gokhan Mumcu

Publisher: IEEE

Date: 7-13 July 2013

Copyright © 2013, IEEE

LOGIN

If you're a copyright.com user, you can login to RightsLink using your copyright.com credentials. Already a RightsLink user or want to learn more?

Thesis / Dissertation Reuse

The IEEE does not require individuals working on a thesis to obtain a formal reuse license, however, you may print out this statement to be used as a permission grant:

Requirements to be followed when using any portion (e.g., figure, graph, table, or textual material) of an IEEE copyrighted paper in a thesis:

1) In the case of textual material (e.g., using short quotes or referring to the work within these papers) users must give full credit to the original source (author, paper, publication) followed by the IEEE copyright line © 2011 IEEE.
2) In the case of illustrations or tabular material, we require that the copyright line © [Year of original publication] IEEE appear prominently with each reprinted figure and/or table.
3) If a substantial portion of the original paper is to be used, and if you are not the senior author, also obtain the senior author's approval.

Requirements to be followed when using an entire IEEE copyrighted paper in a thesis:

1) The following IEEE copyright/ credit notice should be placed prominently in the references: © [year of original publication] IEEE. Reprinted, with permission, from [author names, paper title, IEEE publication title, and month/year of publication]
2) Only the accepted version of an IEEE copyrighted paper can be used when posting the paper or your thesis on-line.
3) In placing the thesis on the author's university website, please display the following message in a prominent place on the website: In reference to IEEE copyrighted material which is used with permission in this thesis, the IEEE does not endorse any of [university/educational entity's name goes here]'s products or services. Internal or personal use of this material is permitted. If interested in reprinting/republishing IEEE copyrighted material for advertising or promotional purposes or for creating new collective works for resale or redistribution, please go to http://www.ieee.org/publications_standards/publications/rights/rights_link.html to learn how to obtain a License from RightsLink.

If applicable, University Microfilms and/or ProQuest Library, or the Archives of Canada may supply single copies of the dissertation.

Thesis / Dissertation Reuse

The IEEE does not require individuals working on a thesis to obtain a formal reuse license, however, you may print out this statement to be used as a permission grant:

Requirements to be followed when using any portion (e.g., figure, graph, table, or textual material) of an IEEE copyrighted paper in a thesis:

1) In the case of textual material (e.g., using short quotes or referring to the work within these papers) users must give full credit to the original source (author, paper, publication) followed by the IEEE copyright line © 2011 IEEE.
2) In the case of illustrations or tabular material, we require that the copyright line © [Year of original publication] IEEE appear prominently with each reprinted figure and/or table.
3) If a substantial portion of the original paper is to be used, and if you are not the senior author, also obtain the senior author's approval.

Requirements to be followed when using an entire IEEE copyrighted paper in a thesis:

1) The following IEEE copyright/ credit notice should be placed prominently in the references: © [year of original publication] IEEE. Reprinted, with permission, from [author names, paper title, IEEE publication title, and month/year of publication]
2) Only the accepted version of an IEEE copyrighted paper can be used when posting the paper or your thesis on-line.
3) In placing the thesis on the author's university website, please display the following message in a prominent place on the website: In reference to IEEE copyrighted material which is used with permission in this thesis, the IEEE does not endorse any of [university/educational entity's name goes here]'s products or services. Internal or personal use of this material is permitted. If interested in reprinting/republishing IEEE copyrighted material for advertising or promotional purposes or for creating new collective works for resale or redistribution, please go to http://www.ieee.org/publications_standards/publications/rights/rights_link.html to learn how to obtain a License from RightsLink.

If applicable, University Microfilms and/or ProQuest Library, or the Archives of Canada may supply single copies of the dissertation.

Thesis / Dissertation Reuse

The IEEE does not require individuals working on a thesis to obtain a formal reuse license, however, you may print out this statement to be used as a permission grant:

Requirements to be followed when using any portion (e.g., figure, graph, table, or textual material) of an IEEE copyrighted paper in a thesis:

1) In the case of textual material (e.g., using short quotes or referring to the work within these papers) users must give full credit to the original source (author, paper, publication) followed by the IEEE copyright line © 2011 IEEE.
2) In the case of illustrations or tabular material, we require that the copyright line © [Year of original publication] IEEE appear prominently with each reprinted figure and/or table.
3) If a substantial portion of the original paper is to be used, and if you are not the senior author, also obtain the senior author's approval.

Requirements to be followed when using an entire IEEE copyrighted paper in a thesis:

1) The following IEEE copyright/ credit notice should be placed prominently in the references: © [year of original publication] IEEE. Reprinted, with permission, from [author names, paper title, IEEE publication title, and month/year of publication]
2) Only the accepted version of an IEEE copyrighted paper can be used when posting the paper or your thesis on-line.
3) In placing the thesis on the author's university website, please display the following message in a prominent place on the website: In reference to IEEE copyrighted material which is used with permission in this thesis, the IEEE does not endorse any of [university/educational entity's name goes here]'s products or services. Internal or personal use of this material is permitted. If interested in reprinting/republishing IEEE copyrighted material for advertising or promotional purposes or for creating new collective works for resale or redistribution, please go to http://www.ieee.org/publications_standards/publications/rights/rights_link.html to learn how to obtain a License from RightsLink.

If applicable, University Microfilms and/or ProQuest Library, or the Archives of Canada may supply single copies of the dissertation.

Title:	High resolution surface imaging arrays interrogated with microfluidically controlled metalized plates
Conference Proceedings:	2014 IEEE Antennas and Propagation Society International Symposium (APSURSI)
Author:	Abhishek Dey; Gokhan Mumcu
Publisher:	IEEE
Date:	6-11 July 2014

Thesis / Dissertation Reuse

The IEEE does not require individuals working on a thesis to obtain a formal reuse license, however, you may print out this statement to be used as a permission grant:

Requirements to be followed when using any portion (e.g., figure, graph, table, or textual material) of an IEEE copyrighted paper in a thesis:

1) In the case of textual material (e.g., using short quotes or referring to the work within these papers) users must give full credit to the original source (author, paper, publication) followed by the IEEE copyright line © 2011 IEEE.
2) In the case of illustrations or tabular material, we require that the copyright line © [Year of original publication] IEEE appear prominently with each reprinted figure and/or table.
3) If a substantial portion of the original paper is to be used, and if you are not the senior author, also obtain the senior author's approval.

Requirements to be followed when using an entire IEEE copyrighted paper in a thesis:

1) The following IEEE copyright/ credit notice should be placed prominently in the references: © [year of original publication] IEEE. Reprinted, with permission, from [author names, paper title, IEEE publication title, and month/year of publication]
2) Only the accepted version of an IEEE copyrighted paper can be used when posting the paper or your thesis on-line.
3) In placing the thesis on the author's university website, please display the following message in a prominent place on the website: In reference to IEEE copyrighted material which is used with permission in this thesis, the IEEE does not endorse any of [university/educational entity's name goes here]'s products or services. Internal or personal use of this material is permitted. If interested in reprinting/republishing IEEE copyrighted material for advertising or promotional purposes or for creating new collective works for resale or redistribution, please go to http://www.ieee.org/publications_standards/publications/rights/rights_link.html to learn how to obtain a License from RightsLink.

If applicable, University Microfilms and/or ProQuest Library, or the Archives of Canada may supply single copies of the dissertation.

ABOUT THE AUTHOR

Abhishek Dey received his Bachelors in Engineering from Bengal Engineering and Science University, Shibpur, India in 2010 and Masters in Engineering from University of South Florida in 2011. Since joining the PhD program in 2012, Abhishek Dey has performed research on radiofrequency (RF) devices and antennas using novel materials and microfluidic reconfiguration techniques. He was recipient of the 2016 IEEE APS PhD fellowship, 2014 student research award from Florida High Tech Corridor Council, 2013 USF College of Engineering Research week poster award, student paper finalist (top 15 out of 144 student papers) in 2013 IEEE APS Symposium, and 2011 USF Provost PhD Fellowship. He was with Qorvo, FL in summer 2015 as an acoustic filter design intern. He is currently with Qorvo, FL as a senior acoustic filter design engineer.